論文 / 著書情報
Article / Book Information

題目(和文)	ナフサ接触分解のためのH-ZSM-5ゼオライト触媒の設計とその性能
Title(English)	Design and performance of H-ZSM-5 zeolite catalyst for naphtha cracking
著者(和文)	望月大司
Author(English)	Hiroshi Mochizuki
出典(和文)	学位:博士(工学), 学位授与機関:東京工業大学, 報告番号:甲第9499号, 授与年月日:2014年3月26日, 学位の種別:課程博士, 審査員:野村　淳子,小松　隆之,馬場　俊秀,原　亨和,福島　孝典
Citation(English)	Degree:Doctor (Engineering), Conferring organization: Tokyo Institute of Technology, Report number:甲第9499号, Conferred date:2014/3/26, Degree Type:Course doctor, Examiner:,,,,
学位種別(和文)	博士論文
Type(English)	Doctoral Thesis

Doctor thesis, 2014

Design and performance of H-ZSM-5 zeolite catalyst for naphtha cracking

(ナフサ接触分解のための H-ZSM-5 ゼオライト触媒の設計とその性能)

Department of Electronic Chemistry
Interdisciplinary Graduate School of Science and Engineering
Tokyo Institute of Technology

Hiroshi Mochizuki (11D27044)

Contents

Chapter 1: General introduction

Chapter 2: Control of crystallite size of H-ZSM-5 zeolites and their catalytic properties for cracking of *n*-hexane

Chapter 3: Enlargement of external surface area of H-ZSM-5 zeolite by alkali treatment for *n*-hexane cracking

Chapter 4: Effect of Al content and Al state of H-ZSM-5 on catalytic activity for *n*-hexane cracking

Chapter 5: Effect of acid site distributions in the pores of H-ZSM-5 zeolites on their catalytic properties

Chapter 6: Summary

List of Publications

List of conference Presentations

Acknowledgements

Chapter 1

General introduction

1-1 Zeolites

1-1-1 Introduction of zeolites

The term zeolite was originally coined in 1756 by Swedish mineralogist Cronstedt [1]. He recognized zeolite as new class of minerals consisting of hydrated aluminosilicates of the alkali and alkaline earths. Because of the unique frothing characteristics when heated in a blowpipe flame, he called the material “zeolite”, from the two Greek words, “zeo”, meaning "to boil" and “líthos”, meaning "stone". Many occur as natural minerals, but it is the synthetic varieties which are among the most widely used sorbents, catalysts and ion-exchange materials in the world because of their unique properties such as cation exchange ability, strong acidity (H^+ form zeolite), molecular sieving properties due to their molecular scale pore diameter (≤10 Å) [2-4].

Zeolites consist of the primary tetrahedral building unit, TO_4, where the central tetrahedrally bonded atom (T-atom) is usually either a Si or Al atom, surrounded by four oxygen atoms (Fig. 1.1). These TO_4 units interconnect with the four oxygen atoms, resulting in characteristic and periodic cavities and/or channels throughout the zeolite structure. Ion exchange ability is generated by the incorporation of Al into the silica framework. The +3 charge on the Al makes the framework negatively charged, and requires the presence of extraframework cations within the structure to keep the overall framework electrostatically neutral.

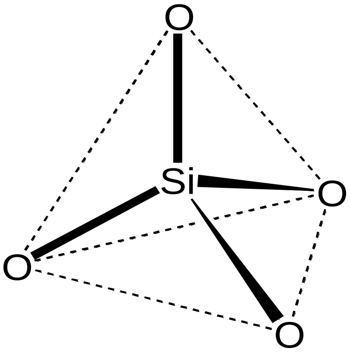

Figure 1.1 TO_4 units

Classical zeolites are aluminosilicates as described above. However, it has been apparent that other elements, such and B, Ge, Zn and some transition metals can also be incorporated into the framework instead of Al. Furthermore, other porous materials with a similar framework structure such as aluminophosphtes (AlPOs) and metalloaluminophsphate (MeAPOs) have been discovered [5]. Therefore, currently, the International Zeolite Association (IZA) defined as zeolites as “open 4-

connected 3-dimensional nets, which have the general (approximate) composition AB_2, where A is a tetrahedrally connected atom and B is any 2-connected atom" and "framework density, the number of tetrahedrally coordinated framework atoms (T-atoms) per 1000 Å^3 of this material is less than or equal to 20" [6]. In this thesis, I limited the mean of "zeolite" to crystalline tectoaluminosilicate having molecular sized pore structures.

1-1-2 Zeolite structure

The general formula for aluminosilicate zeolite is

$$\mathbf{M^{x/n}(AlO_2)_x(SiO_2)_y}$$

where n is the valence of extraframework cation M, x + y the total number of tetrahedral per unit cell and y/x the atomic ratio. The Al content in framework strongly affects the physicochemical properties (hydrophilicity and thermal and hydrothermal stability). In general, zeolites with Si/Al ratios of below 2 (e.g. A, X) are described as low silica or Al-rich zeolite and those with Si/Al ratios above 5 are described as high silica zeolites. The hydrophobicity and stability of zeolite increase with a decrease in the Al content, while its ion-exchange capacity increases with an increase in the Al content.

Zeolite frameworks can be thought to consist of finite or infinite component units. The primary building units (PBU) of zeolite is silicate and aluminate tetrahedra. Typically, Al-O and Si-O bond distances are 1.73 and 1.61 Å, respectively, with O-T-O angles (T is T atom) close to the tetrahedral angle, 109.4° [7]. There is more variation in the Si-O-Si bond angles between tetrahedral, where the average angle is 154° with a range of 135-180° and more of 148° [8], Variation in T-O-T angles enables a wide diversity of frameworks to exist. More complex secondary building units (SBU) and composite building units (CBU) can be formed by linking together groups of PBUs. The secondary building units (SBU), which contain up to 16 T-atoms, are derived assuming that the entire framework is made up of one type of SBU only. The CBUs appear in several different framework structures, and can be useful in identifying relationships between framework types. These are different from SBUs in that they cannot necessarily be used to build the entire framework. Each unit has been assigned a lower case italic three-character designation. With the exception of the double 4-, 6- and 8-rings (D4R, D6R and D8R, respectively), a code corresponding to one of the framework types containing the CBU has been used for this purpose [9]. Figure 1.2 shows examples of SBUs and CBUs.

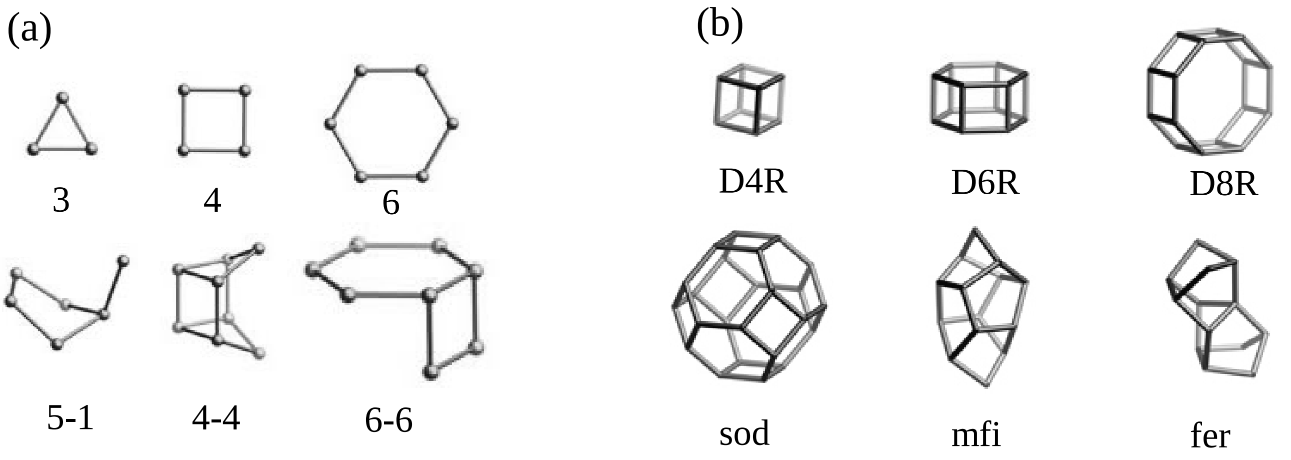

Figure 1.2 Example of SBUs (a) and CBUs (b) [9]

Zeolite structure is also commonly described in terms of the size, geometry and connectivity of pore space defined by their framework. Zeolite can be classified into four categories by the pore-opening size.

(1) ***Small pore zeolites*** with 8 membered-ring (8-MR) pore apertures (8 T-atoms and 8 oxygen) having free diameter of 0.30-0.45 nm.

(2) ***Medium pore zeolites*** with 10 MR apertures, 0.45 - 0.60 nm in free diameter

(3) ***Large pore zeolites*** with 12 MR apertures, 0.60- 0.75 nm

(4) ***Extra-large pore zeolites*** with more than 12 MR

Furthermore, zeolite is also classified according to the dimension of the pore system. The connectivity of pore space can be one dimensional, 1D, (unconnected channels), 2D (where any point in a place in the pore system can be accessed from any other point in that plane) or 3D, where any part of the pore space is accessible from any other point within the crystal. These pore structures strongly affect molecular sieving properties, adsorption properties and diffusion of molecules in the pores. Figure 1.3 shows the typical zeolite frameworks.

Zeolite structures are designated by a 3 capital letter code according to rules set by the Commission of IZA and 213 Framework Type Codes have been assigned as of December 1, 2013 [9].

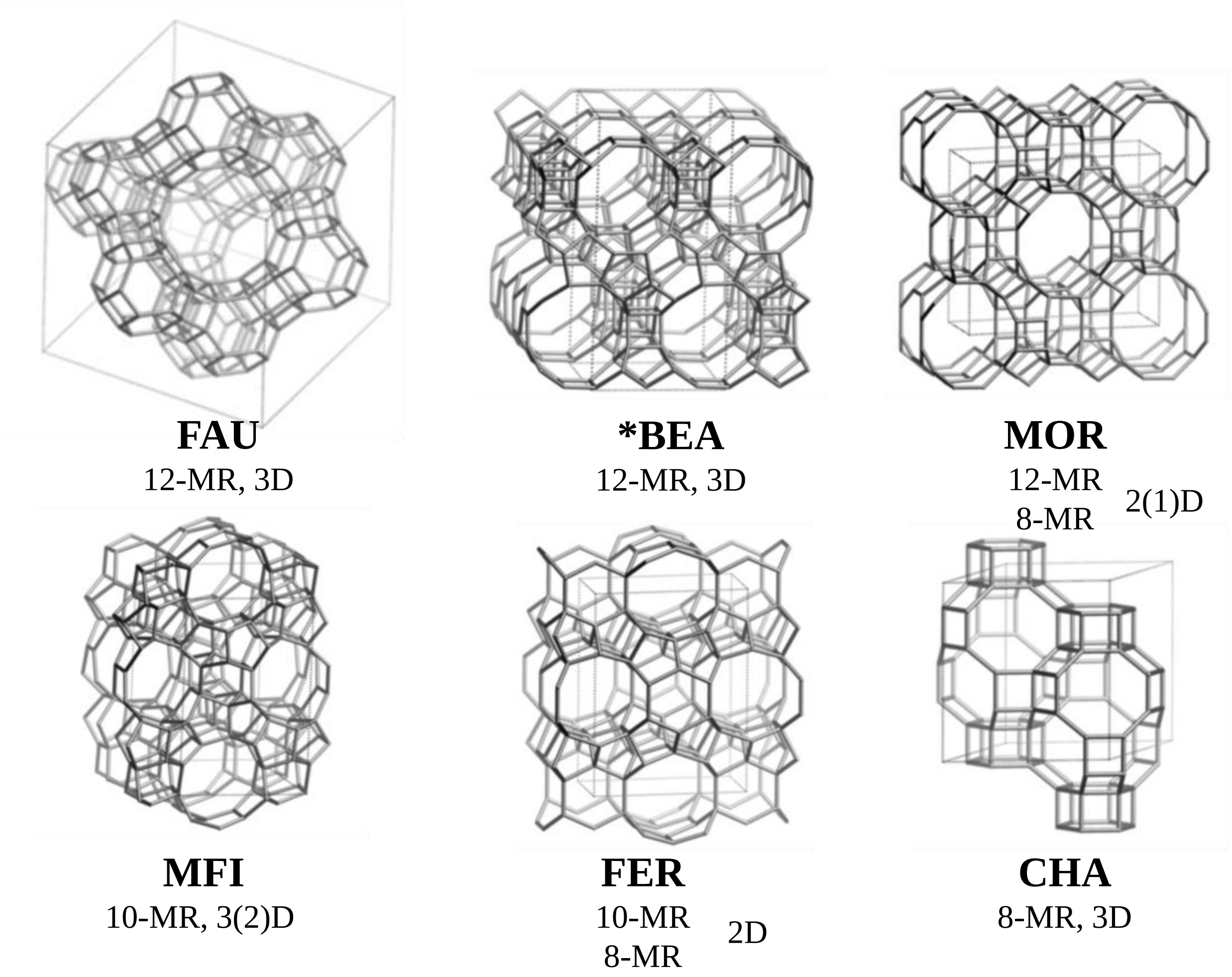

FAU
12-MR, 3D

***BEA**
12-MR, 3D

MOR
12-MR
8-MR 2(1)D

MFI
10-MR, 3(2)D

FER
10-MR
8-MR 2D

CHA
8-MR, 3D

Figure 1.3 Typical zeolite frameworks [9]

1-1-3 Zeolite synthesis

Since the first hydrothermal synthesis of zeolites was achieved in 1940s by Barrer [10, 11], many zeolites were synthesized using only inorganic reagents, and all the phases studied up to 1961 (such as the classical synthetic zeolites A, X, and Y) were synthesized in this manner. In the 1960s, new synthesis method using organic compounds as structure-directing agents (SDAs), particularly quaternary ammonium salts was developed. The introduction of SDAs allowed the synthesis of new zeolite structure, such as Beta [12] and ZSM-5 [13]. These are often referred to as templates, since the zeolite structure is formed around them. Clearly, the steric requirement will limit the number of organic units which can be accommodated. Thus, SDAs such as quaternary ammonium cations, which also act as charge-balancing cations, impose a restriction on the zeolite framework charge density, resulting in the formation of increased Si/Al ratios. For instance, the Si /Al ratio of sodalite aluminosilicate synthesized using only teramethylammoniumu (TMA) cation is higher than that synthesized using only Na cations, since only one TMA cation can be accommodated in the sodalite cage (Fig. 1.4) [14].

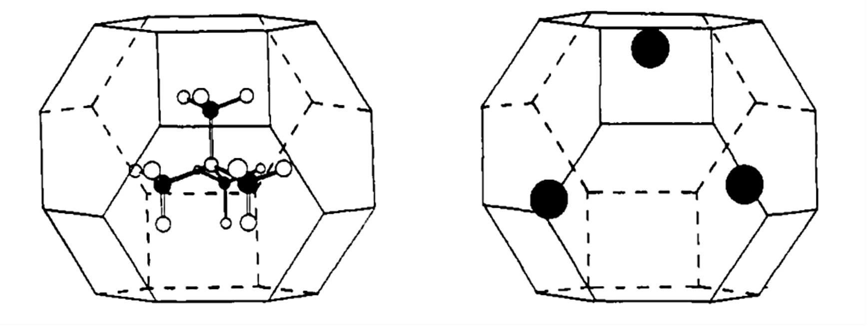

TMA-sodalite
Si/Al = 5

Na-sodalite
Si/Al = 1

Figure 1.4 Illustration of cations in the sodalite cage [15]

High silica (Si/Al ≥ 5) aluminosilicate zeolites are usually synthesized [2-4, 16, 17] under hydrothermal conditions from reactive gels in alkaline media at temperatures between about 353 and 493 K. Zeolite synthesis occurs with reagents being a silica source, an alumina source, a mineralizing agent such as OH or F anions, and for higher Si/Al ratio zeolites, organic molecules as SDAs. The role of inorganic metal cations, such as Na or K cations, is quite profound. In one example, these cations take a role as counter cations to keep the overall framework neutral. It is difficult to determine the product phase only by theory of equilibrium because zeolites are synthesized as a metastable phase in many cases. Thus, the product phase and morphology of crystal are strongly affected by synthesis conditions beside temperature and compositions of raw materials, such as a type of raw materials, stirring speed, pH and so on.

1-1-4 Crystallization mechanism of MFI type zeolite

The crystallization of pure silica **MFI** type zeolite using tetrapropylammonium (TPA) cations as an SDA have been investigated by several researchers [18].

In a very significant paper, Chang and Bell [19] have studied the formation of ZSM-5 from Al-free precursor gels at 363 - 368 K by using XRD, ^{29}Si MAS NMR spectroscopy, and ion exchange. The NMR results suggested that major changes in gel structure occur during the early stages of the reaction. This is confirmed by the demonstration of ion sieve effects, suggesting that in the tetrapropylammonium (TPA) system, embryonic structures with Si/TPA = 20-24 are formed rapidly upon heating. These first-formed units, approximating to channel intersections and containing one TPA cation in each unit, are initially randomly connected to each other but in time become ordered ("annealed") through repeated cleavage and recombination of siloxane bonds, mediated by hydroxide ions. The hydrophobic effect and the isomorphism between water and silicate structure are invoked to provide a possible mechanism for ZSM-5 nucleation with the following steps:

(a) formation of clathrate-like water structure around the template, (b) isomorphous substitution of silicate for water in these cages (which resemble ZSM-5 channel intersections), and (c) progressive ordering of these entities into the final crystal structure.

Burkett and Davis [20-22] build upon the work of Chang and Bell mentioned above to examine the role of TPA as SDAs in silicalite synthesis, primarily by MAS NMR spectroscopy. ^{1}H-^{29}Si CP MAS NMR results provide direct evidence for the existence of preorganized inorganic-organic composite structures during the synthesis, in which the TPA molecules adopt a conformation similar to that the one they have in the zeolite product. The initial formation of the inorganic-organic composite is initiated by overlap of the hydrophobic hydration spheres of the inorganic and organic components, with subsequent release of ordered water to establish favorable van der Waals interactions. Thereafter, aggregation of these composite species is responsible for nucleation. Crystal growth occurs through diffusion of the same species to the surface of the growing crystallites to give a layer-by-layer growth mechanism (Fig. 1.5).

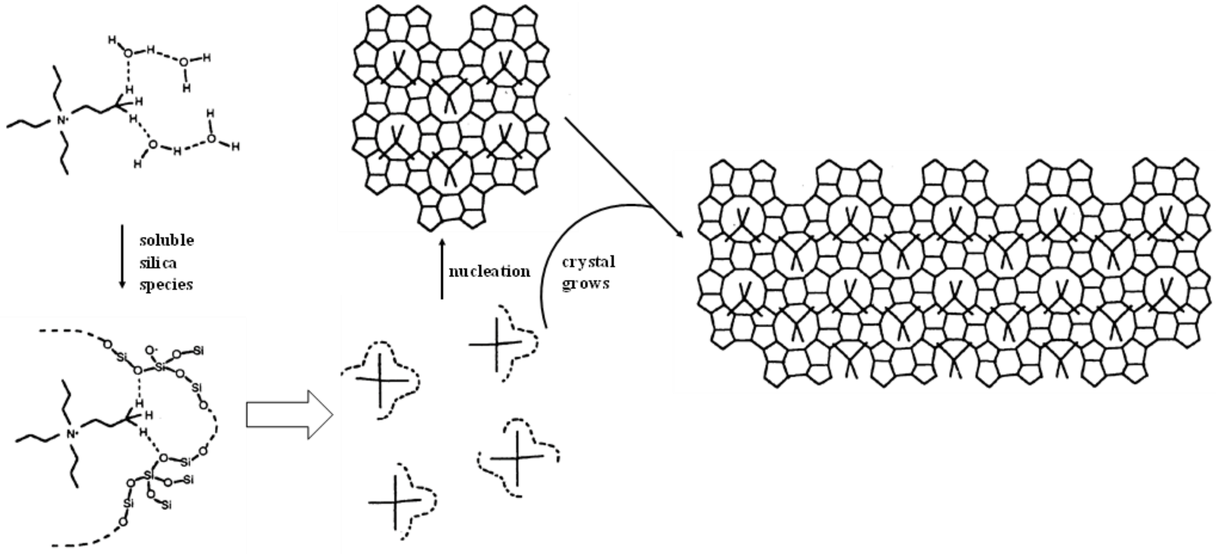

Figure 1.5 Mechanism of structure direction and crystal growth in the synthesis of TPA-Si-ZSM-5 [18]

However, in a series of papers by the Leuven group [23-27], this type of procedure constitutes the main framework of their studies. In part, this work is a continuation of the characterization of the zeolite precursor material identified by Schoeman [28]. The silica species in an aged clear sol (which crystallizes silicalite upon heating) were extracted (80% efficiency) using a sequence of acidification, salting out, phase transfer into organic solvent, and freeze-drying. The resulting powder was characterized by a wide variety of methods leading to the identification of constituent "nanoslabs" having dimensions 1.3 × 4.0 × 4.0 nm and having the MFI structure with nine intersections per particle, each constituent unit containing a TPA cation (Figure 1.6 a). Aggregation of precursor units leads to larger particles measuring up to 15.6 × 8 × 8 nm and ultimately to the crystalline colloidal MFI-type material which forms the final product of the synthesis (Figure 1.6 b).

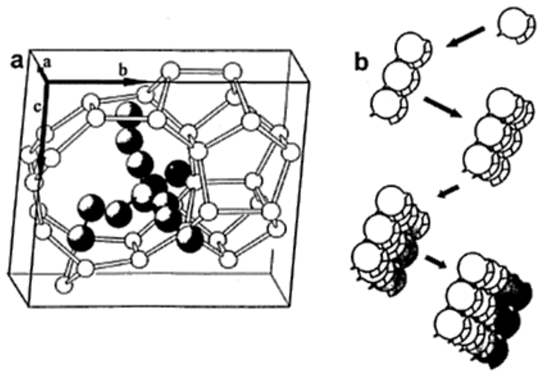

Figure 1.6 The "nanoslab" hypothesis of the Leuven research group: (a) the precursor unit containing one TPA cation and (b) schematic representation of nanoslab formation by aggregation of precursor units [18]

1-1-5 Catalysis

Zeolite have found wide application as catalysts in the oil refining and petrochemical industry [29], where they have been gradually replacing amorphous catalysts. Types of commercial processes using zeolite-based catalysts are listed in Table 1.1 [29]. The superior catalytic performance of zeolites is related to some important properties:

- Strong acid sites compared to amorphous aluminosilicate
- Shape selectivity
- High thermal and hydrothermal stability

Among above properties, acidity and shape selectivity are explained as follows.

Table 1.1 Types of commercial processes using zeolite-based catalysts [29]

Zeolite structure code	**FAU**	**LTL**	**MOR**	**BEA**	**MWW**	**MTW**	**MFI**	**FER**	**AEL**	**Area**
Zeolite name	Y, USY	L	Mordenite	Beta	MCM-22, MCM-49	ZSM-12	ZSM-5	Ferrierite	SAPO-11	
Process										
Naphtha isomerization			B							*Refining*
Iso-dewaxing							B		B	
Dewaxing							M			
Hydro-cracking	B									
Hydro-dearomatization	B									
FCC	M						M			
Olefin oligomerization					M		M			
Olefin isomerization								M		
Ethylbenzene					M		M			*Petrochemicals*
Cumene	M		M	M	M					
C2, C3-transalkylation	M		M	M	M					
p-Ethyltoluene							M			
p-t-Butylethylbenzene						M				
Xylene isomerization							M/B			
Ethylbenzene isomerization			B							
Toluene disproportionation			B				B			
C9+ transalkylation			B							
Naphtha aromatization		B								
LPG or olefin aromatization							B			
Amination			M				M			*Chemicals*
Hydration							M			
Chlorination/isomerization		M					M			
Beckmann rearrangement							M			
Oxidation							M			
Acylation	M			M						

M stands for monofunctional catalyst and B stands for bifunctional catalysts

(I) Acidity of zeolite

Most of the catalytic processes are based upon acid catalyzed reactions in which the exchangeable cation of the zeolite is replaced by proton that provides Brønsted acidity. A first feature of zeolites is their stronger acidity compared to amorphous alumino-silicate. Morier [30] has proposed the existence of an enhanced donor-acceptor interaction in zeolites. This interaction has been extended by Robo and Gajida [31] into a resonance model of the (Al(OH)Si) bond structure with bridging hydroxyls (a) and terminal silanols (b) as extreme limits (Fig. 1.7):

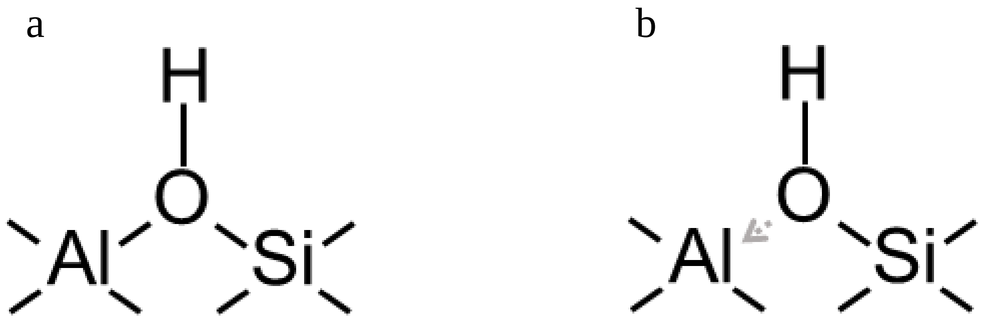

Figure 1.7 (Al(OH)Si) bond structure with bridging hydroxyls (a) and terminal silanols (b)

Indeed, NMR data indicate that OH groups of amorphous aluminosilicate are primarily terminal where those of zeolite are primarily bridging, and that the interaction of O with Al weakens the OH bond and, therefore, increases the acid strength [31]. A relation exists between the T-O-T bond angles and the Brønsted acid strength of the associated proton in the zeolite [31]. The greater the angle, the stronger the sites. Thus, the protonic sites of H-MOR (bond angle between 143-180°) and H-MFI (133-177°) are stronger than those of H-FAU (138-147°).

Weak to moderately strong acid sites can be generated in zeolite by ion exchange with multivalent cations. Owing to the polarizing effect of metal cations, water is dissociatively adsorbed, and equilibrium of equation is established.

$$[M(H_2O)]^{n+} \rightarrow [M(OH)]^{(n-1)} + H^+$$

The following order of Brønsted acidity is given for cation-exchanged zeolite:

H form >> La form > Mg form > Ca form > Sr form > Ba form

The metallosilicates containg trivalent elements in the framework other than Al (B, Ga, In, Fe) are of interest in designing the acid strength. The ranking in the acid strength drawn from theoretical calculations is in relatively good agreement with acidity measurements [32]. In the MFI type metallosilicates, the acid strength is in the following order:

B(OH)Si < In(OH)Si < Fe(OH)Si < Ga(OH)Si< Al(OH)Si

When an H-zeolite is heated to high temperature, water is ariven off and coordinatively unsaturated Al^{3+} ions are formed. These are Lewis acid sites (Fig. 1.8) [33].

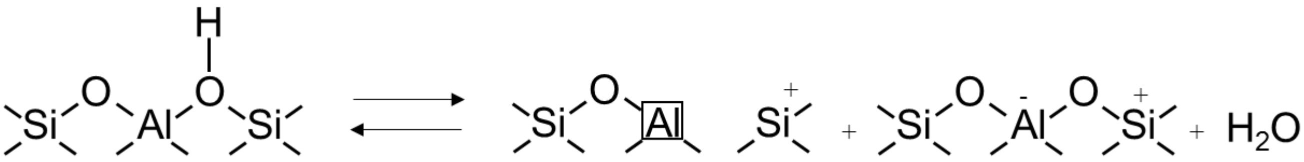

Figure 1.8 Formation model of Lewis acid site by dehydration or hydrolysis of Al-O-Si bond [33]

These Lewis acid sites are also formed by hydrolysis of Al-O-Si bonds (dealumination) under steam conditions.

(II) Shape selectivity

Shape-serectivity was first described by Weisz and Frilette in 1960 [34]. They were not only the pioneers of shape-selective catalysis, but in their subsequent publications they demonstrated its many possible applications. The types of shape- selectivities can be distinguished by depending on whether pore size limits the entrance of the reacting molecule, the departure of the product molecule, or the formation of certain transition states:

(1) Reactant shape-selectivity

The simplest forms of shape selectivity come from the impossibility of certain molecules in reactant mixture entering the zeolite pores. Reactant shape selectivity was the basis of the Selecto-forming process. The *n*-paraffin in light naphtha (mainly *n*-pentane and *n*-hexane) enter the pores of erionite, which is a small pore (8-MR) zeolite, and, therefore the cracking of n-paraffin takes place, whereas branched paraffin are excluded from the pores and, therefore, the cracking of them hardly takes place (Fig. 1.9).

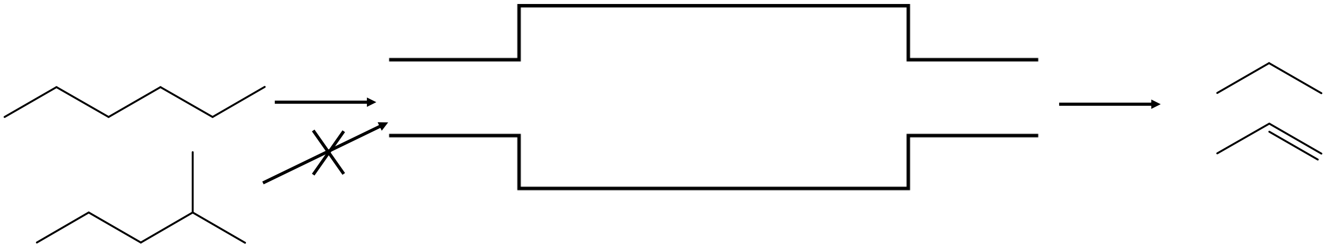

Figure 1.9 Example of reactant shape selectivity: Cracking of paraffins over H-erionite zeolite

(2) Product shape-selectivity

Product shape selectivity come from the impossibility of certain product molecules formed inside the pores exiting from the pores. This shape selectivity plays a key role in various processes developed by Mobil for the selective synthesis of para (*p*-) dialkylbenzene (35): such as toluene disproportionation and alkylation of toluene. In these processes, the bulkier ortho (*o*-) and meta (*m*-) isomers are also formed in the pores, but their exit is hampered by their slower diffusion; this selective removal of product (*p*- isomer) allows the bulkier isomers (*o*- and *m*-) to be transformed into the less bulky species (*p*-isomer). In toluene disproportionation the selectivity to *p*-xylene of the ZSM-5 which is medium pore (10-MR) zeolite is singnificantly increased by deposits of silica, maganesia, coke etc (Fig. 1.10). The diffusion coefficient of p-xylene in modified ZSM-5 zeolite is significantly higher than that of *o*- and *m*-xylene.

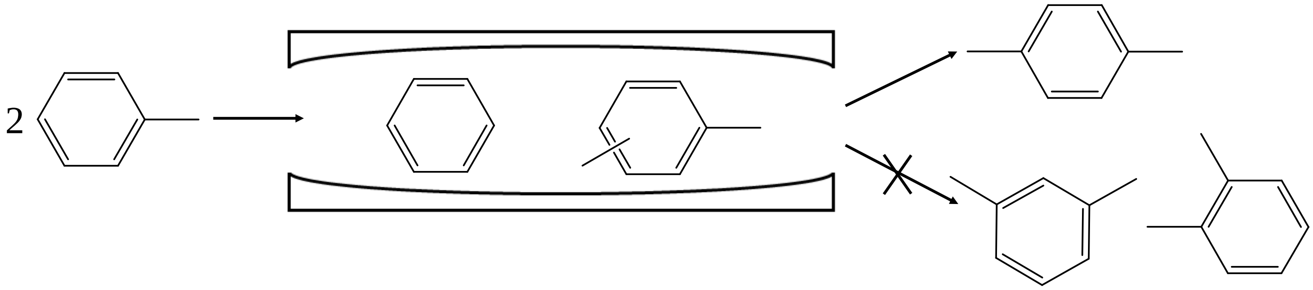

Figure 1.10 Example of product shape selectivity: Disproportionation of toluene over modified H-ZSM-5 zeolite

(3) Transition state shape-selectivity

In restricted transition state-type selectivity, certain reactions are prevented because the transition state is too large for the cavities of the molecular sieve. However, neither reactants nor potential products are prevented from diffusing through the pores; only the formation of the transition state is hindered. An interesting example is acid-catalysed *m*-xylene disproportionation. Figure 1.11 clearly shows an alkyl group in the transition state for this reaction protruding downward, making this transition state too wide for the pores of mordenite which is large pore (12-MR) zeolite. Thus, whereas the 1,2,4-isomer can form, the 1,3,5-isomer cannot [36, 37].

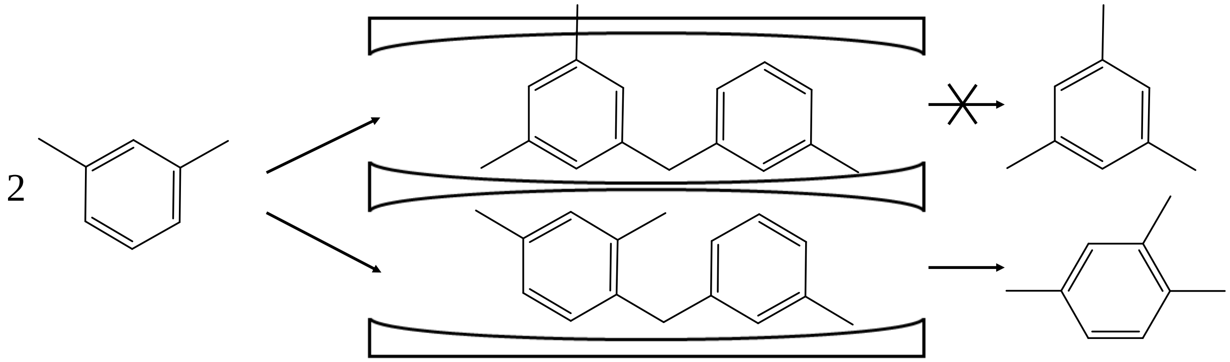

Figure 1.11 Example of transition state shape selectivity: Disproportionation of m-xylene over H-moredenite zeolite

Another example for transition-state selectivity is cracking of 3-methylpentane over ZSM-5 zeolite. Haag and co-workers determine the causes of shape selectivity in the cracking of C6 and C9 paraffins and olefins over ZSM-5 [38]. They have found that intrinsic cracking rates of monomethyl paraffins are affected by steric constraints on the transition states (Fig. 1.12). Cracking of the structurally equivalent olefins does not require such bulky transition states; and, as a consequence, they crack with about equal rates.

The *m*-xylene conversion has been used as a test reaction to investigate void size and structure of zeolites. In *m*-xylene conversion, the disproportionation of *m*-xylene proceeds with difficulty in a narrow reaction space, because it is a bimolecular reaction, involving diphenylmethane-like intermediates, that are bulkier than the reagent and product molecules [40]. In contrast, the isomerization of *m*-xylene proceeds in absence of steric hindrance, because it is a monomolecular reaction [40]. Hence, the isomerization / disproportionation ratio can be regarded as a parameter of the size of the reaction spaces in the pores, also 3-methylpentane cracking has been used as test reaction.

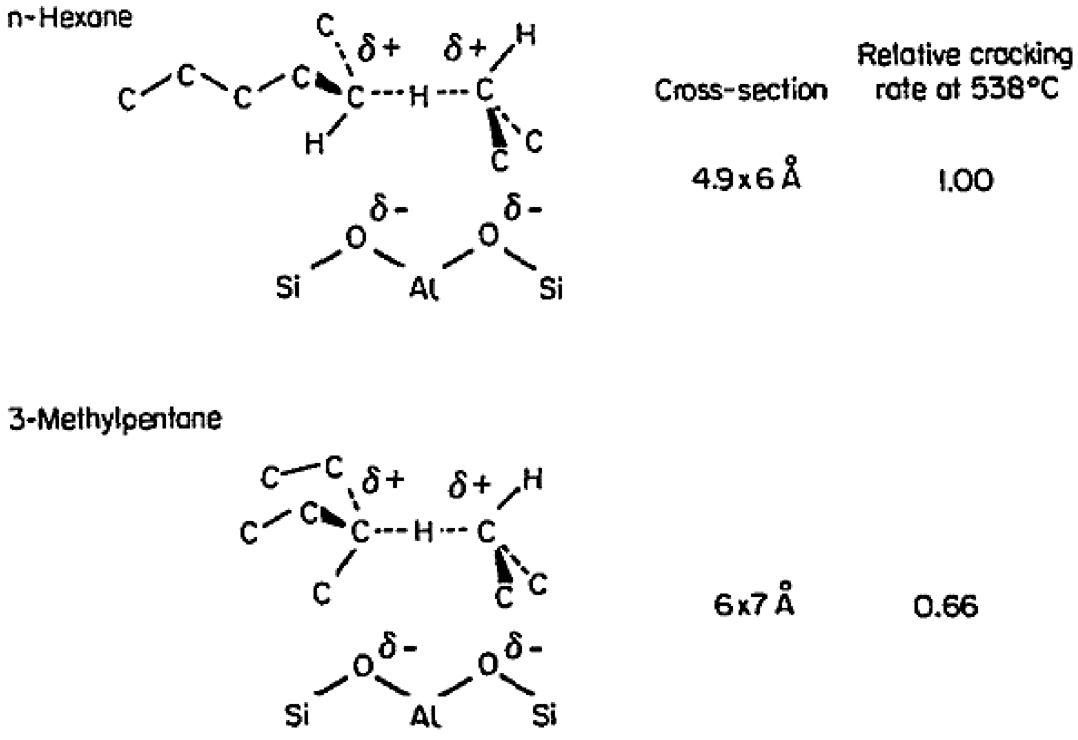

Figure 1.12 Dimensions of transition states of C6 paraffins [39]

The constraint index (CI) the ratio of the first-order rate constants for cracking of *n*-hexane and its isomer 3-methylpentane. The CI is strongly dependent on the pore size of the zeolite. Small values between 0 and 2 mean little or no shape selectivity (large-pore zeolites)m values between 2 and 12 a medium selectivity (medium-pore zeolites), and values higher than 12 a high shape selectivity (small-pore zeolites) [41-44]. This is because narrow spaces impose more severe steric constraint on the bulky transition state of 3-methylpentane than on that of *n*-hexane. These model reactions can be used to get detailed insight into the void structure of unknown new zeolites.

These shape-selective properties described above strongly depend on structure of zeolites: such as the size of pore window, the pore space geometry (presence or absence of large cages). Therefore, it is necessary to select zeolite which has the optimum pore structure for target reactions. Further-more, the acid site location in the pores of zeolite is important factor to affect catalytic properties due to shape selectivity. For example, *m*-xylene conversion over H-ferrierite zeolite with different acid site distributions has been reported [45]. H-ferrielite zeolite with the FER topology has 2-dimensional pore system consist of 10-MR and the cages accessible through 8-MR windows. Pérez-Pariente and co-workers were found that the distribution of Brønsted acid sites between the cage and the 10-MR channel dependent on the type of OSDAs. The catalytic activity of the zeolites in *m*-xylene isomerisation increased as the relative population of strong Brønsted acid sites in sterically constrained sites inside the H-ferrierite pores (8-MR) decreased. It is because the size of *m*-xylene is too large to enter the 8-MR pores window in H-ferrielite.

1-1-6 ZSM-5 zeolite

ZSM-5 zeolite having the **MFI** topology has been widely applied in many important catalytic reactions because of its special porous structures. The **MFI** structure has twelve distinct T-sites and consists of parallel and straight 10-membered ring (MR) channels intersected by sinusoidal 10-MR channels [9]. Although the sizes of both 10-MR are similar to that of the aromatic ring (ca. 5.5 Å), the intersections of these 10-MR have large spherical spaces (diameter ca. 10 Å in diameter) as shown Fig. 1.13.

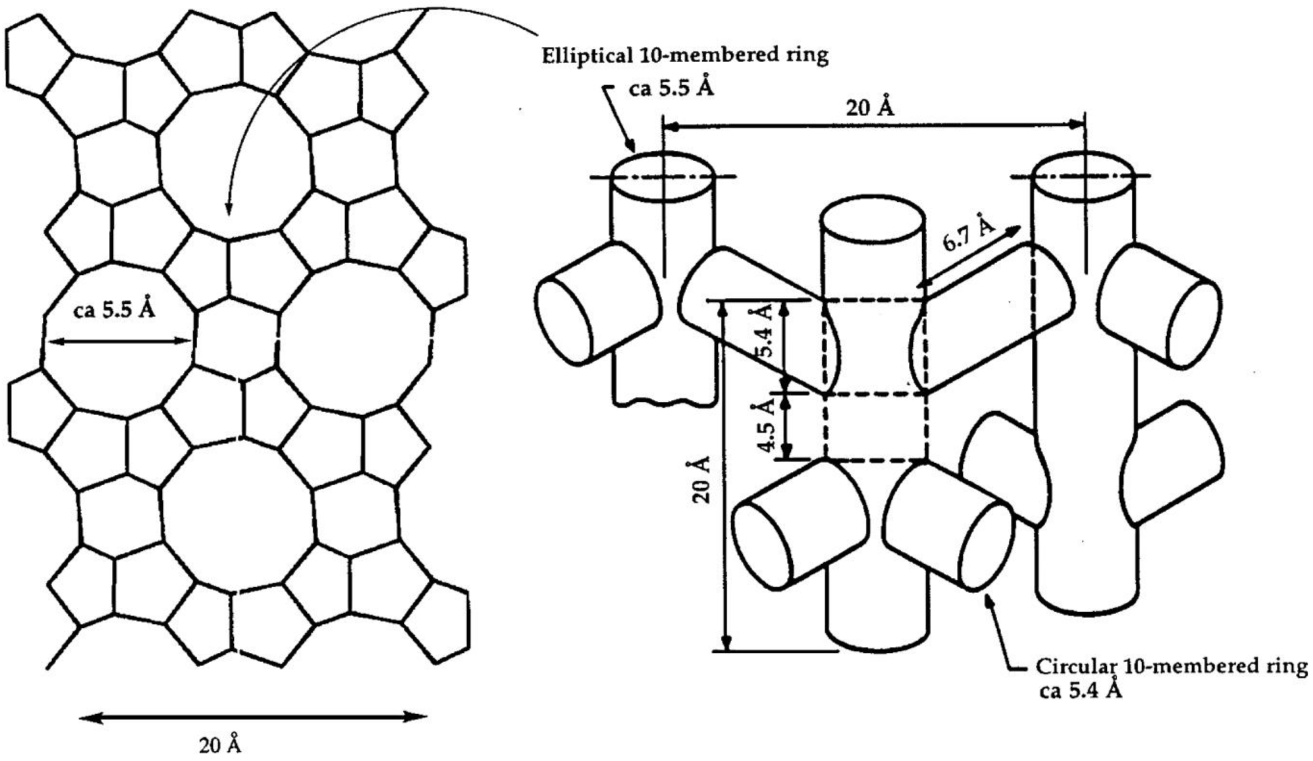

Figure 1.13 Representation of the External Surface (left) and the internal surface (right) of a MFI Zeolite [46]

ZSM-5 with a wide variety of Si/Al ratios (~∞) has been hydrothermally synthesized using TPA as an OSDA [47-49]. Furthermore, ZSM-5 zeolite can be synthesized using many types of OSDA or OSDA free conditions [50]. The number of organic species which play a role of OSDA in ZSM-5 synthesis is quite large (Table 1.2).

Table 1.2 Organic molecules used for synthesis of ZSM-5 [50]

Tetrapropylammoniumu	Alcohols	Pentaerythritol
Tetraethylammoniumu	Glycerol	Dipropylenetriamine
Tripropylamine	*n*-propylamine	Dihexamethylenetriamine
Ethyldiamine	Di-*n*-butylamine	Triethylenetetramine
Propanolamine	Di-*n*-propylamine	Diethylenetetramine
Ethanolamine	1,5-diaminopentane	1-alkyl-4-azonibicyclo[2,2,2]octane-4-oxide halide
Methyl quinuclide	1,6-diaminohexane	Hexanediol
NH3 + Alcohol	Morpholine	propylamine

ZSM-5 was first synthesized in 1965 by Landolt and Argauer [13]. It was soon determined to be a very shape-selective material that cracked only normal or slightly branched paraffins. For much of the late 1960s most of the ZSM-5 was directed toward the development of new dewaxing catalysts [51]. Since then, ZSM-5 zeolite has been widely used in many petrochemical catalytic processes such as oligomerization [52, 53], hydrocracking [54], cracking of olefin [55-61] and paraffin [62-65], methanol to olefin [66], aromatization [67, 68], isomerization, disproportionation and alkylation of aromatic compounds processes [69-71]. The superior catalytic performance of ZSM-5 for various reactions are caused by several excellent following features:

(1) Shape selective properties for various reaction.
(2) Strong acidity due to high Si/Al ratios.
(3) Controllable wide range Si/Al ratios.
(4) High thermal and hydrothermal stability.
(5) Long catalytic lifetime due to lack enough space in the pores for the polymerization of coke precursors [72].

From above features, ZSM-5 zeolite has contributed to not only the development of several industrial processes but also elucidation and development of fundamental chemistry of zeolite.

1-2 Cracking

1-2-1 Hydrocarbon cracking process

The cracking is one of the most important reactions in petrochemical industry. In petroleum chemistry, hydrocarbon cracking is the process of breaking a long-chain of hydrocarbons into short ones by the breaking of carbon-carbon bonds. For example, cracking is the breakdown of large paraffins into smaller, more useful paraffins and olefins. Among several cracking processes in petrochemical industry, steam cracking (thermal cracking) of hydrocarbons which is non-catalytic process and fluid catalytic cracking (FCC) which is catalytic process using acidic zeolite catalysts are typical large scale important processes.

(I) Steam cracking of Naphtha

Steam cracking is the process by which hydrocarbon feeds are broken down to form light olefins, such as ethylene, propylene. The feedstock can vary from naphtha, liquefied petroleum gas (LPG), ethane, and other light paraffins. Naphtha has been a typical feedstock for light olefin production by steam cracking process in Japan.

Steam cracking of naphtha is proceeded in steam cracker as following [73]. Naphtha is vaporized with superheated steam and is passed into long, narrow tubes, which are made of chromium nickel alloys. Thermal cracking takes place mainly in the radiant section of the furnace, where tubes are externally heated to 1030 - 1173 K (up to 1373 K) by fuel oil or gas fired burners. After leaving the furnace, the hot gas mixture is subsequently quenched in the transfer line exchangers and temperatures can drop down to 573 K. These heat transfer activities avoid degradation by secondary reactions and at the same time generate high pressure steam for driving compressors, etc.

Depending on the severity [74], naphtha is cracked into smaller molecules via a free-radical mechanism in the absence of catalysts. The free radicals lead to the formation of light olefins, mainly ethylene in the gaseous state [75]. To cope with the requirements of higher-temperature and reduced residence time, the steam cracking process has been modified in various ways to improve energy efficiency, *e.g.*, the cracking furnace and heat recovery systems. However, marginal technological improvements cannot make further improvement in energy efficiency. The current steam cracking process uses as much as 40% of the energy consumed by the entire petrochemical industry. Therefore, global environmental issues have stimulated the development of processes that maximize energy and resource-savings and minimize CO_2 emissions. Besides, in the case of the current steam cracking process, it is difficult to control the composition of olefins formed. Hence, there is an increasing demand for processes capable of controlling the composition of olefins [63].

(II) Fluid catalytic cracking (FCC)

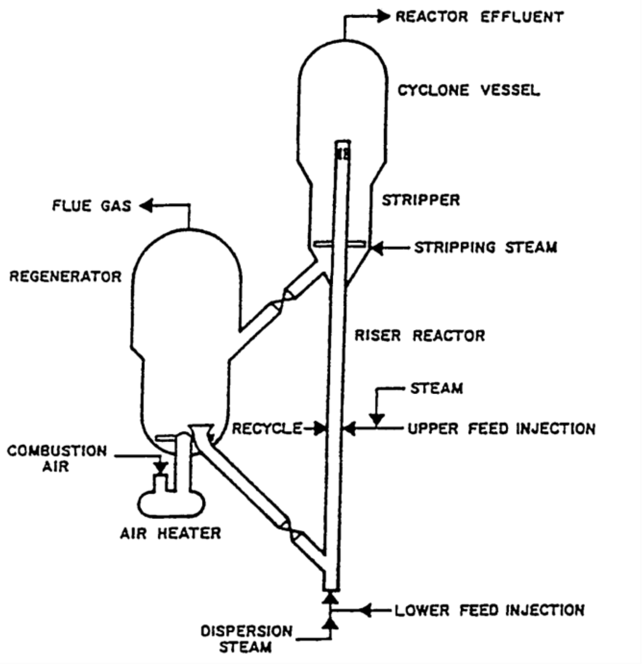

Figure 1.14 Typical FCC unit [76]

The FCC process converts heavy oil into valuable fuel products and petrochemical feedstocks involving light olefins [76]. The FCC process is the largest gasoline source within a refinery. The FCC process consists of a riser and a regenerator. The riser cracks the feed into valuable fuel products. The regenerator burns off the coke deposited on the catalyst during cracking in the riser. **A** simplified schematic of the process is shown in Fig. 1.14. Preheated feed injected at the bottom of the riser contacts hot active catalyst. The feed vaporizes and flows upward through the riser, together with the catalyst. During this time, the feed cracks and, in the process, the catalyst becomes deactivated by coke and feed metals. The residence time in the riser is in the range 2-10 **s** [77]. The riser top temperature is between 753 K and 843 K. Cracked products are separated from the coked catalyst by cyclones at the top of the riser and sent to a fractionation column. The coked catalyst is stripped of entrapped and other volatile hydrocarbons and sent to the regenerator. The regenerator is a hot, dense fluidized bed in which the coke on catalyst is burnt off. The typical catalyst residence time in the regenerator ranges from about 5 to 15 min. Combustion products and entrained catalyst are conveyed upward, out of the dense fluidized bed, into a dilute phase zone where cyclones separate the catalyst, which is returned to the bed. A typical FCC regenerator operates in turbulent fluidization and there is considerable carryover of catalyst to the cyclones. In fact, the whole bed circulates through the cyclones every 5 min [78]. The hot, nearly coke-free, regenerated catalyst is sent to the riser and contacts the feed, thereby completing the cycle. The hot regenerated catalyst provides the heat required for the endothermic cracking reactions, thereby maintaining the FCC unit in heat balance [76].

Commercial FCC catalysts consist of faujasite (Ultra-stable Y) and additives dispersed in an inorganic oxide matrix. Although the zeolite provides most of the cracking activity of the FCC catalyst, the matrix fulfills both physical and catalytic functions. Additives have physical characteristics that are similar to the cracking catalyst. They are typically blended in at concentrations of less than 10 wt%. For example, an additive containing the zeolite ZSM-5 may be used to boost gasoline octane and increase the yield of light olefins (mainly propylene).

Recently, the increasing demand for light olefins is directing many FCC units towards maximizing their yields. The FCC family technologies, such as MAXOFIN developed by Kellogg Brown & Root, Inc. (KBR) and Mobil Technology Company, UOP's PetroFCC, UOP's Fluidized Light Olefin Catalytic Cracking (FLOCC), ABB Lummus' Selective Catalytic Cracking (SCC), RIPP/Sinopec's Deep Catalytic Cracking (DCCI & II), RIPP/Sinopec's and Stone & Webster's Catalytic Pyrolysis Process (CPP), and Grace Davison's HPFCC (High Propylene Fluid Catalytic Cracking), have been commercialized and industrial plants are established based on the mentioned technologies [79-83]. Vacuum gas oil (VGO), VGO blended with residual oil, cocker gas oil, deasphalted oil, and atmospheric residue are among the industrial feedstocks used in these technologies [84-87]. The first five mentioned processes can yield up to 15–25 % propylene [84, 85], and in the former ones the combined yield of ethylene and propylene above 40% has been obtained [88, 89].

1-2-2 Mechanism of thermal cracking of paraffin

Thermal cracking of paraffins proceeds via a free-radical mechanism [75]. Consider *n*-hexane as a model straight-chain paraffin. At the cracking temperature thermal cleavage of carbon-carbon bonds occurs readily;

$$CH_3CH_2CH_2CH_2CH_2CH_3 \rightarrow CH_3CH_2CH_2\cdot + \cdot CH_2CH_2CH_3$$

This provides the initiation step for a free radical chain reaction. The radicals thus formed can undergo a series of β-scission reactions, each giving rise to a molecule of ethylene

$$CH_3CH_2CH_2\cdot \rightarrow CH_3\cdot + CH_2{=}CH_2$$

Hydrogen atom abstraction from a substrate molecule by a methyl or ethyl radical (or a hydrogen atom- see below) continues the reaction chain

$$CH_3\cdot + C_6H_{14} \rightarrow CH_4 + C_6H_{13}\cdot$$

Most molecules of substrate enter the reaction through hydrogen-atom abstraction rather than carbon-carbon cleavage. For both energetic and statistical reasons the radicals thus formed will be predominantly secondary radicals, and when these undergo β-scission, olefins other than ethylene will be produced;

$$CH_3CH_2CH_2CH_2CHCH_3 \rightarrow CH_3CH_2CH_2\cdot + CH_2{=}CHCH_3$$

The primary radical then produced can undergo further β-scissions producing ethylene.

$$CH_3CH_2CH_2\cdot \rightarrow CH_3\cdot + CH_2{=}CH_2$$

1-2-3 Mechanism of catalytic cracking of paraffin

The cracking of paraffin proceeds through the “monomolecular cracking” *via* the penta-coordinated carbonium ion mechanism and/or the classical “bimolecular cracking” *via* the carbenium ion/β-scission chain mechanism involving a hydride transfer reaction [90-96].

(I) Classical carbenium ion/β-scission chain mechanism (Bimolecular cracking)

In this mechanism, paraffin cracking proceeds via a carbenium ion as an intermediate, which undergoes a β-scission to form a small olefin and a smaller carbenium ion [93]. The latter ion can be transformed to a small paraffin by hydride transfer from a paraffin molecule, which then becomes a carbenium ion. In this way a reaction cycle is created [91].

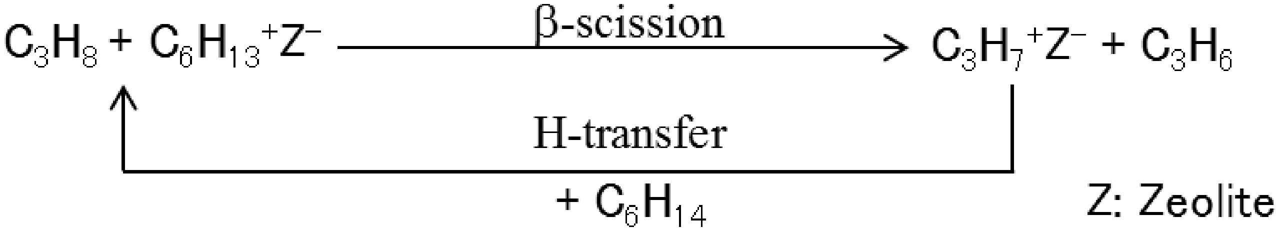

This mechanism is predominant at low reaction temperatures, high paraffin pressures, high conversions, wide reaction space and high Al content of zeolites [92]. In this mechanism, the hydrocarbons smaller than C2 are rarely formed because these products need to form via energetically unfavorable primary carbenium ions [90-92]. Therefore, the formation of propylene and butenes are easier than that of ethylene in this mechanism.

Several possibilities have been recognized for the initiation step leading to formation of carbenium ions. For example, olefines are protonated by the catalyst. There is no doubt that such protonations occur readily if olefins are present under cracking conditions, and the question is where they come from. They could be impurities in the feed, products of free-radical cracking (provided that the temperature is high enough), products of hydride abstraction from paraffins by Lewis acid sites on the catalyst, or products of cracking via carbonium ion mechanism [90].

(II) Penta-coordinated carbonium ion mechanism (monomolecular cracking)

In this mechanism, paraffin cracking proceeds via a penta-coordinated carbonium ion as an intermediate, which collapses to form a smaller paraffin or hydrogen and a carbenium ion [94]. The latter ion can be transformed to a small olefin by desorption or following β-scission, or to a small paraffin by hydride transfer from a paraffin molecule.

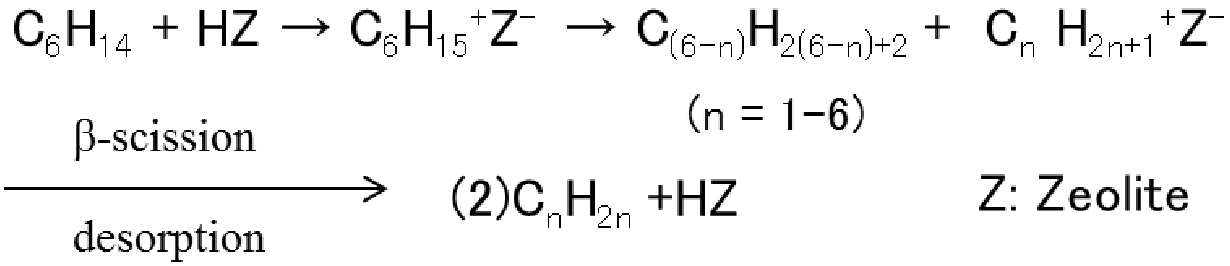

$$C_6H_{14} + HZ \rightarrow C_6H_{15}{}^{+}Z^{-} \rightarrow C_{(6-n)}H_{2(6-n)+2} + C_nH_{2n+1}{}^{+}Z^{-} \quad (n = 1-6)$$

$$\xrightarrow[\text{desorption}]{\beta\text{-scission}} (2)C_nH_{2n} + HZ \qquad Z\text{: Zeolite}$$

This mechanism is predominant at high reaction temperatures, low paraffin pressures, low conversions, narrow reaction space and low Al content of zeolites and requires the higher activation energy than the classical carbenium ion/β-scission chain mechanism [92]. In this mechanism, the product distribution will be very similar to that obtained by a radical- cracking mechanism, i.e. larger H_2, CH_4, C_2 [91].

1-2-4 Naphtha catalytic cracking for propylene production

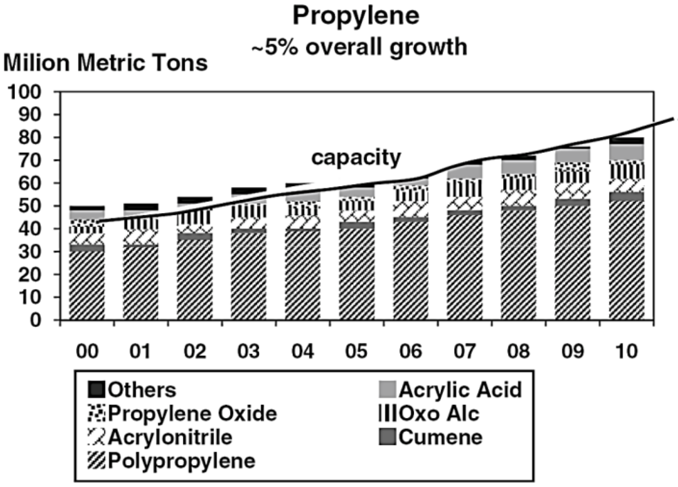

Figure 1.15 Expected market demands of propylene in the world [83]

Propylene is the key building block for the production of important petrochemicals, such as polypropylene, acrylonitrile, propylene oxide, cumene, phenol, isopropyl alcohol and many others [97]. As shown in Fig. 1.15, propylene worldwide demand has been increasing at an annual average of 5 % [83]. Currently, about 70% of propylene worldwide production comes from steam crackers, 28% from refinery fluid catalytic cracking (FCC) units and 2% from specific on purpose processes, such as propane dehydrogenation, metathesis and others. It is expected that in order to cover the future demand, the propylene market share from other processes than steam cracking will importantly grow, since it is forecast that propylene market will grow faster than ethylene market [98].

In comparison with the conventional steam cracking, the catalytic cracking of naphtha over acidic zeolite catalysts gives a high propylene/ethylene ratio at lower temperatures [63], since the transformation of long-chain paraffins to short-chain olefins occurs in some extent via the carbenium ion/β-scission mechanism. Therefore, using this process will reduce energy costs and provide selective production of propylene.

Various zeolites such as **FAU**, ***BEA**, **MOR**, **MWW**, **MFI, FER** and **MSE** types as cracking catalysts have been extensively investigated so far [99-103]. Among these zeolites, ZSM-5 with the **MFI** type structure has been recognized as a prime candidate for the practical catalytic cracking because of its high thermal and hydrothermal stabilities and its considerable resistance to deactivation by coking as well as its strong acidity [63, 64]. During the last decade, research scientists have focused on developing a number of modified ZSM-5 zeolites with tuned acidities and optimized control of the catalyst pore size to maximize the selectivities, and minimize the by product and coke formation [64].

1-3 Objects and outline of this thesis

In this thesis, I described influence of H-ZSM-5 properties on catalytic cracking of paraffins in order to design catalysts for naphtha catalytic cracking process. This thesis is begun with general introduction (this chapter) and is consist of two sessions and six chapters.

In the first session (chapter2 and chapter 3), I reported on the morphology control of H-ZSM-5 crystals and the influence of that on catalytic performance for *n*-hexane cracking which is a model reaction of naphtha cracking.

Chapter 2

I reported on the synthesis of nano-sized (~100 nm) H-ZSM-5 and the influence of crystallite sizes on the catalytic performance for *n*-hexane cracking. The influence of synthesis conditions on the crystallite size of ZSM-5 zeolite was examined. Then, different-sized H-ZSM-5 catalysts were used as catalysts for *n*-hexane cracking at 723-923 K in order to clarify the influence of crystallite size of H-ZSM-5 on catalytic properties; such as initial activity, selectivity and deactivation.

Chapter 3

I reported on the enlargement of external surface of H-ZSM-5 with different crystallite sizes by alkaline treatment (treatment with NaOH aqueous solution) and influence of external surface area on catalytic performance for *n*-hexane cracking. The influence of treatment conditions on external surface area and physicochemical properties of ZSM-5 zeolite were examined. Then, H-ZSM-5 catalysts with different external surfaces area were used as a catalyst for *n*-hexane cracking at 723-923 K in order to clarify the influence of external surface area of H-ZSM-5 on catalytic properties.

In another session (chapter4 and chapter 5), I reported on the influence of microstructure in H-ZSM-5 zeolite such as Si-O-Al angles and acid site location in the pores on paraffin cracking.

Chapter 4

I reported on the synthesis of H-ZSM-5 with different Al contents and influence of Al contents in ZSM-5 zeolites on Al distribution among 12 distinct T-site and on activity for *n*-hexane cracking. The influence of Al contents on Al state and Brønsted acid strength were examined. Then, H-ZSM-5 catalysts with different Al contents were used as a catalyst for *n*-hexane cracking at 673-923 K. The influence of Al state of H-ZSM-5 zeolite on catalytic activity for *n*-hexane cracking was discussed based on reaction mechanism.

Chapter 5

I reported on the synthesis of H-ZSM-5 with different acid site distributions in the pores and influence of acid site distributions on catalytic performance for paraffin cracking. The influence of the type of SDAs on acid site distributions on ZSM-5 zeolites were examined based on constraint index test. Then, H-ZSM-5 catalysts with different acid site distributions were used as a catalyst for C6 paraffins cracking at 623-673 K. The influence of acid site distributions of H-ZSM-5 zeolite and molecular size of paraffin on catalytic activity for paraffin cracking was investigated. Finally, I investigated deactivation of H-ZSM-5 with different acid site distributions for *n*-hexane and methylcyclohexane cracking at 923 K. I discussed deactivation behavior of H-ZSM-5 with different acid site distributions.

Finally, I summarized this thesis in chapter 6.

Reference

1. A. F. Cronstedt, Kongl Vetenskaps Academiens Handlingar Stockholm, 17 (1756) 120.
2. D. W. Breck, Zeolite Molecular Sieves; Wiley: New York, 1974.
3. R. M. Barrer, Hydrothermal Chemistry of Zeolites; Academic Press: London, 1982.
4. R. Szostak, Molecular Sieves - Principles of Synthesis and Identification, 1st ed.; Van Nostrand Reinhold: New York, 1989; 2nd ed.; Blackie: London, 1998.
5. S. T. Wilson, B. M. Lok, C. A. Messina, T. R. Cannan, E. M. Flanigen, J. Am. Chem. Soc., 104 (1982) 1146.
6. Ch. Baerlocher, L.B. McCusker, D.H. Olson, Atlas of Zeolite Framework Types, 6th revised edition , Elsevier, Amsterdam, 2007.
7. F. Liebau, Structural chemistry of silicates: structure, bonding, and classification, Springer-Verlag, Berlin (1985) 14.
8. D. S. Wragg, R. E. Morris, A. W. Burton, Chem. Mater., 20 (2008) 1561.
9. International Zeolite Association, Structure Commission, http://www.iza-structure.org/databases/.
10. R. M. Barrer, J. Chem. Soc. (1948) 127.
11. R. M. Barrer, L. Hinds, E. A. White, J. Chem. Soc. (1953) 1466.
12. R. L. Wadlinger, G. T. Kerr, E. J. Rosinski, U.S. Patent 3,308,069, 1967.
13. R. J. Argauer, G. R. Landolt, U.S. Patent 3,702,886, 1972.
14. Ch. Baerlocher, W. M. Meier, Helu. Chim. Acta. 52 (1969)1853.
15. M. E. Davis, R.F. Lobo, Chem. Mater., 4 (1992) 756.
16. Stud. Surf. Sci. Catal. (1991) 58; (2001) 137.
17. Stud. Surf. Sci. Catal. (1994) 85.
18. C. S. Cundy, P.A. Cox, Chem. Rev., 103 (2003) 663.
19. C. D. Chang, A. T. Bell, Catal. Lett., 8 (1991) 305.
20. S. L. Burkett, S. L. M. E. Davis, J. Phys. Chem., 98 (1994) 4647.
21. S. L. Burkett, S. L. M. E. Davis, Chem. Mater., 7 (1995) 920.
22. S. L. Burkett, S. L. M. E. Davis, Chem. Mater., 7 (1995) 1453.
23. R. Ravishankar, C. Kirschhock, B. J. Schoeman, P. Vanoppen, P. J. Grobet, S. Storck, W. F. Maier, J. A. Martens, F. C. De Schryver, P. A. Jacobs, P. A. J. Phys. Chem. B, 102 (1998) 2633.
24. R. Ravishankar, C. E. A. Kirschhock, P.-P. Knops-Gerrits, E. J. P. Feijen, P. J. Grobet, P. Vanoppen,

F. C. De Schryver, G. Miehe, H. Fuess, B. J. Schoeman, P. A. Jacobs, J. A. Martens, J. Phys. Chem. B, 103 (1999) 4960.

25. C. E. A. Kirschhock, R. Ravishankar, F. Verspeurt, P. J. Grobet, P. A. Jacobs, J. A. Martens, J. Phys. Chem. B, 103 (1999) 4965.
26. C. E. A. Kirschhock, R. Ravishankar, F. L. Van Looveren, P. A. Jacobs, J. A. Martens, J. Phys. Chem. B, 103 (1999) 4972.
27. C. E. A. Kirschhock, R. Ravishankar, P. A. Jacobs, J. A. Martens, J. Phys. Chem. B, 103 (1999) 11021
28. B. J. Schoeman, Zeolites, 18 (1997) 97.
29. W. Vermeiren, J.-P. Gilson, Top. Catal., 52 (2009) 1131.
30. W. J. Mortier, Proc. 6th Zeolite Conf., (1984) 734.
31. J. A. Rabo, G. J. Gajda, Catal. Rev.-Sci. Eng., 31 (1989–1990) 385.
32. J. A. Martens, W. Souverijns, W. Van Rhijn, P. A. Jacobs, in Handbook of Heterogeneous Catalysis, 1 (1997) 324.
33. M. Greger, B. Gutsche, L. Jeromin, Chem. Ing. Tech., 64(3) (1992) 253.
34. P. B. Weisz, V. J. Frilette, J. Phys. Chem., 64 (1960) 382.
35. N. Y. Chen, W. E. Garwood, F. G. Dwyer, Shape Selective Catalysis in Industrial Applications, Chemical industries, 36 (1989).
36. S. M. Csicsery, J. Catal., 19 (1970) 394.
37. S. M. Csicsery, J. Catal., 23 (1971) 124.
38. W. O. Haag, R. M. Lago, P. B. Weisz, Faraday Discuss. Chem. Soc., 72 (1981) 317.
39. S. M. Csicsery, Zeolites, 4(3) (1984) 202.
40. J. A. Martens, J. Pérez-Pariente, E. Sastre, A. Corma, P. A. Jacobs, Appl. Catal., 45 (1988) 85.
41. V. J. Frilette, W. O. Haag, R. M. Lago, J. Catal., 67 (1981) 218.
42. W. O. Haag, R. M. Lago, P. B. Weisz, Faraday Discuss. Chem. Soc., 72 (1981) 317.
43. S. I. Zones, T. Harris, Micropor. Mesopor. Mater., 35 (2000) 31.
44. J. R. Carpenter, S. Yeh, S. I. Zones, M. E. Davis, J. Catal., 269 (2010) 64.
45. A. B. Pinar, C. Márquez-Álvarez, M. Grande-Casas, J. Pérez-Pariente, J. Catal., 263 (2009) 258.
46. N. J. Turro, X.-G. Lei, W. Li, Z. Liu, A. McDermott, M.F. Ottaviani, L. Abrams, J. Am. Chem. Soc., 122 (2000) 11649.
47. E. M. Flanigen, J. M. Bennett, R. W. Grose, J. P. Cohen, R. L. Patton, R. M. Kirchner, J. V. Smith, Nature, 271 (1978) 512.

48. G. D. Price, J. J. Pluth, J. V. Smith, J. M. Bennett, R. L. Patron, J. Am. Chem. Soc., 104 (1982) 5971.
49. K. J. Chao, J. C. Lin, Y. Wang, G. H. Lee, Zeolites, 6 (1986) 35.
50. B. M. Lok, T.R. Cannan, C.A. Messina, Zeolites, 3 (1983) 282.
51. N. Y. Chen, W.E. Garwood, F.G. Dwyer, Shape Selective Catalysis in Industrial Applications, second ed. Marcel Dekker, New York, 1996.
52. C. Knottenbelt, Catal. Today, 71 (2002) 437.
53. W. Lieber, M. Wagner, Erdoel Erdgas Kohle, 120 (2004) 323.
54. C. Ringelhan, G. Burgfels, J. G. Neumayr, W. Seuffert, J. Klose, V. Kurth, Catal. Today, 97 (2004) 277.
55. S. Zinger, Petroleum Technology Quarterly, 10(4) (2005) 125.
56. W. Vermeiren, D. H. Wei, R. B. James, J. M. Andersen, Hydrocarbon Eng 8(10) (2003) 79.
57. U. Koss, Hydrocarbon Eng, (1999) 66.
58. P. A. Ruziska, T. R. Steffens, AIChE Spring meeting, Houston, 2001.
59. T. Tsunoda, M. Sekiguchi, Catal. Surv. Asia, 12 (2008) 1.
60. M. Tallman, S. Borsos, EPTC, Prague, 2000.
61. J. Teng, Z. Xie, ERTC petrochemical conference, Brussels, 2007.
62. P. B. Venuto, E. T. Habib, Fluid catalytic cracking with zeolite catalysts. Marcel Dekker, Inc., New York, 1979.
63. Y. Yoshimura, N. Kijima, T. Hayakawa, K. Murata, K. Suzuki, F. Mizukami, K. Matano, T. Konishi, T. Oikawa, M. Saito, T. Shiojima, K. Shiozawa, K. Wakui, G. Sawada, K. Sato, S. Matsuo, N. Yamaoka, Catal. Surv. Jpn., 4 (2000) 157.
64. N. Rahimi, R. Karimzadeh, Appl. Catal. A: Gen., 398 (2011) 1.
65. C. Eng, AIChE Spring national neeting, Houston, 2007.
66. H. Koempel, W. Liebner, Stud. Surf. Sci. Catal., 167 (2007) 261.
67. L. Wang, L. Tao, M. Xie, G. Xu, J. Huang, Y. Xu, Catal. Lett., 21 (1993) 35.
68. K. Honda, X. Chen, Z-G. Zhang, Appl. Catal. A: General, 351 (2008) 122.
69. T. F. Degnan Jr., C. M. Smith, C.R. Venkat, Appl. Catal. A: General, 221 (2001) 283.
70. C. Perego, P. Ingallina, Catal. Today, 73 (2002) 3.
71. J. P. Breen, R. Burch, M. Kulkarni, D. McLaughlin, P.J. Collier, S.E. Golunski, Appl. Catal. A: General, 316 (2007) 53.
72. P. Dejaifve, A. Auroux, P. C. Gravelle, J. C. Vedrine, Z. Gabelica, and E. Derouane, Catal., 70 (1981)

123.

73. T. Ren, M. Patel, K. Blok, Energy, 31 (2006) 425.
74. M. Golombok, J. Bijl, M. Kornegoor, Ind. Eng. Chem. Res., 40 (2001) 470.
75. P. Wiseman, J. Chem. Educ., 54 (1977) 154
76. W.-C. Cheng, G. Kim, A.W. Peters, X. Zhao, K. Rajagopalan, Catal. Rev.-Sci. Eng., 40 (1998) 39.
77. J. J. Blazek, Catdugram, 42 (1973) 3.
78. A. A. Avidan, R. Shinnar, Ind. Eng. Chem. Res., 29 (1990) 931.
79. R. B. Miller, P. K. Niccum, A. Claude, M. A. Silverman, N. A. Bhore, G. K. Chitnis, S. J. McCarthy, K. Liu, NPRA Annual Meeting, San Francisco, California, USA, 1998.
80. PetroFCC Process, 9/30/2010, http://www.uop.com/lightolefins/5037.html.
81. J.S. Plotkin, Catal. Today, 106 (2005) 10.
82. A.G. Maadhah, Y. Fujiyama, H. Redhwi, M. Abul-Hamayel, A. Aitani, M. Saeed, C. Dean, Arab. J. Sci. Eng., 33 (2008) 17.
83. Y.-K. Park, C.W. Lee, N.Y. Kang, W.C. Choi, S. Choi, S.H. Oh, D.S. Park, Catal. Surv. Asia, 14 (2010) 75.
84. W. Xieqing, X. Chaogang, L. Zaiting, Z. Genquan, Practical Advances in Petroleum Processing, Springer, 2006.
85. PEP Report 248, Steam Cracking for Olefins Production, 2003.
86. R. Deng, F. Wei, Y. Jin, Q. Zhang, Y. Jin, Chem. Eng. Technol., 25 (2002) 711.
87. X. Meng, C. Xu, J. Gao, L. Li, Appl. Catal. A: Gen., 294 (2005) 168.
88. Zai-Ting, X. Chao-Gang, Z. Zhi-Gang, Z. Jiu-shun, 17th World Petroleum Congress, Rio de Janiero, Brazil, 2002.
89. H. Xie, X. Wang, Z. Guo, Q. Wei, 17th World Petroleum Congress, Rio de Janeiro, Brazil, 2002.
90. A. Corma, A.V. Orchillés, Micropor. Mesopor. Mater., 35 (2000) 21.
91. S. Kotrel, H. Knözinger, B.C. Gates, Micropor. Mesopor. Mater., 35 (2000) 11.
92. A. F. H. Wielers, M. Waarkamp, M.F.M. Post, J. Catal., 127 (1991) 51.
93. B.S. Greensfelder, H.H. Voge, G.M. Good, Ind. Eng. Chem., 41 (1949) 2573.
94. W. O. Haag, R. M. Dessau, Proc. 8th Int. Congr. Catalysis. Berlin, 2 (1984) 305.
95. W. O. Haag, R. M. Dessau, R. M. Lago, Stud. Surf. Sci. Catal., 60 (1991) 255.
96. H. Krannila, W. O. Haag, B. C. Gates, J. Catal., 135 (1992) 115.
97. Petrochemical processes, 99 (1999) 85.

98. A. Corma, F.V. Melo, L. Sauvanaud, F. Ortega, Catal. Today, 107-108 (2005) 699.

99. A. Corma, V. GonzBlez-Alfaro, A. V. Orchillks, Appl. Catal. A: Gen., 129 (1995) 203.

99. A. Corma, J. Martinez-Triguero. J. Catal., 165 (1997) 102.

100. S. Inagaki, K. Takechi, Y. Kubota, Chem. Commun., 46 (2010) 2662.

101. T. Komatsu, H. Ishihara, Y. Fukui, T. Yashima – Appl. Catal. A: Gen., 214 (2001) 103.

102. T. Komatsu, 20th Annual Saudi-Japan Symposium; Catalysts in Petroleum Refining and Petrochemicals, Dharan, Saudi-Arabia, 2010.

Chapter 2

Control of crystallite size of H-ZSM-5 zeolites and their catalytic properties for cracking of *n*-hexane

2-1 Abstract

Nano-sized H-ZSM-5 (*ca.* ~65 nm) was successfully prepared by mixing the mother gel under mild conditions before crystallization. Furthermore, a facile control of the crystallite size of the H-ZSM-5 catalyst was achieved merely by changing the amount of water in the mother gel. Three different-sized H-ZSM-5 catalysts were used as a catalyst for *n*-hexane cracking at 723-923 K. The crystallite size of H-ZSM-5 little affected the initial activity, but affected the deactivation rate considerably. The reduction in the crystallite size of the H-ZSM-5 catalysts contributes to the slow deactivation, probably because the H-ZSM-5 with a smaller crystallite size is less sensitive to deactivation by pore blocking by coke formed.

2-2 Introduction

H-ZSM-5 with the **MFI** type structure has been recognized as a prime candidate for the practical catalytic cracking of naphtha because of its high thermal and hydrothermal stabilities and its considerable resistance to deactivation by coking as well as its strong acidity [1,7-14]. However, the catalytic performance is strongly affected by coke formation. The coke fouls the catalytic surfaces and blocks the micropores, resulting in the catalytic deactivation. Especially, zeolite catalysts often exhibit insufficient activity and fast deactivation mainly due to poor diffusion efficiency by coking. It is expected that if the nano-sized zeolite instead of the micro-sized one is used as a catalyst, the catalytic activity and catalyst deactivation rate may be improved considerably.

Recently, uniformly nano-sized zeolites with sizes less than 100 nm have been receiving much attention, showing the better catalytic and adsorptive properties than micron sized ones because of efficient mass transport of guest molecules [3-6]. Nano-sized zeolites have been prepared by several routes. For example, nanocrystals of zeolites such as **MFI**-, **BEA**-, **LTA**-, **FAU**- and **SOD**-type ones were synthesized from clear solutions containing zeolite precursors [7-15]. An emulsion system containing surfactants has also been employed to preparing **MFI** and **MOR** nanocrystals [16, 17]. The "confined space synthesis" method using *e.g.*, porous carbon as a template has led to the synthesis of various nanosized zeolites [18]. However, these methods require some organic additives and/or the porous carbon template. Therefore, the development of a simpler method has been desired.

Recently, we have developed a method for preparing the colloidal dispersion containing the nano-sized silicalite-1 with the **MFI t**opology [19]. Our strategy is to enhance the nucleation by stirring the mother gel at 353 K for 24 h before crystallization; this mixing process was designated as "pre-aging process". We have considered that the nucleation before crystallization produces a large number of particles, leading to the formation of the smaller-sized zeolite crystallites.

In this chapter, first, we will report on the facile control of the crystallite size of ZSM-5 based on the pre-aging process. Then, the different-sized ZSM-5 catalysts will be applied as a solid acid catalyst for catalytic cracking of *n*-hexane to clarify the effect of the crystallite size on the catalytic performance.

2-3 Experimental

2-3-1 Synthesis of different-sized ZSM-5 catalysts

The ZSM-5 samples with different crystallite sizes were prepared as follows. Tetraethyl orthosilicate (TEOS, Tokyo Kasei, >96 %) was added to the solution containing water, tetrapropylammonium hydroxide (TPAOH, 25 % aqueous solution, Tokyo Kasei). The resulting mixture was stirred at 353 K for 24 h. Thereafter, the solution containing water, $Al(NO_3)_3•9H_2O$ (Wako, 99.9 %) and NaOH (Wako, 97 %) was added to the mixture. Thus prepared mother gel was crystallized at 443 K for 24 h. The molar composition of the final gel was 1 SiO_2: 0.01 Al_2O_3: 0.25 TPAOH: 0.05 Na_2O: 8.3-100 H_2O. Then, the solid product was collected by centrifugation. The Na-type ZSM-5 (Na-ZSM-5) samples were obtained by calcination of the as-synthesized sample in an oven at 823 K to remove TPA^+ species. The effects of the amount of water in the gel and the conditions of the pre-aging process were examined.

The H-type ZSM-5 (H-ZSM-5) samples were obtained as follows. The calcined Na-ZSM-5 samples were treated with 1 M NH_4NO_3 (Wako, 99.0+%) aq. at 353 K for 3 h twice followed by calcination at 823 K for 10 h to exchange Na^+ ions for protons.

2-3-2 Characterizations

Field-emission scanning electron microscopic (FE-SEM) images of the powder samples were obtained on an S-5200 (Hitachi) microscope operating at 1-30 kV. The samples for FE-SEM observations were mounted on a carbon-coated microgrid (Okenshoji Co.) without any metal coating. XRD patterns were collected on a Rint-UltimaⅢ (Rigaku) using a Cu Kα X-ray source (40 kV, 20 mA). Nitrogen adsorption-desorption measurements to obtain information on the micro- and meso-porosities were conducted at 77 K on a Belsorp-miniⅡ (Bel Japan). The BET (Brunauer-Emmett-Teller) specific surface area (S_{BET}) was calculated from the adsorption data in the relative pressure ranging from 0.04 to 0.2. External surface area (S_{EXT}) was estimated by the *t*-plot method. Elemental analyses of the samples (Si/Al ratio) were performed on an inductively coupled plasma-atomic emission spectrometer (ICP-AES, Shimadzu ICPE-9000). Temperature-programmed desorption of ammonia (NH_3-TPD) spectra were recorded on Multitrack TPD equipment (Japan BEL). Typically, 25 mg catalyst was pretreated at 773 K in He (50 mL min^{-1}) for 1 h and then was cooled to adsorption temperature of 373 K. Prior to the adsorption of NH_3, the sample was evacuated. Approximately 2500 Pa of NH_3 was allowed to make contact with the sample for 10 min. Subsequently, the sample was evacuated to remove weakly adsorbed NH_3 for 30 min. Finally, the sample was heated from 373 to 873 K at a ramping rate of 10 K

min^{-1} with the He flow (50 mL min^{-1}) passed through the reactor. A mass spectrometer was used to monitor desorbed NH_3 (m/e = 16). The amount of acid sites was determined by using the area of the so-called ‘‘h-peak’’ [32] in the profiles. Solid-state ^{27}Al magic-angle spinning (MAS) NMR spectra were obtained with $\pi/2$ pulse width of 6 μs and pulse delay of 5 s on a JEOL ECA-400 spectrometer. Al resonance frequency employed was at 104 MHz and the sample spinning rate speed was 5.3 kHz. ^{27}Al chemical shifts were referenced to a saturated $Al(NO_3)_3$ solution.

2-3-3 Catalytic cracking of *n*-hexane

The H-ZSM-5 zeolites with various crystallite sizes were used as catalysts for the catalytic cracking of *n*-hexane (Wako, 96.0+%). The cracking of *n*-hexane was carried out in a 6 mm quartz tubular flow microreactor loaded with 10 to 100 mg of 50/80 mesh zeolite pellets without a binder. The catalyst was centered at the reactor in a furnace. The catalyst was calcined at 923 K for 1 h prior to the reaction, and then the reactor was cooled to the desired reaction temperatures (723-923 K). The initial partial pressure of *n*-hexane was set at 6 or 23 kPa. He was used as a carrier gas. The catalyst weight to the flow rate ratio ($W/F_{n\text{-hexane}}$) was varied from 2.5 to 32 g-cat h/mol-*n*-hexane. The weight hourly space velocity of *n*-hexane (WHSV) was varied from 2.7 to 70 h^{-1}.

The reaction products were analyzed with an on-line gas chromatograph (Shimadzu GC-2014) with an FID detector and a capillary column (PLOT Fused Silica 30 m×0.53 mm, 6μm film thickness). The selectivities to the products and the *n*-hexane conversion were calculated based on the carbon numbers. Coke amount was calculated by thermogravimetry (TG). The weight loss from 673 to 1073 K in each TG profile was defined as the contents of coke on used catalyst.

2-4 Results and discussion

2-4-1 Preparation of different-sized H-ZSM-5

The XRD patterns of the products synthesized with the molar ratio of the H_2O/Si in the gel varied from 8.3 to 100 are shown in Fig. 2.1, indicating that all the products have a pure **MFI** phase. The molar ratio of the H_2O/Si in the gel hardly affected the crystallinity. The morphology of the products was evaluated by FE-SEM observations (Fig. 2.2). The crystallites were mono-dispersed in every case and the crystallite size was decreased with a decrease in the molar composition of water; *e.g.*, the average sizes were found to be 106, 253, 380 and 935 nm for the H_2O/Si ratio of 8.3, 30, 40 and 100, respectively.

Typical "coffin-shaped" particles were formed when the water compositions were over 30. Thus, the different-sized ZSM-5 nanocrystals are successfully prepared by changing the amount of water. Persson and co-workers have reported that higher alkalinity favored the nucleation of a large number of particles, forming the smaller-sized zeolite [8]. One of the reasons is that crystallite size of H-ZSM-5 is reduced with the increase in the pH which leads to the formation of ZSM-5 nanocrystals.

The S_{BET} was increased with a decrease in the crystallite size; the S_{BET} was found to be about 370, 390, 399 and 403 $m^2 \cdot g^{-1}$ for the samples with the average size of 935, 380, 253 and 106 nm, respectively. The S_{EXT} was also increased with a decrease in the crystal size (Table 2.1). The internal (micropore) surface areas, which are defined as the difference between S_{BET} and S_{EXT}, are fairly similar for all the products (ca. 350 m^2/g).

The yields of the products were over 80 % irrespective of the molar ratio of the H_2O/Si in the gel. The ICP analyses showed that the Si/Al atomic ratios of the products were almost the same regardless of the crystallite size (Si/Al = ca. 50). The acid amounts estimated by the NH_3-TPD analyses of H-ZSM-5 catalysts were fairly similar for all the products (ca. about 0.3 mmol/g). The ^{27}Al MAS NMR spectra exhibited a sharp peak at 58 ppm, which is assigned to tetrahedrally coordinated aluminium in the framework, regardless of the crystallite size (Fig. 2.3). No product demonstrated a marked peak at 0 ppm assigned to octahedrally coordinated aluminium.

At the H_2O/Si molar ratio = 8.3, the product which was well-crystallized ZSM-5 with particle size of ca. 100 nm was obtained, when the pre-aging process was applied not before but after the addition of the aqueous solution containing $Al(NO_3)_3$ and NaOH. The crystallite size of the product was ca. 100 nm and almost the same as that of ZSM-5 prepared normally. This result suggests that the timing of the pre-aging process hardly affects the properties of the products.

The control of the Si/Al ratio in the nano-sized H-ZSM-5 about 100 nm in size was attempted by changing the amount of the Al and Na sources introduced into the mother gel. As a result, the Si/Al ratio was controlled ranging from ∞ to 50 when the Si/Al ratio of the mother gel was changed from ∞ to 50. The crystallinity, morphology and Al coordination state were not remarkably changed when the Si/Al ratio was varied in this range. When the Si/Al ratio in the mother gel was further decreased, the crystallite size was increased; at a Si/Al ratio of 25 in the mother gel, the H-ZSM-5 sample 150 nm in size was obtained with the Si/Al ratio in the product almost similar to that in the mother gel.

2-4-2 Conditions of the pre-aging process

Our method for preparing the H-ZSM-5 nanocrystals includes the “pre-aging process” where the synthesis gel is stirred at 353 K for 24 h before crystallization. Thereupon, the effects of the pre-aging temperature and time were investigated.

First, at a pre-aging temperature of 353 K, the effect of the pre-aging time was examined. Figure 2.4 shows the FE-SEM images of the products synthesized with the pre-aging time varied ranging from 0 to 96 h, indicating that the crystallite size was decreased with an increase in the pre-aging time; the average crystallite sizes of the products at the pre-aging time of 0, 12, 24 and 96 h were found to be 924, 154, 106 and 65 nm, respectively. Second, at a pre-aging time of 24 h, the effect of pre-aging temperature was examined. The average crystallite sizes of the products at the pre-aging temperature of 298, 333, 353 and 373 K were found to be 270, 176, 106 and 110 nm, respectively (Fig. 2.5).

The pre-aging process with short time and/or low temperature did not give nano-sized crystals. This is probably because such conditions do not enhance the nucleation before the crystallization process, resulting in the larger-sized crystals. In contrast, long time and/or high temperature conditions enhance the nucleation during the aging process. In addition to the small amount of water in the synthesis gel, increasing concentration of the silicate species may make the nucleation take place more readily. However when the pre-aging temperature was raised from 353 to 373 K, the average crystallite sizes was slightly increased from 106 to 110 nm. This result could be accounted for by assuming that not only the nucleation but also the crystal growth takes place at 373 K. For these reasons, the small amount of water in the synthesis gel and the optimized pre-aging process are indispensable for preparing the ZSM-5 nanocrystals.

Thus the H-ZSM-5 zeolites with different crystallite sizes (65 nm - 1 μm) are successfully synthesized by controlling the amount of water in the starting gel, pre-aging time and pre-aging temperatures.

2-4-3 Catalytic cracking of *n*-hexane over different-sized H-ZSM-5 catalysts

The three different-sized H-ZSM-5 catalysts were examined for the catalytic cracking of *n*-hexane; the crystallite sizes were *ca*. 1000, 400 and 100 nm, which were synthesized with the H_2O/Si ratios set at 100, 40 and 8.3, respectively, and denoted by L, M and S, resepctively. The structural and physicochemical properties are listed in Table 2.2. These samples had similar physicochemical properties except for the crystallite size.

First, the influence of the reaction temperature on the catalytic performances was investigated. Figure 2.6 shows the results of cracking of *n*-hexane over the three different-sized H-ZSM-5 catalysts at 723 to 923 K. It should be noted that the thermal cracking of *n*-hexane took place without catalyst, the conversion of *n*-hexane being 0, 2.6 and 7.8%, at 723, 823 and 923 K, respectively. The conversion of *n*-hexane was increased along with the reaction temperature irrespective of the crystallite size of the catalysts; the conversion for every catalyst was *ca.* 25, 70 and 100% at the reaction temperature of 723, 823 and 923 K, respectively. Haag and co-workers also have reported that crystallite size does not affect the activity on for *n*-hexane cracking over H-ZSM-5 at 811 K [21]. This result indicates that the cracking of *n*-hexane over H-ZSM-5 is not limited by diffusion of *n*-hexane under the present reaction conditions. The slight differences in the behavior of the products distributions depending on the crystallite size were observed; the smaller-sized catalysts gave the lower selectivities to propylene and butenes (1-butnene, 2-butenes and isobutene) and higher ones to ethylene and BTX (benzene, toluene and xylenes). When the reaction temperature was increased, the selectivities to propylene and butenes were decreased (*e.g.*, the selectivity of propylene was 37, 35 and 26% at the reaction temperature of 723, 823 and 923 K, respectively.), while those to ethylene and BTX were increased. With increasing reaction temperature, propylene and butenes once formed are gradually transformed into aromatic compounds, resulting in the decrease in the selectivities to propylene and butenes accompanied with the increase in the selectivity to BTX. The selectivity to ethylene was low compared with other olefins at low temperatures. Ethylene is formed via energetically unfavorable primary carbenium ions, regardless of the monomolecular or bimolecular mechanism [22, 23] and therefore the apparent activation energy for ethylene formation should be high, resulting in the steep increase in the ethylene selectivity with an increase in reaction temperature.

Second, the influence of W/F on the catalytic performance of the three different-sized H-ZSM-5 catalysts was examined at 873 K, where the thermal cracking of *n*-hexane took place only slowly (Fig. 2.7). The changes in the conversion and the products distributions caused by an increase in W/F were fairly similar to those caused by an increase in the reaction temperature. The selectivities to propylene and butenes were decreased and those to ethylene and BTX were increased along with increasing W/F.

2-4-4 Effect of crystallite size on the deactivation

The changes in the conversion and the selectivities along with the time-on-stream were examined under a higher initial pressure of *n*-hexane of 23 kPa, which should lead to the faster deactivation. The conversion of *n*-hexane by thermal cracking was 10.2 % under these reaction conditions. Note that the initial conversion of *n*-hexane was almost the same (ca 75 %) regardless of the crystallite sizes (Fig. 2.8 (A)). The conversion was decreased along with the reaction time. The deactivation became faster with an increase in the crystallite size. The selectivities to ethylene, propylene and other products are shown in Fig. 2.8 (B), showing that no marked difference in the selectivities among three catalysts is observed. The propylene/ethylene ratio was decreased with an increase in the conversion for every catalyst.

Assuming that the catalytic cracking of *n*-hexane obeys the first-order kinetics [22] and the deactivation rate is in proportion to the first order rate constant, the deactivation rate should be expressed as follows:

$$-dk_c / dt = k_d k_c \qquad (1)$$

$$k_d t = \ln k_{c0} - \ln k_c \qquad (2)$$

where k_c is the rate constant for catalytic cracking, k_d is the rate constant for deactivation, and t is time on stream and k_{c0} is the k_c at $t = 0$. In Fig. 2.9, ln k_c is plotted against time on stream, t, indicating that linear relationships are observed irrespective of the crystallite size. The k_d values for the S, M and L catalysts based on the equation (2) are 0.0171, 0.0242 and 0.0327 h^{-1}, respectively. The reduction in the crystallite size of the H-ZSM-5 catalysts contributed to the slow deactivation.

The relationship between the reaction time and the amount of coke formed, which was estimated by TG-DTA analyses (Fig. 2.10 (A)), indicates that the formation rate of coke was increased along with the crystallite sizes. The formation of coke resulted in the decrease in the conversion (Fig. 2.10 (B)). On the large-sized catalyst, the blocking of the zeolite pores seriously occurred by the deposition of coke, giving rise to the high diffusional resistance of the products as well as the reactant, and as a result, the catalytic activity decreased. On the other hand, in the smaller-sized catalyst, the products would easily diffuse out from the pore, suppressing the formation of coke on the external surface and/or in the pore, and as a result the deactivation was mitigated. It is noteworthy that, with similar amounts of coke deposited, the smaller-sized catalyst suffered from less deactivation than the larger-sized catalyst. This fact is caused by the increase in the number of pore entrances caused by the decrease in the crystallite size. The larger number of pore entrances should retard the deactivation resulting from pore blocking by coke formed during the reaction.

2-5 Conclusions

The H-ZSM-5 zeolites with different crystallite sizes (65 nm - 1 μm) were successfully synthesized by controlling the amount of water in the starting gel. Both the optimized pre-aging process and the small amount of water in the synthesis gel are indispensable for preparing the ZSM-5 nanocrystals. The small-sized H-ZSM-5 catalyst showed a better catalytic performance compared to the medium- and large- sized H-ZSM-5 catalysts. The reduction in the crystallite size of the ZSM-5 catalysts suppressed the formation of coke on the surface and/or in the pore, contributing to the slow deactivation.

References

1. Y. Yoshimura, N. Kijima, T. Hayakawa, K. Murata, K. Suzuki, F. Mizukami, K. Matano, T. Konishi, T. Oikawa, M. Saito, T. Shiojima, K. Shiozawa, K. Wakui, G. Sawada, K. Sato, S. Matsuo, N. Yamaoka, Catal. Surv. Jpn., 4 (2000) 157.
2. N. Rahimi, R. Karimzadeh, Appl. Catal. A: Gen., 398 (2011) 1.
3. D. Chen, K. Moljord, T. Fuglerud, A. Holmen, Micropor. Mesopor. Mater., 29 (1999) 191.
4. M. Firoozi, M. Baghalha, M. Asadi, Catal. Commun., 10 (2009) 1582.
5. P. Botella, A. Corma, J. M. López-Nieto, S. Valencia, and R. Jacquoty, J. Catal. 195 (2000) 161.
6. M. A. Arribas, A. Martínez, Catal. Today, 65 (2001) 117.
7. L. Tosheva, V. P. Valtchev, Chem. Mater., 17 (2005) 2494.
8. A. E. Persson, B. J. Schoeman, J. Sterte, J. E. Otterstedt, Zeolites, 14 (1994) 557.
9. J. Kobler, J. Abrevaya, S. Mintova, T. Bein, J. Phys. Chem. C., 112 (2008) 14274.
10. W. Fan, K. Morozumi, R. Kimura, T. Yokoi, T. Okubo, Langmuir, 24 (2008) 6952.
11. D. E. Kuechl, A.I. Benin, L. M. Knight, H. Abrevaya, S.T. Wilson, W. Sinkler, M. Mezza, R. R. Willis, Micropor. Mesopor. Mater., 127 (2010) 104.
12. M. A. Camblor, A. Corma, A. Mifsud, J. Perez-Pariente, S. Valencia, Stud. Surf. Sci. Catal., 105 (1997) 3411.
13. P. Sharma, P. Rafaram, R. Tomar, J. Colloid Interface Sci., 325 (1997) 547.
14. O. Larlus, S. Mintova, T. Bein, Micropor. Mesopor. Mater., 96 (2006) 405.
15. V. P. Valtchev, L. Tosheva, K. N. Bozhilov, Langmuir., 21 (2005) 10724.
16. T. Tago, M. Nishi, Y. Kouno, T. Masuda, Chem. Lett., 33 (2004) 1040.
17. T. Tago, D. Aoki, K. Iwakai, T. Masuda, Top. Catal., 52 (2009) 865.
18. C. Madsen, C. J. H. Jacobsen, Chem. Commun., (1999) 673.
19. R. Watanabe, T. Yokoi, T. Tatsumi, J. Colloid Interface Sci., 356, 2 (2011) 434.
20. M. Niwa, K. Katada, Catal. Surv. Jpn., 1 (1997) 215.
21. W. O. Haag, R. M. Lago, P. B. Weisz, Faraday Discuss. Chem. Soc., 72 (1981) 317.
22. W. O. Haag, R. M. Dessau, R. M. Lago, Stud. Surf. Sci. Catal., 60 (1991) 255.
23. H. Krannila, W. O. Haag, B. C. Gates, J. Catal., 135 (1992) 115.

Table 2.1 Physicochemical properties of the sample synthesized in the various amount of added water

H_2O/Si	**Particle size**[a)] nm	**S_{BET}**[b)] $m^2\ g^{-1}$	**S_{EXT}**[c)] $m^2\ g^{-1}$	**V_{micro}**[d)] $ml\ g^{-1}$	**V_{meso}**[e)] $ml\ g^{-1}$
100	935	370	12	0.16	0.08
40	380	399	32	0.18	0.11
30	253	400	40	0.17	0.11
8.3	106	403	49	0.17	0.39

a) Particle size: Estimated by the FE-SEM.

b) S_{BET}: BET surface area

c) S_{EXT}: External surface area

d) V_{micro}: Micropore volume

e) V_{meso}: Mesopore volume

Table 2.2 Physicochemical properties and acid amount of three different-sized H-ZSM-5 catalysts

Sample	**Si/Al**[a)]	S_{BET}[b)] $m^2\ g^{-1}$	S_{EXT}[c)] $m^2\ g^{-1}$	**Acid amount**[d)] mmol g^{-1}	**Al content**[e)] mmol g^{-1}
H-ZSM-5 (S)	50	403	49	0.307	0.326
H-ZSM-5 (M)	53	399	32	0.286	0.309
H-ZSM-5 (L)	48	370	12	0.309	0.340

a) Si/Al: atomic ratio of Si/Al in the sample.

b) S_{BET}: BET surface area

c) S_{EXT}: External surface area

d) Acid amount: Estimated by the NH_3-TPD.

e) Al content: Content of Al in the sample.

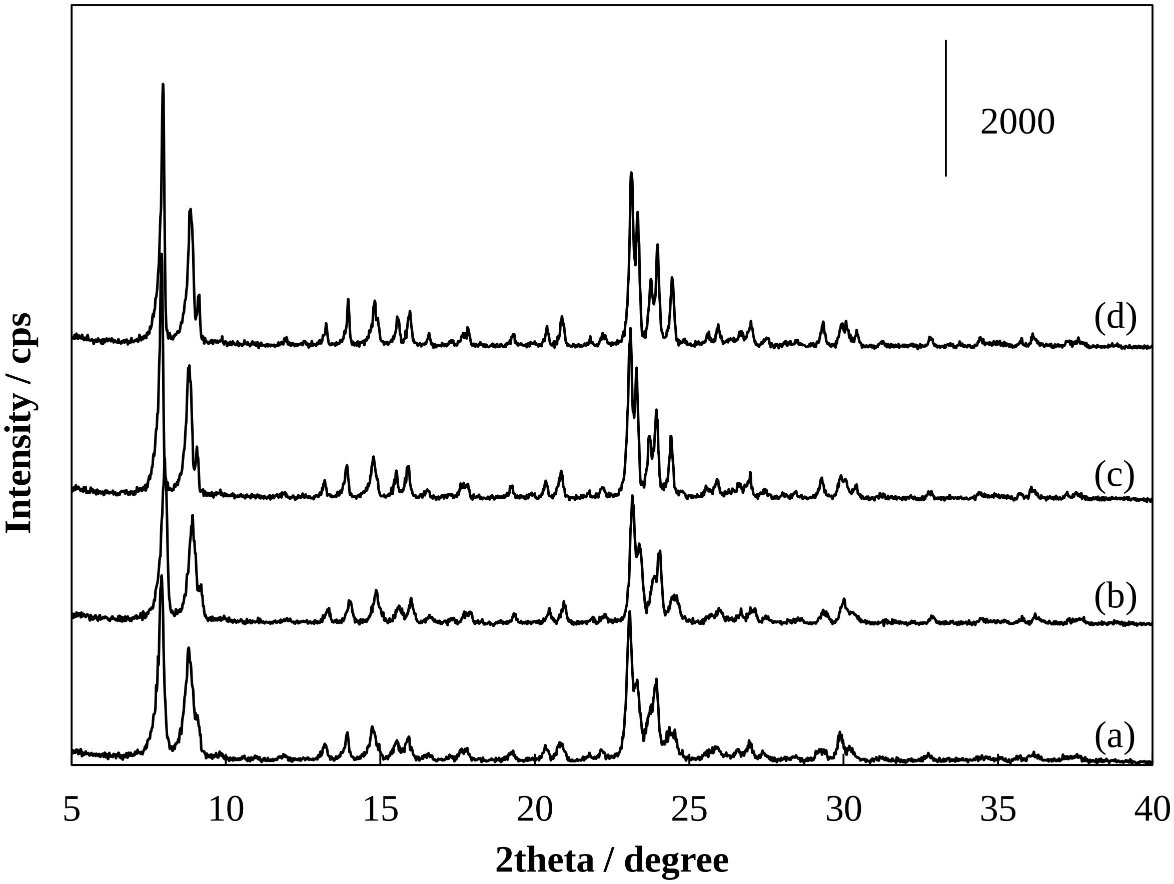

Figure 2.1

XRD patterns of the products synthesized with the molar ratio of the H_2O/Si in the gel = (a) 8.3, (b) 30, (c) 40 and (d) 100.

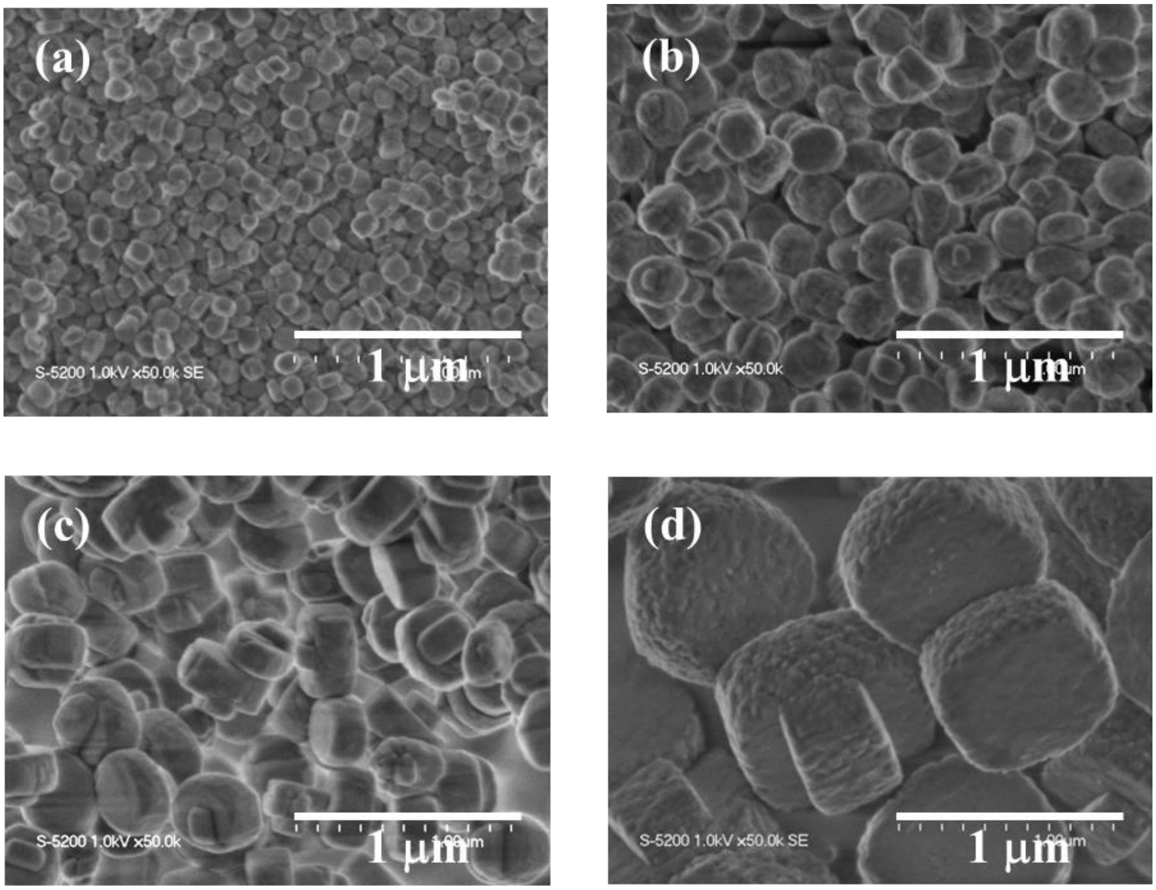

Figure 2.2

FE-SEM images of the products synthesized with the molar ratio of the H_2O/Si in the gel = (a) 8.3, (b) 30, (c) 40 and (d) 100.

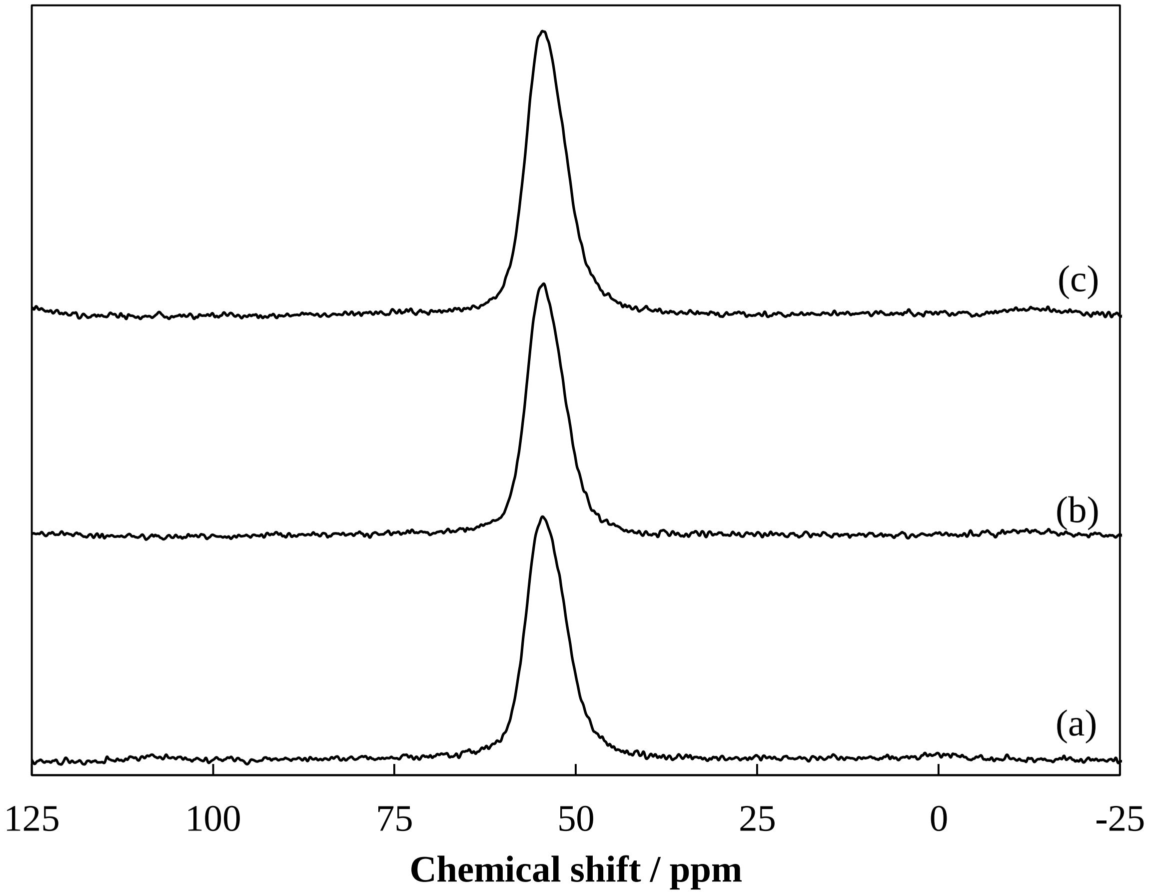

Figure 2.3

The ^{27}Al MAS NMR spectra of products synthesized with the molar ratio of the H_2O/Si in the gel = (a) 8.3, (b) 30 and (c) 100.

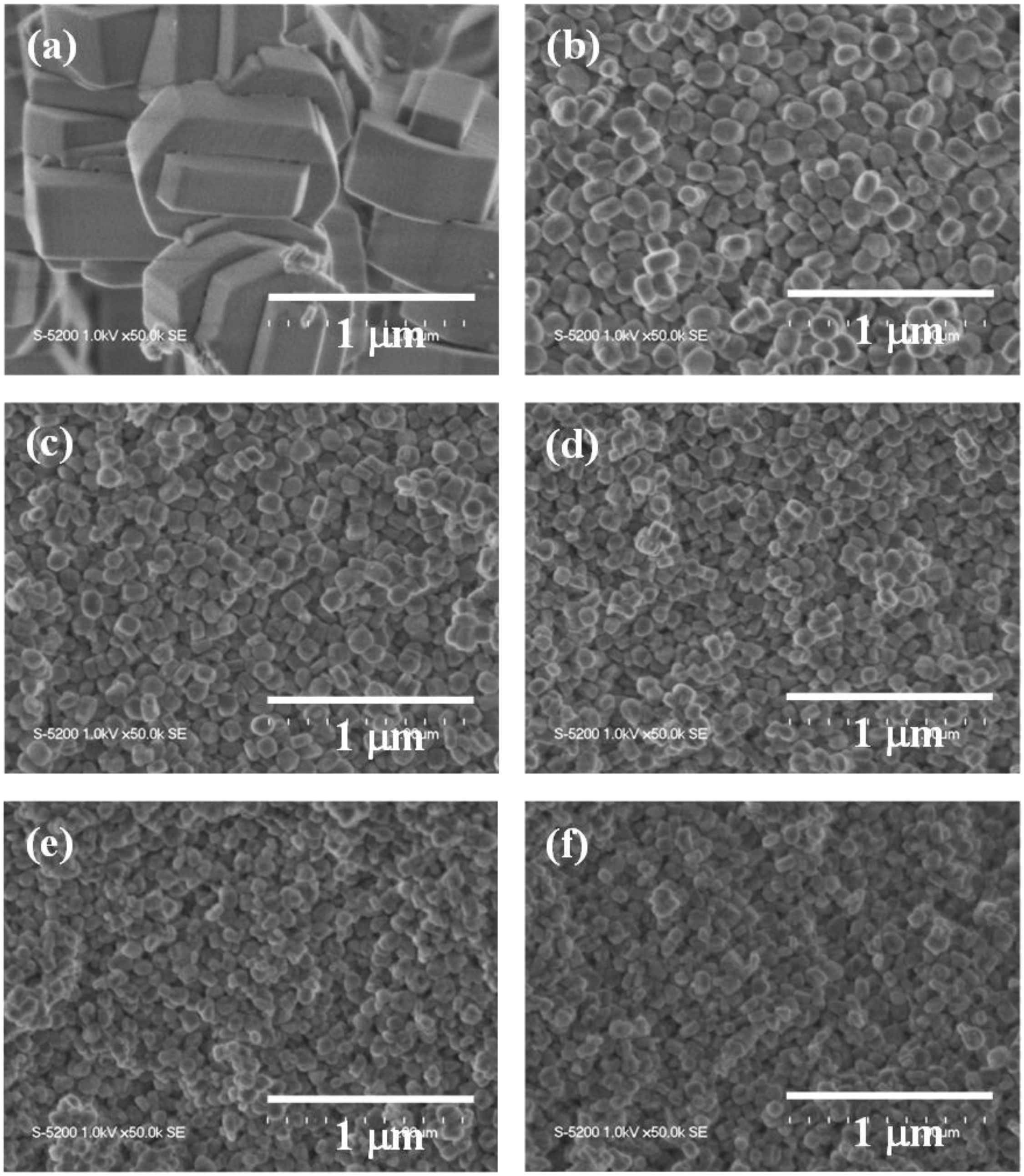

Figure 2.4

FE-SEM images of the products synthesized with the pre-aging time = (a) 0, (b) 12, (c) 24, (d) 48, (e) 72 and (f) 96 h.

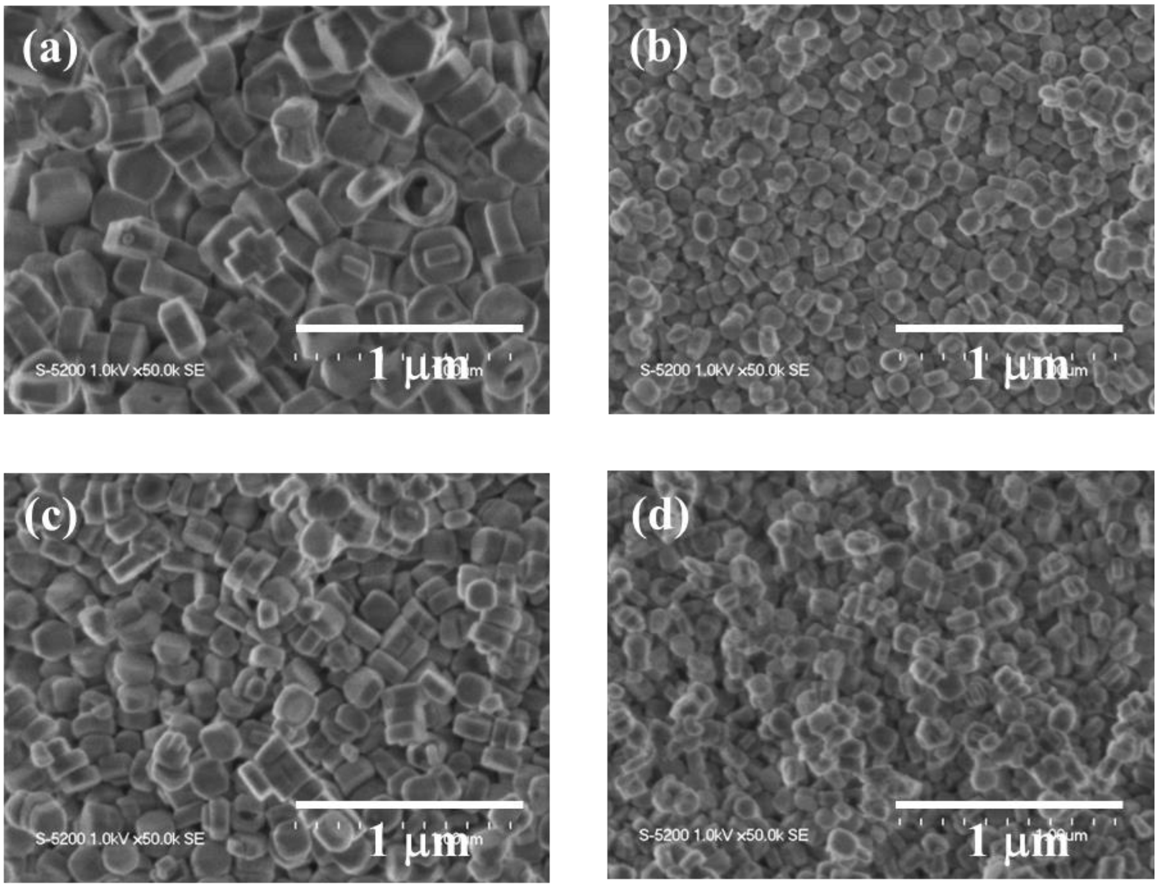

Figure 2.5

FE-SEM images of the products synthesized with the pre-aging temperature = (a) 298, (b) 333, (c) 353 and (d) 373 K

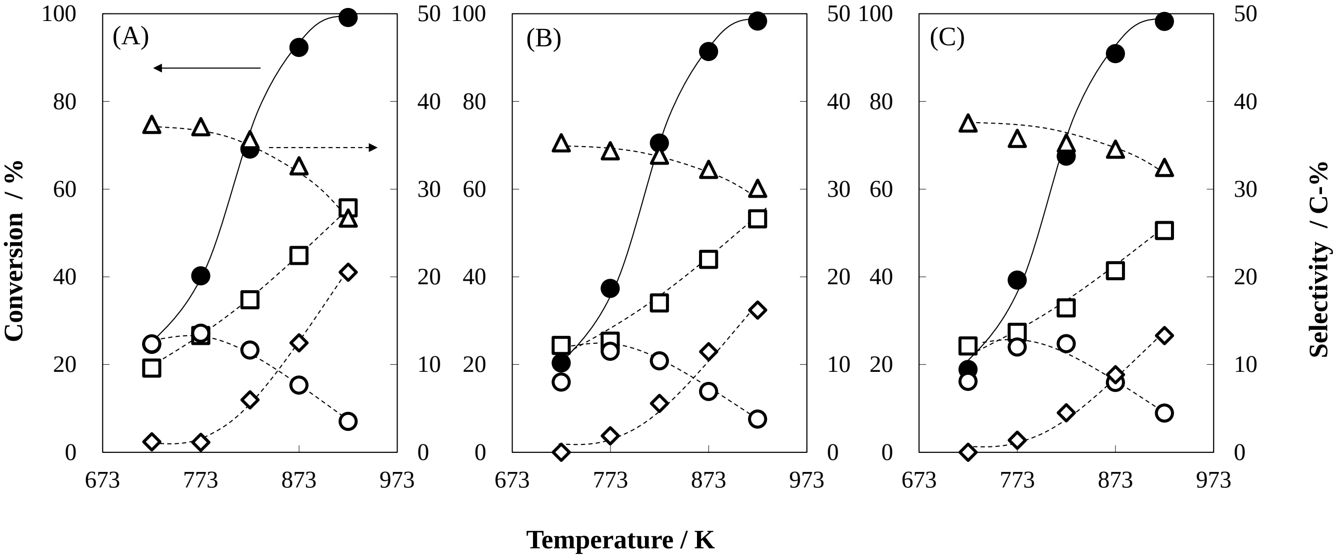

Figure 2.6

Results of cracking reaction of *n*-hexane over the three different-sized H-ZSM-5 catalysts with the reaction temperature varied ranging from 723 to 923 K. (A) S, (B) M and (C) L

Conversion (●), Propylene (△), Ethylene (□), Butenes (○), BTX (◇)

Reaction conditions:

0.05 g catalyst, W/F = 16 g-cat h / mol-*n*-hexane, Partial pressure of *n*-hexane = 6.0 kPa, 723-923 K.

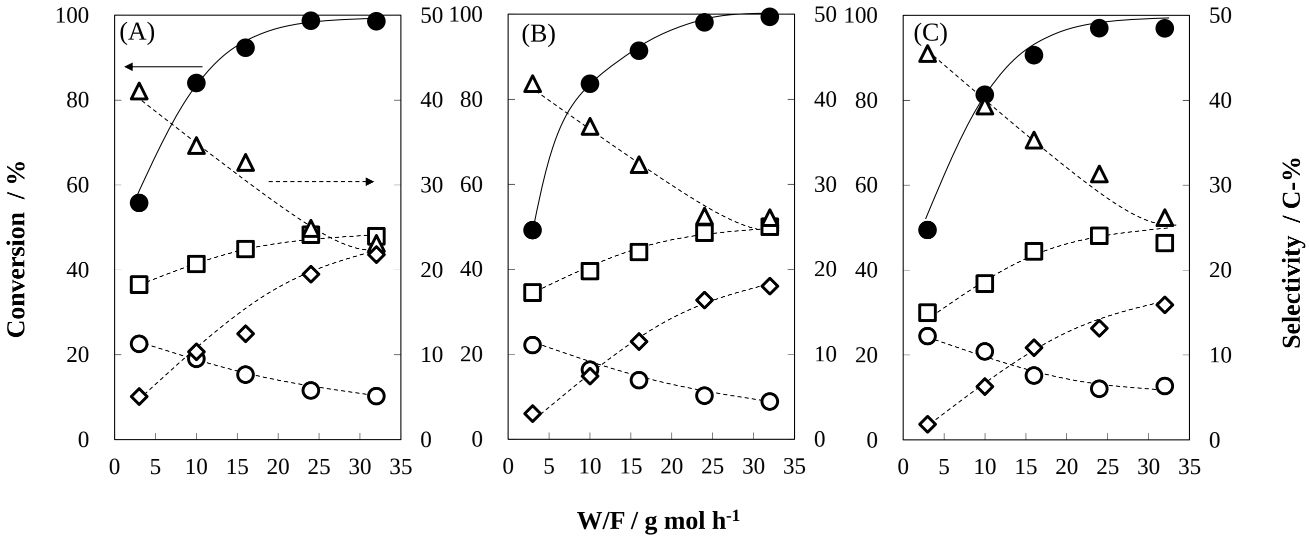

Figure 2.7

Results of cracking reaction of *n*-hexane over the three different-sized H-ZSM-5 catalysts with the various W/F. a) S, (b) M and (c) L

Conversion (●), Propylene (△), Ethylene (□), Butenes (○), BTX (◇)

Reaction conditions: 0.01-0.1 g catalyst, W/F = 2.5-32 g-cat h / mol-*n*-hexane, Partial pressure of *n*-hexane = 6.0 kPa, 873 K.

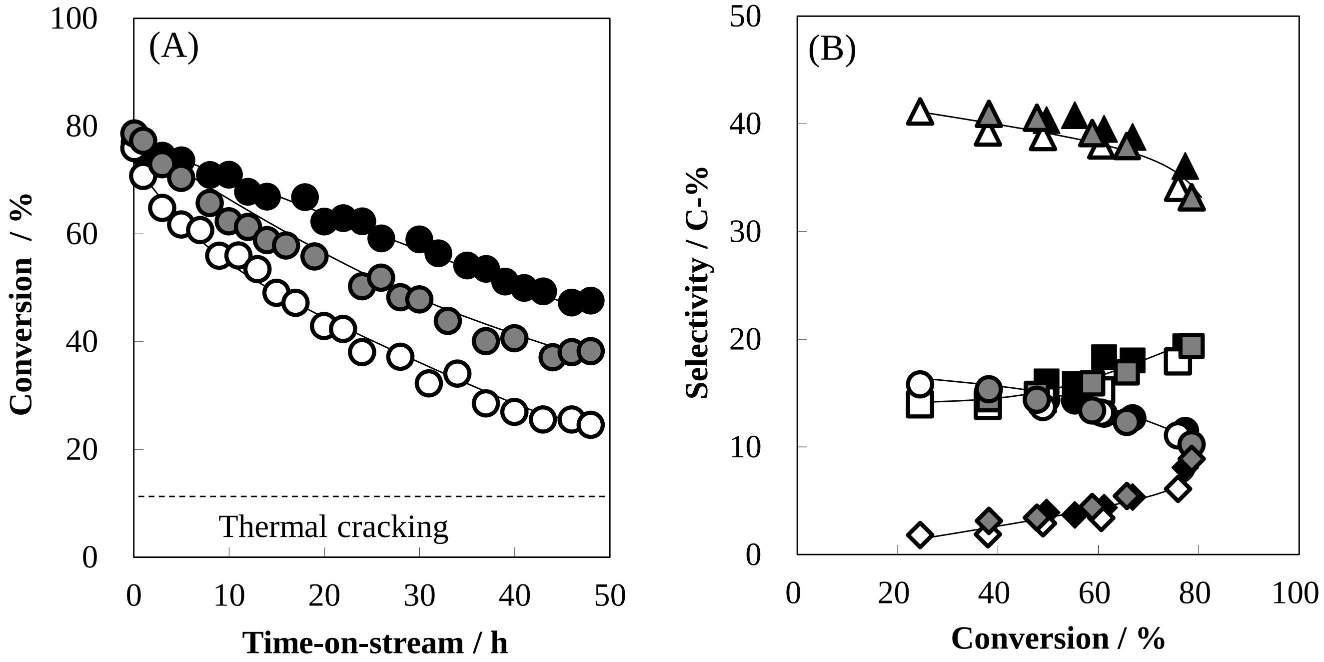

Figure 2.8

Results of cracking reaction of *n*-hexane over the three different-sized H-ZSM-5 catalysts .(A) Time on stream. S (Solid symbol), M (Gray symbol), L (Open symbol)

(B) Conversion vs Selectivity. Propylene (▲), Ethylene (■), Butenes (●). BTX (◆)

Reaction conditions: 0.01 g catalyst, W/F = 1 g-cat h / mol-*n*-hexane, Partial pressure of *n*-hexane = 23.0 kPa, 923 K.

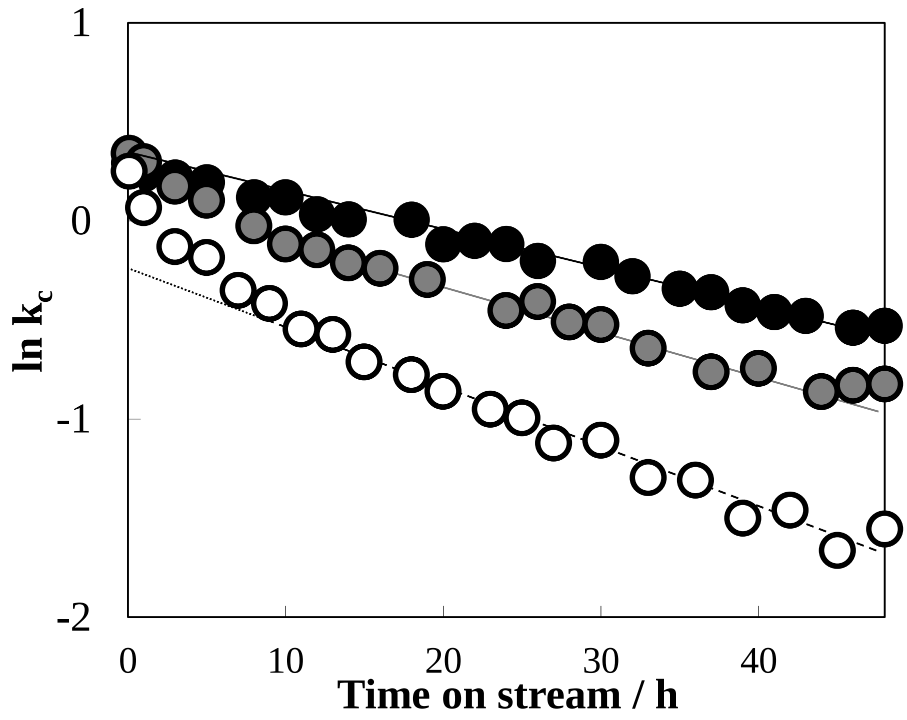

Figure 2.9

The change in lnk_c against *t*. S (Solid symbol), M (Gray symbol), L (Open symbol)

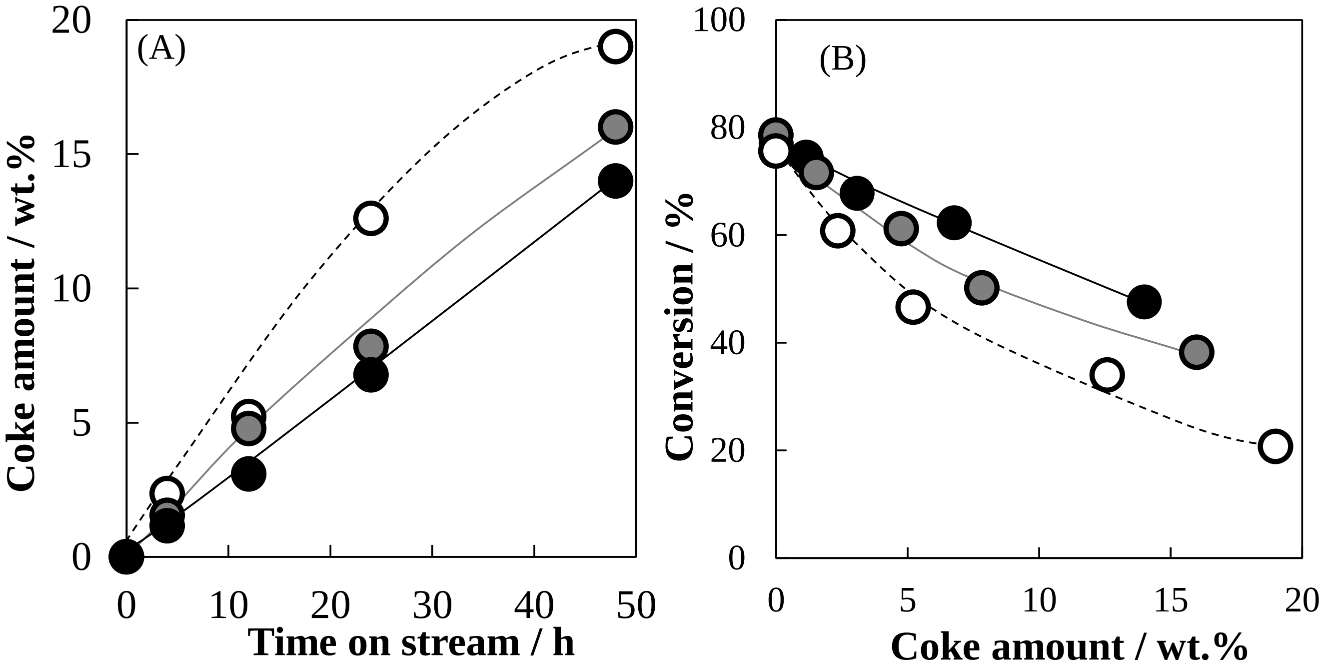

Figures 2.10

Effect of crystallite size on coke formation behavior: (A) The relationship between the reaction time and the amount of coke formed. (B)The relationship between the amount of coke and the conversion.

Chapter 3

Enlargement of external surface area of H-ZSM-5 zeolite by alkali treatment for *n*-hexane cracking

3-1 Abstract

The effects of external surface and acid properties of desilicated H-type ZSM-5 zeolites (H-ZSM-5) on their catalytic performance in *n*-hexane cracking were investigated. H-ZSM-5 with two different crystallite sizes of 100 nm and 1 μm were treated with NaOH solution of different concentrations. The external surface area (S_{EXT}) was increased with an increase in the NaOH concentration, because of the formation of mesopores inside the H-ZSM-5 crystallites as a result of desilication. The increase in the S_{EXT} of the H-ZSM-5 catalysts contributed to mitigating the catalyst deactivation during the *n*-hexane cracking. Although the amount of coke deposited on the alkali-treated H-ZSM-5 was larger than that on the parent H-ZSM-5, the micropore volume of the alkali-treated H-ZSM-5 decreased less due to coke deposition than that of the parent. The deactivation rate and the decrease in the micropore volume of the small-sized H-ZSM-5 catalysts were smaller than those of the large-sized catalysts, because of their shorter average diffusion path lengths. Thus the activity of the alkali-treated H-ZSM-5, especially small-sized one is less sensitive to coke deposition. Lewis acid sites (LASs) were generated by treating with NaOH of high concentrations. The selectivities to benzene, toluene and xylene (BTX) in the *n*-hexane cracking were increased with an increase in the LASs amount at high reaction temperatures (≥873 K). The LASs on the alkali-treated H-ZSM-5 were selectively removed by acid treatment. The resultant H-ZSM-5 exhibited a slightly lower *n*-hexane conversion and a lower selectivity to BTX but a small amount of coke compared to the parent and alkali-treated H-ZSM-5 catalysts, suggesting that LASs on alkali-treated H-ZSM-5 accelerated the dehydrogenation including hydride transfer and aromatization, forming BTX, which would be precursors of coke.

3-2 Introduction

In chapter 2, we have reported that reduction in the crystallite size of ZSM-5 is highly effective in improving the catalytic lifetime in the *n*-hexane cracking owing to large external surface area and short diffusion path lengths. Therefore, it is expected that the enlargement of external surfaces of H-ZSM-5 makes the catalyst life longer.

It has been reported that mesoporous zeolites can be prepared by various direct synthesis methods using carbon [1-3], organosilane surfactants [4] and cationic polymers [5]. Moreover, the desilication to form mesopores inside zeolite crystallites by the post treatment with NaOH solution have been reported [6, 7]. Ogura and co-workers. have reported that the NaOH treatment improves the conversion and activity per Al in the cumene cracking over alkali treated H-ZSM-5 [6]. They have claimed that alkali post-treatment does not lead to stronger acidity but leads to a greater degree of diffusivity inside the zeolite crystal, providing easier access to the microporous entrance via the mesopores created by the treatment. Groen and co-workers have reported a change in properties of ZSM-5 by the alkali treatment in detail [7]. They have examined the effect of treatment conditions such as the Si/Al ratio of zeolite, treatment time and temperature and claimed that the alkaline treatment selectively removes silicon atoms from the framework, leaving the catalytically important Al sites unaffected. On the other hand, some papers reported on the formation not only of mesopores but of LASs with NaOH treatment. Bjørgen and co-workers have reported that product distribution and lifetime in methanol to gasoline reaction (MTG) are altered dramatically with desilication of H-ZSM-5, as a result of formation of Lewis acid sites (LASs) [8]. There are only a few reports on the catalytic performance of alkali- treated H-ZSM-5 in paraffin cracking [9]. Therefore, the influence of LASs on the lifetime of H-ZSM-5 in paraffin cracking is still unclear.

In this chapter I have investigated the effects of alkali treatment of H-ZSM-5 zeolites on the external surface area (S_{EXT}) and acidic and catalytic properties. The alkali-treated ZSM-5 catalysts with different S_{EXT}s and Lewis acidities were prepared and examined to clarify the effect of their physicochemical properties on the activity, selectivity and lifetime in the cracking of *n*-hexane as a model compound of naphtha.

3-3 Experimental

3-3-1 Synthesis of different-sized ZSM-5 catalysts

Two H-ZSM-5 catalysts with a Si/Al ratio of ca. 50 and crystallite sizes of *ca*. 1 μm and 100 nm were synthesized according to our method [Chapter 2]. The gels with two different compositions of 1 SiO_2: 0.01 Al_2O_3: 0.25 TPAOH: 0.05 Na_2O: 8.3 or 100 H_2O were prepared from tetraethyl orthosilicate (TEOS, Tokyo Kasei, >96 %), tetrapropylammonium hydroxide (TPAOH, 25 % aqueous solution, Tokyo Kasei), $Al(NO_3)_3$•$9H_2O$ (Wako, 99.9 %) and NaOH (Wako, 97 %). Crystallization was carried out at 443 K for 24 h. The Na-type ZSM-5 (Na-ZSM-5) samples were obtained by calcination of the as-synthesized sample in an oven at 823 K to remove TPA cations. The calcined Na-ZSM-5 samples were treated with 1 M NH_4NO_3 (Wako, 99.0+%) aq. at 353 K for 3 h twice followed by calcination at 823 K for 10 h to exchange Na^+ ions for H^+. The lager and smaller sized H-ZSM-5 were denoted by “Parent L” and “Parent S”, resepectively.

3-3-2 Alkali treatment of ZSM-5 zeolite with NaOH solutions

An alkali treatment of the ZSM-5 zeolite was performed with aqueous solutions of 0.05, 0.1, and 0.2 M NaOH. To 100 ml of the NaOH aqueous solution was added 1 g of calcined Na-ZSM-5. The solution was stirred at 353 K for 1-5 h. In order to adjust the Si/Al atomic ratio to *ca*. 35, the treatment time was controlled; the time for the alkali treatment with 0.05, 0.1 and 0.2 M NaOH were 5, 3 and 1 h, respectively. The yields of alkali-treated samples were ca. 50 – 70 % (Table 3.1).

The alkali-treated zeolites were washed with deionized water to remove remaining NaOH. Then Na^+ ions in the Na-ZSM-5 were exchanged for H^+ by the conventional cation-exchange procedure described in section 3-3-1. The samples thus prepared were denoted by AT-, NaOH concentration and crystallite sizes (L or S), *e.g.* “AT-0.1L”.

3-3-3 Acid treatment of alkali-treated ZSM-5 zeolite using HNO_3 solutions

The acid treatment of the alkali-treated ZSM-5 zeolite was performed with 1.0 or 2.0 M HNO_3 (Wako) aqueous solution. To 100 ml of the HNO_3 aqueous solution was added 1 g of the large-sized Na-ZSM-5 treated with 0.2 M NaOH to provide Na type AT-0.2L. The solution was stirred at 353 K for 2 h. After washed with deionized water followed by drying at 383K overnight, the sample was calcined. Thus obtained products were denoted by AAT- 1L and AAT-2L, respectively.

3-3-4 Characterizations

XRD patterns were collected on a Rint-Ultima III (Rigaku) using a Cu Kα X-ray source (40 kV, 20 mA). Nitrogen adsorption measurements to determine the BET surface area (S_{BET}), S_{EXT} , and micropore volume (V_{micro}) were conducted at 77 K on a Belsorp-mini II (Bel Japan). S_{EXT} and V_{micro} were estimated by the *t*-plot method. Field-emission scanning electron microscopic (FE-SEM) images of the powder samples were obtained on an S-5200 microscope (Hitachi) operating at 1-30 kV. The sample was mounted on a carbon-coated microgrid (Okenshoji Co.) without any metal coating. Transmission electron microscopic (TEM) images of the powder samples were obtained on a JEM-1400 microscope (JOEL) operating at 100 kV. Si/Al ratios of the samples were determined by using an inductively coupled plasma-atomic emission spectrometer (ICP-AES, Shimadzu ICPE-9000). To investigate the Al environment, solid-state ^{27}Al magic-angle spinning (MAS) NMR spectra were obtained on a JEOL ECA-600 spectrometer (14.1 T). The relaxation delay time was 10 ms. The ^{27}Al chemical shift was referenced to $AlNH_4(SO_4)_2 \cdot 12H_2O$ at -0.54 ppm and samples were spun at 17 kHz by using a 4 mm ZrO_2 rotor.

Temperature-programmed ammonia desorption (NH_3-TPD) profiles were recorded on a Multitrack TPD equipment (Japan BEL). Typically, 25 mg catalyst was pretreated at 773 K in He (50 mL min^{-1}) for 1 h and then cooled to 423 K. Prior to the adsorption of NH_3, the sample was evacuated at 423 K for 1 h. Approximately 2500 Pa of NH_3 was allowed to make contact with the sample at 423 K for 10 min. Subsequently, the sample was evacuated to remove weakly adsorbed NH_3 at the same temperature for 30 min. Finally, the sample was heated from 423 to 873 K at a ramping rate of 10 K min^{-1} in a He flow (50 mL min^{-1}). A mass spectrometer was used to monitor desorbed NH_3 ($m/e = 16$). The amount of acid sites was determined by using the area in the profiles.

Fourier transform infrared (FT-IR) spectra were obtained at a resolution of 4 cm^{-1} using a Jasco 4100 FTIR spectrometer equipped with a mercury cadmium telluride (MCT) detector. A total of 64 scans were averaged for each spectrum. IR spectra of the clean disk were recorded in vacuo at 423 K to obtain background spectra. The H-ZSM-5 sample was pressed into a self-supporting disk (20 mm diameter, 50 mg) and placed in an IR cell attached to a conventional closed-gas circulation system. The sample was pretreated by evacuation at 773 K, followed by adsorption of 30 Torr pyridine at 623 K. Then, the sample was evacuated at the same temperature for 30 min. The spectra were recorded at 423 K. Background-subtracted IR spectra corresponding to adsorbed species were presented throughout this chapter.

3-3-5 Catalytic cracking of 1, 3, 5-triisopropylbenzene

The cracking of 1, 3, 5-triisopropylbenzene (TIPB, Tokyo Kasei, 95.0%) was carried out in a 6-mm quartz tubular flow microreactor loaded with 10 mg of 50/80 mesh zeolite pellets without a binder. The catalyst was centered at the reactor in a furnace. The catalyst was calcined at 773 K for 1 h prior to the reaction. Then the reactor was cooled to the reaction temperature (573 K). The initial partial pressure of TIPB was set at 0.5 kPa. Helium was used as a carrier gas. The ratio of the catalyst weight to the flow rate (W/F_{TIPB}) was 154 g-cat h/mol-TIPB. The reaction products were analyzed with an on-line gas chromatograph (Shimadzu GC-2014) with an FID detector.

3-3-6 Catalytic cracking of *n*-hexane

The cracking of *n*-hexane (Wako, 96.0+%) was carried out in a 6-mm quartz tubular flow microreactor loaded with 10 to 100 mg of 50/80 mesh zeolite pellets without a binder. The catalyst was centered at the reactor in a furnace. The catalyst was calcined at 923 K for 1 h prior to the reaction, and then cooled to the reaction temperature ranging from 723 to 923 K. The initial partial pressure of *n*-hexane was set at 6 or 23 kPa. Helium was used as a carrier gas. The $W/F_{n\text{-hexane}}$ and the weight hourly space velocity of *n*-hexane (WHSV) were varied from 2.5 to 32 g-cat h/mol-*n*-hexane and 2.7 to 70 h^{-1}, respectively. The reaction products were analyzed with an on-line gas chromatograph (Shimadzu GC-2014) with an FID detector and a capillary column (PLOT fused silica 30 m×0.53 mm, 6 μm film thickness). Selectivities were calculated based on the carbon numbers.

The amount of coke formed during the reaction was determined from the weight loss from 673 to 1073 K in a thermogravimetric (TG) profile, which was performed on a thermogravimetric - differential thermal analyser (TG-DTA, Rigaku Thermo plus EVO II)

3-4 Results and discussion

3-4-1 Physicochemical properties of alkali- and alkali-acid-treated H-ZSM-5

SEM observation indicated that Parent L and Parent S exhibited uniform crystallite size distributions of 1 μm and 100 nm, respectively. The acid amounts of Parent L and Parent S were almost the same; it was estimated at 0.288 and 0.291 mmol/g, respectively, from NH_3-TPD. The external surface area of Parent L was much smaller than that of Parent S (Table 3.1).

Figure 3.1 (A) shows XRD patterns of the alkali-treated H-ZSM-5 zeolites. Although the intensities of the peaks attributed to the **MFI** zeolite were slightly decreased with an increase in the NaOH concentration, the characteristic diffraction peaks still remained even for AT-0.2.

Figure 3.2 shows the N_2 adsorption and desorption isotherms for the parent and alkali-treated H-ZSM-5 catalysts. Parent L exhibited a typical isotherm of microporous materials with a plateau at high relative pressures (type I, IUPAC). Parent S exhibited a type I isotherm with a steep increase in adsorption volume at P/P_0 = 0.8-0.9. This steep increase is due to the interparticle voids of the nanocrystals of Parent S. The N_2 isotherms for the alkali-treated samples changed obviously from type I to combined types I and IV with hysteresis, which corresponded to the formation of mesopores in zeolite crysatallites, regardless of its crystal size. The S_{BET} and S_{EXT} increased with an increase in the NaOH concentration (Table 3.1). However, V_{micro} was decreased with an increase in the NaOH concentration. From these results, it is apparent that a higher concentration of NaOH causes the formation of more mesopores, but the zeolitic structure collapses slightly more severely. The alkali-acid-treated samples show almost the same XRD patterns and S_{BET} and S_{EXT} values as AT-0.2L (Fig. 3.1 (b)), regardless of the HNO_3 concentration (Table 3.1).

The morphology of the parent and alkali-treated H-ZSM-5 zeolites was evaluated by FE-SEM and TEM observations (Fig. 3.3). The SEM images showed that there was no difference in crystallite shape between Parent L and AT-0.05L, while a part of crystallites of AT-0.2L were broken into pieces. TEM images revealed changes in the inner part of crystallite due to desilication. The inside densities of AT-0.05L and AT-0.2L crystallites were lower than those of the outer fringes of crystallites. The width of the outer fringes decreased along with the NaOH concentration. Taking into consideration the results of N_2 adsorption and desorption measurements, the decreased density of crystallites should be due to the formation of meso- and macro-pores in the crystallites by the desilication.

3-4-2 Acid properties of alkali- and alkali-acid-treated H-ZSM-5

The acidity of the alkali-treated H-ZSM-5 samples was examined by NH_3-TPD and pyridine-FTIR. Figure 3.4 shows the NH_3-TPD profiles of Parent L and alkali- and alkali-acid-treated samples. A conventional NH_3-TPD profile of H-ZSM-5 has two NH_3 desorption peaks. The low temperature peak (400–600 K) corresponds to NH_3 adsorbed on non-acidic -OH groups and NH_4^+, which forms by the reaction of NH_3 and Bronsted acid sites (BASs), and does not correspond to NH_3 adsorbed on catalytically active BASs and LASs. On the other hand, the high temperature peak (600–800 K) corresponds to NH_3 desorption from catalytically active BASs and LASs [10, 11]. We obtained NH_3-TPD profiles after removal not only of physisorbed NH_3 but also of NH_3 adsorbed on non-acidic -OH groups and NH_4^+ by evacuation at 423 K. Therefore the profiles have no low temperature peak.

The NH_3-TPD profiles for L series are shown in Fig. 3.4 (A). The peak intensity for AT-0.05L was higher than that for Parent L, since the Si/Al ratio was decreased by desilication. However, when Parent L was desilicated with 0.1 or 0.2 M NaOH, the peak intensity was decreased with an increase in the NaOH concentration, and the shoulder peak appeared at around 500 K. The NH_3-TPD profiles for S series were similar to those for L series. The amounts of acid sites for L and S series estimated by the peak areas in NH_3-TPD profiles are listed in Table 3.1. The change in the amounts of acid sites suggests that the desilication takes place selectively at a low NaOH concentration and that both desilication and dealumination of framework Al to extra-framework Al take place at high NaOH concentrations. The shoulder peak at around 500 K may correspond to a part of extra-framework Al which exhibits weak Lewis acidity.

The alkali-treated samples were further treated with HNO_3. The shoulder peak at around 500 K for AT-0.2L was decreased with an increase in the HNO_3 concentration and almost disappeared after the acid treatment with 2 M HNO_3 (Fig. 3.4 (B)). It has been reported that the tetrahedrally coordinated Al in the framework of ZSM-5 are hardly dealuminated by the acid treatment under mild conditions [12]. Therefore, the decreased acid amount of AAT series (Table 3.1) would be due to the removal of extra-framework Al species, a part of which exhibits Lewis acidity. These results imply that the change in the NH_3-TPD profile by the alkali treatment with 0.1 and 0.2 M NaOH solutions is caused by the formation of extra-framework Al species from the tetrahedrally coordinated Al in the framework.

In order to clarify the change in the acid properties, FT-IR spectra of adsorbed pyridine and ^{27}Al MAS NMR spectra were measured for L and ATT series. Figure 3.5 shows FT-IR spectra of adsorbed pyridine for L series. Bands at around 1450 and 1540 cm^{-1} are attributed to LASs and BASs, respectively [13]. Table 3.2 shows the amount of BASs and LASs calculated from two bands corresponding to BASs and LASs [14]. The amount of BASs was increased due to desilication by alkai treatment with 0.05M NaOH solution, regardless of crystallite sizes. However, the amount of BASs in alkali-treated samples was decreased with an increase in the NaOH concentration, while that of LASs was increased with an increase in the NaOH concentration in the alkali treatment. In contrast, the amount of LASs in AT-0.2L was decreased with an increase in the HNO_3 concentration, while that of BASs was not decreased in the subsequent acid treatment. Therefore, it is apparent that LASs are generated by the alkali treatment and removed by the subsequent acid treatment without a decrease in the amount of BASs.

Figure 3.6 shows ^{27}Al MAS NMR spectra for L series. The NMR spectra of Parent L and AT-0.05L exhibited a sharp high peak at 58 ppm and a very small peak at 0 ppm, which are assigned to tetrahedrally coordinated Al in the framework and octahedrally coordinated Al in the extra-framework, respectively. These findings indicate that little dealumination occurred during the alkali treatment with such a low concentration of NaOH solution. On the other hand, for AT-0.1L and AT-0.2L, dealumination remarkably occurred during the alkali treatment. A large part of extra-framework Al species were removed by the acid treatment (Fig. 3.6 (B)). It is estimated that at least a part of the extra-framework Al species exhibits the Lewis acidity from FT-IR observation and ^{27}Al MAS NMR spectra. These findings indicate that the shoulder peak at around 500 K in the NH_3-TPD profile for the samples treated with 0.1 and 0.2 M NaOH is due to the generation of LASs by the dealumination and that the extra-framework Al species, a part of which exhibits Lewis acidity, are removed by the acid treatment.

3-4-3 Cracking of 1,3,5-triisopropylbenzene over alkali- and alkali-acid treated H-ZSM-5 catalysts

TIPB is too large to enter the pores of ZSM-5 zeolite and, therefore, the catalytic activity for TIPB cracking reflects the Bronsted acidity solely on the external surfaces of H-ZSM-5 [15]. In order to elucidate the catalytic activity of external surfaces of the alkali-treated H-ZSM-5 catalysts, the catalytic cracking of TIPB was carried out.

Fig. 3.7 shows the relationship between the first order rate constant, k_{TIPB}, and S_{EXT} of H-ZSM-5 catalysts. The proportional relationship was observed except for Parent L and Parent S, irrespective of the NaOH concentration in the alkali treatment and HNO_3 concentration in the acid treatment. Activities per a unit of external surface area, k_{TIPB}/S_{EXT}, for the alkali-treated H-ZSM-5 were higher than those for Parent L and Parent S. It is suggested that BASs on the external surfaces of H-ZSM-5 are enriched by the desilication. The LASs on the alkali-treated H-ZSM-5 were removed by the acid treatment with HNO_3. It is conceivable that the LASs both on the external and internal surfaces were removed by this treatment. However, the acid treatment did not affect the k_{TIPB}/S_{EXT} value, suggesting that the catalytic cracking of TIPB was independent of LASs. Actually, γ-alumina (Nippon Aerosil Co.), which has no BASs [16], exhibited no catalytic activity for TIPB cracking. Thus the Bronsted acid density on the external surface is almost constant, irrespective of the crystallite size and the NaOH concentration in the alkali treatment.

3-4-4 Catalytic cracking of *n*-hexane over alkali- and alkali-acid-treated H-ZSM-5 catalysts

The catalytic cracking of *n*-hexane was carried out over L series, S series, and ATT series. First, the influence of the reaction temperature on the catalytic performances was examined. Fig. 3.8 (A) shows the results of *n*-hexane cracking over L series with different S_{EXT} values at 723 - 923 K. It should be noted that even without catalyst the thermal cracking of *n*-hexane proceeded. The conversions for the thermal cracking of *n*-hexane were 0, 2.6 and 7.2 %, at 723, 823 and 923 K, respectively. The conversion of *n*-hexane for the catalytic cracking was increased along with the reaction temperature for every catalyst. AT-0.05L exhibited the highest conversion irrespective of temperature. We have reported that the catalytic cracking of *n*-hexane over H-ZSM-5 is not limited by diffusion of *n*-hexane under the present reaction conditions [Chapter 2]. Therefore, the highest conversion for AT-0.05L is caused not by the formation of mesopores but by the increase in BASs. AT-0.1L and AT-0.2L exhibited lower conversions than Parent L in a low temperature region (<823 K). The order of the conversions in the low temperature region for Parent L and alkali-treated H-ZSM-5 will be almost the same as that of the amount of BASs estimated not from peak areas but from peak intensities in the NH_3-TPD profiles shown in Fig. 3.5. The peak intensity could roughly correspond to the amount of BASs, while the peak area corresponds to the total amount of both BASs and LASs. These findings indicate that *n*-hexane cracking occur solely on BASs in the low temperature region. On the other hand, the samples treated with NaOH solution of high concentrations exhibited higher conversions than Parent L in a high temperature region (≥873 K).

The conversions for AAT-1L and AAT-2L were similar to that for AT-0.2L in the low temperature region (Fig. 3.8 (B)), because their Bronsted acidities were similar to that of AT-0.2L. On the other hand, the conversions for AAT series in the high temperature region were decreased with a decrease in the amount of LASs. These findings indicate that not only BASs but also LASs accelerate the *n*-hexane cracking in the high temperature region.

Second, the change in the product distribution effected by the conversion was examined at 873 K (Fig. 3.9), where the thermal cracking of *n*-hexane proceeded very slowly. To keep contribution from the thermal cracking constant, the conversion was controlled with the catalyst weight varied. The selectivities to propylene and butenes were decreased, while those to ethylene and BTX were increased with an increase in *n*-hexane conversion for every catalyst. These findings indicate that BTX forms by a successive reaction of propylene and butenes. Ethylene should form *via* energetically unfavorable primary carbenium ions, regardless of the reaction mechanism (monomolecular or bimolecular mechanism [17]) and, therefore, the apparent activation energy for ethylene formation should be high.

At a high temperature of 873 K, the primary carbenium ions should form relatively readily. Therefore, ethylene forms not only by cracking of *n*-hexane but also by successive reactions of hydrocarbons with a carbon number of 4 or more, resulting in the increase in ethylene selectivity along with the conversion. At a low conversion as around 60 %, Parent L, AT-0.05L and AAT-2L exhibited a similar product distribution, regardless of S_{EXT}. However, the selectivities to propylene and C1-C4 paraffins were low, while those to ethane and BTX were high for AT-0.1L and AT-0.2L, compared to Parent L, AT-0.05L and AAT-2L with little Lewis acidity. These findings suggest that LASs may play an important role in dehydrogenation reactions to form a part of ethylene and BTX.

To clarify the effect of LASs on *n*-hexane conversion at high temperatures, H-ZSM-5 (Si/Al = 500) having little LASs and γ-alumina having no BASs were used as catalysts at 923 K. Figure 3.10 shows the relationship between product yields and *n*-hexane conversion. A considerable amount of light olefins and paraffins formed and BTX scarcely formed on H-ZSM-5, while BTX, especially benzene, was the main products on γ-alumina at a conversion higher than 20 %. These findings indicate that LASs accelerated the dehydrogenation including hydride transfer, resulting in the high yield of BTX. It is apparent that LASs act as a catalyst for *n*-hexane conversion at high temperatures and the reaction mechanism on LASs is quite different from that on BASs.

3-4-5 Effect of external surface area and crystallite size on deactivation

The change in *n*-hexane conversion along with time-on-stream (TOS) was examined under a higher initial pressure of *n*-hexane of 23 kPa, which should lead to faster deactivation. The conversion of *n*-hexane by thermal cracking was 10.2 % under these reaction conditions. The initial conversion of *n*-hexane on every alkali treated sample was almost the same (ca. 90 %) as shown in Fig. 3.11 (A). In order to attain almost the same initial conversion, the amount of Parent L and S used were 1.6 times as much as those of the alkali treated samples. The conversion was decreased along with TOS.

The catalytic cracking of *n*-hexane obeys the first-order kinetics. Assuming that the deactivation rate is in proportion to the first order rate constant, the deactivation rate is expressed as follows:

$$-dk_c / dt = k_d k_c \qquad (1)$$

$$k_d t = \ln k_{c0} - \ln k_c \qquad (2)$$

where k_c is the rate constant for catalytic cracking, k_d is the rate constant for deactivation, t is TOS, and k_{c0} is k_c at $t = 0$ [chapter 2]. In Fig. 3.11 (B), ln k_c is plotted against t. The linear relationships are observed irrespective of S_{EXT}. The k_d values, which are estimated by the equation (2) and Fig. 3.11 (B), are plotted against S_{EXT} as shown in Fig. 3.12 (A). It is apparent that the larger S_{EXT} of H-ZSM-5 contributes to the slower deactivation for each crystallite size. However, despite the fact that the S_{EXT} of AT-0.2 M L was much larger than that of Parent S, the deactivate rate for AT-0.2L was similar to that for Parent S.

The relationship between S_{EXT} and the amount of coke formed for 24 h is shown in Fig. 3.12 (B). The amount of coke was estimated by TG-DTA analyses. The amount of coke formed on Parent S was much less than that on Parent L, as reported in chapter 2. In Parent S, the products involving coke precursors may easily diffuse out from the pores, because of shorter diffusion path length and larger S_{EXT} than Parent L. Therefore, coke formation is reduced, resulting in the slow deactivation. In contrast, as for the alkali treated samples, the coke amount increased with an increase in S_{EXT} for each crystallite size. It is because LASs promote the coke formation owing to their dehydrogenation activity. However, despite the larger amount of coke formed on the alkali-treated samples, the deactivation rate was decreased with an increase in S_{EXT}, probably because the larger number of pore entrances mitigated the deactivation due to pore blocking.

Figure 3.13 shows the relationship between %-decrease in V_{micro} by coke formed for 24 h and and S_{EXT}. The %-decrease in V_{micro} was defined as follows:

$$\{1 - (V_{micro} \text{ of the used catalyst})/(V_{micro} \text{ of the fresh catalyst})\} \times 100. \qquad (3)$$

The %-decrease in V_{micro} was decreased with a decrease in crystallite size and an increase in S_{EXT}. Kim and co-workers have reported that the higher mesoporosity of ZSM-5 provides the longer catalytic lifetime for methanol conversion, because of the larger external surface area and the shorter diffusion path length [18]. There are two possible reasons to explain the deactivation behavior. First, the increase in S_{EXT} corresponds to the increase in the number of the pore entrances. The larger number of pore entrances give the more active sites available for the *n*-hexane cracking at the same number of pore blockings by coke. Second, the enlargement of S_{EXT} and/or the reduction of crystallite size shorten the diffusion path length. Coke precursors, BTX etc., formed inside the shorter micropores are more easily diffused out of the micropores and, therefore, the coke formation in the micropores is more effectively prevented.

The diffusion path lengths in H-ZSM-5 were shortened on average by the alkali treatment. However, the distribution of the path lengths may be wide, because the desilication takes place randomly. Furthermore, LASs will accelerate coke formation. Therefore, the deactivation rate for AT-0.2L with a higher S_{EXT} is almost the same as that for Parent S with a lower S_{EXT}. Thus the small-sized and alkali-treated H-ZSM-5 catalysts exhibit the highest resistance to catalyst deactivation by coke formation.

3-4-6 Effect of Lewis acid sites on deactivation rate

The diffusion path lengths of alkali-treated samples should be shorter than those of parent samples. On the other hand, the coke amount increased with an increase in S_{EXT} for each crystallite size. This finding may be due to the dehydrogenation activity of LASs. In order to clarify the influence of LASs on coke formation and deactivation, the effect of the acid treatment were examined. The acid treatment removes only LASs as mentioned in Section 3-4-3. The *n*-hexane cracking over Parent L, AT-0.2L and AAT series was performed. The initial conversion slightly decreased by the acid treatment, because the catalytically active LASs on the alkali-treated H-ZSM-5 were removed by the acid treatment. The initial conversions for AT-0.2L, AAT-1L and AAT-2L were 88, 82 and 76 %, respectively. Figure 3.14 shows the coke amount formed for 24 h and the deactivation rate constant, $k_{d.}$, for Parent L and alkali- and alkali-acid treated samples. The deactivation rates were decreased from 0.019 to 0.014 by the acid treatment with 2 M HNO_3. The largest amount of coke was formed on AT-0.2L, because AT-0.2L had a lot of LASs, which accelerate the coke formation. LASs on AT-0.2L were removed by the acid treatment, resulting in a less amount of coke and less deactivation. Thus LASs on H-ZSM-5 play the negative role in the *n*-hexane cracking.

3-5 Conclusions

The catalytic performance of alkali- and alkali-acid treated H-ZSM-5 in the *n*-hexane cracking has been studied. S_{EXT} and LASs were increased with an increase in the NaOH concentration. The deactivation rate was decreased with an increase in S_{EXT}. The deactivation rate of large-sized H-ZSM-5 catalyst treated with 0.2 M NaOH is less than half of the parent H-ZSM-5 catalyst. The larger number of pore entrances and shorter diffusion path lengths should retard the deactivation due to blocking by coke formed during the reaction. The small-sized H-ZSM-5 catalysts are more stable against coke deposition than the large-sized catalysts, because of their shorter average diffusion path lengths.

The external surface hardly affects the selectivity in *n*-hexane cracking. However, LASs enhance dehydrogenation and aromatization at high temperature (≥873 K), resulting in the formation of large amount of aromatic compounds and coke. The LASs on the alkali treated H-ZSM-5 can be removed by the acid treatment. The conversion for the alkali-acid treated H-ZSM-5 is slightly low compared with the parent alkali-treated H-ZSM-5. However, it exhibits the higher selectivity to propylene and a less amount of coke formed during *n*-hexane cracking. Therefore, the alkali-acid treatment of H-ZSM-5 is an effective and simple post-treatment method, leading to a high propylene yield and a long lifetime.

References

1. C. J. H. Jacobsen, C. Madsen, J. Houzvicka, I. Schmidt, A. Carlsson, J. Am. Chem. Soc., 122 (2000) 7116.
2. Y. Tao, H. Kanoh, K. Kaneko, J. Am. Chem. Soc., 125 (2003) 6044.
3. A. H. Janssen, I. Schmidt, C. J. H. Jacobsen, A. J. Koster, K. P. de Jong, Micropor. Mesopor. Mater. 65 (2003) 59.
4. V. N. Shetti, J. Kim, R. Srivastava, M. Choi, R. Ryoo, J. Catal. 254 (2008) 296.
5. F. -S. Xiao, L. Wang, C. Yin, K. Lin, Y. Di, R. Xu, D. S. Su, R. Schlögl, T. Yokoi, T. Tatsumi, Angew. Chem. 118 (2006) 3190.
6. M. Ogura, S. Shinomiya, J. Tateno, Y. Nara, M. Nomura, E. Kikuchi, M. Matsukata, Appl. Catal. A: Gen. 219 (2001) 33.
7. J. C. Groen, J. A. Moulijn, J. Pérez-Ramírez, J. Mater. Chem. 16 (2006) 2121.
8. M. Bjørgen, F. Joensen, M. S. Holm, U. Olsbye, K. -P. Lillerud, S. Svelle, Appl. Catal. A: Gen. 345 (2008) 43.
9. J. S. Jung, J. W. Park, G. Seo, Appl. Catal. A: Gen. 288 (2005) 149.
10. M. Niwa and K. Katada, Catal. Surv. Jpn. 1 (1997) 215
11. K. Suzukia, Y. Aoyagia, N. Katadaa, M. Choib, R. Ryoob, M. Niwa, Catal. Today 132 (2008) 38.
12. C. S. Triantafillidis, A. G. Vlessidis, L. Nalbandian, N. P. Evmiridis, Micropor. Mesopor. Mater. 47 (2001) 369.
13. E. P. Parry, J. Catal. 2 (1963) 371.
14. C. A. Emeis, J. Catal. 141 (1993) 347.
15. S. Namba, A. Inaka and T. Yashima, Zeolites 6 (1986) 107.
16. T. R. Hughes, H. M. White, R. J. White, J. Catal. 13 (1969) 58.
17. A. Corma, A.V. Orchillés, Micropor. Mesopor. Mater. 35 (2000) 21.
18. J. Kim, M. Choi, R. Ryoo, J. Catal. 269 (2010) 219.

Table 3.1 Physicochemical properties and acid amount of parent, alkali-treated and alkali-acid-treated H-ZSM-5 catalysts

Catalyst	**Treatment time**		**Recovery yields**	**Si/Al**[a)]	S_{BET} [b)]	S_{EXT} [c)]	V_{micro} [d)]	**Acid amount**[e)]
	NaOH	HNO_3	%		$m^2 g^{-1}$	$m^2 g^{-1}$	$cm^3 g^{-1}$	$mmol g^{-1}$
Parent L	-	-	-	53	387	12	0.18	0.288
AT-0.05L	5	-	66	36	442	88	0.16	0.410
AT-0.1L	3	-	60	37	452	134	0.14	0.371
AT-0.2L	1	-	55	33	443	152	0.12	0.310
AAT-1L	1	2	-	43	451	155	0.12	0.257
AAT-2L	1	2	-	55	435	148	0.11	0.198
Parent S	-	-	-	51	410	65	0.17	0.291
AT-0.05S	5	-	63	34	447	123	0.15	0.430
AT-0.1S	3	-	52	35	500	180	0.14	0.358
AT-0.2S	1	-	56	34	520	215	0.14	0.344

[a)] Si/Al: atomic ratio of Si/Al in the sample.

[b)] S_{BET}: BET surface area

[c)] S_{EXT}: External surface area

[d)] V_{micro}: Micropore volume

[d)] Acid amount: Estimated by the NH_3-TPD.

Table 3.2 Acid properties of parent, alkali-treated and alkali-acid-treated H-ZSM-5 catalysts

Catalyst	**Amount of BASs** [a]	**Amount of LASs**[a]	**BAS/LAS**
	mmol g^{-1}	mmol g^{-1}	
Parent L	0.17	0.019	9.1
AT-0.05L	0.25	0.027	9.1
AT-0.1L	0.18	0.067	2.7
AT-0.2L	0.13	0.089	1.4
AAT-1L	0.13	0.042	3.0
AAT-2L	0.12	0.015	7.8
Parent S	0.18	0.015	12
AT-0.05S	0.27	0.026	10
AT-0.1S	0.19	0.053	3.5
AT-0.2S	0.13	0.093	1.4

a) The amounts of BASs and LASs were calculated from corresponding IR peak areas by using the extinction coefficients reported in Ref. 14.

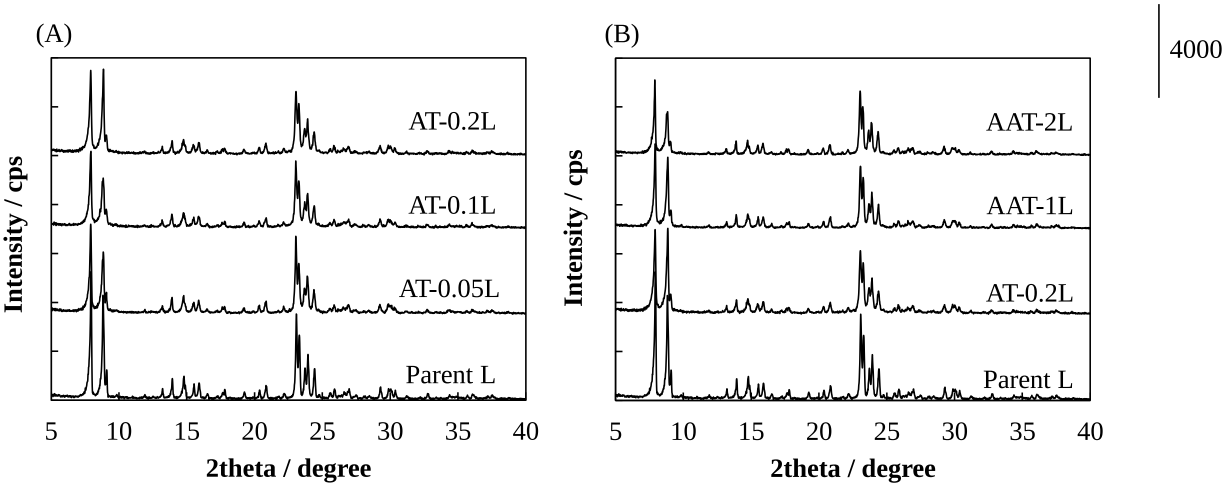

Figure 3.1

XRD patterns of H-ZSM-5 catalysts; (A) L series, (B) AAT series

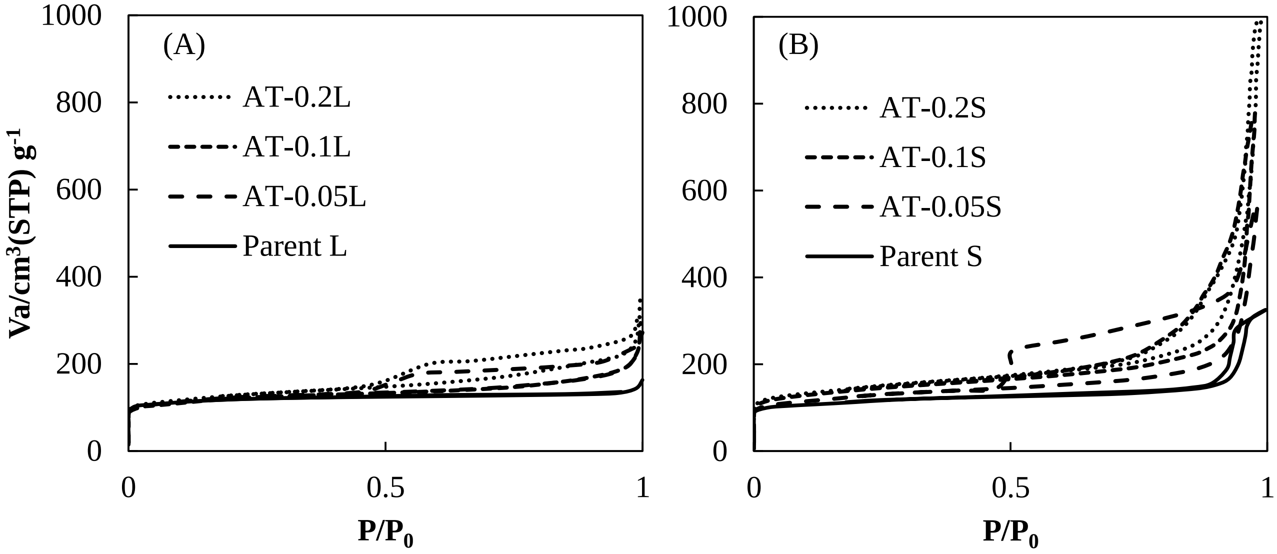

Figure 3.2

N_2 adsorption and desorption isotherms of H-ZSM-5 catalysts; (A) L series, (B) S series

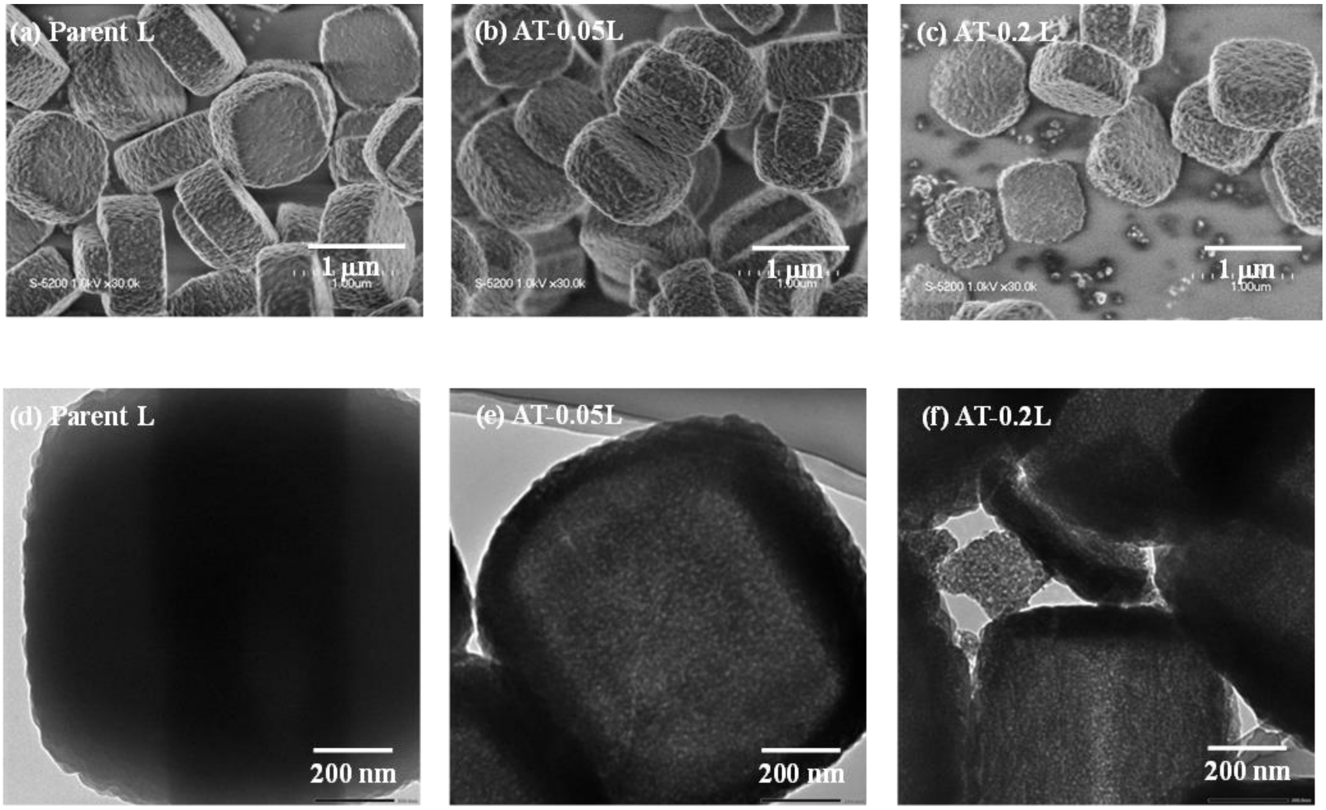

Figure 3.3

FE-SEM and TEM images of H-ZSM-5 catalysts; (a),(d) Parent, (b), (e) AT-0.05L, (c), (f) AT-0.2L

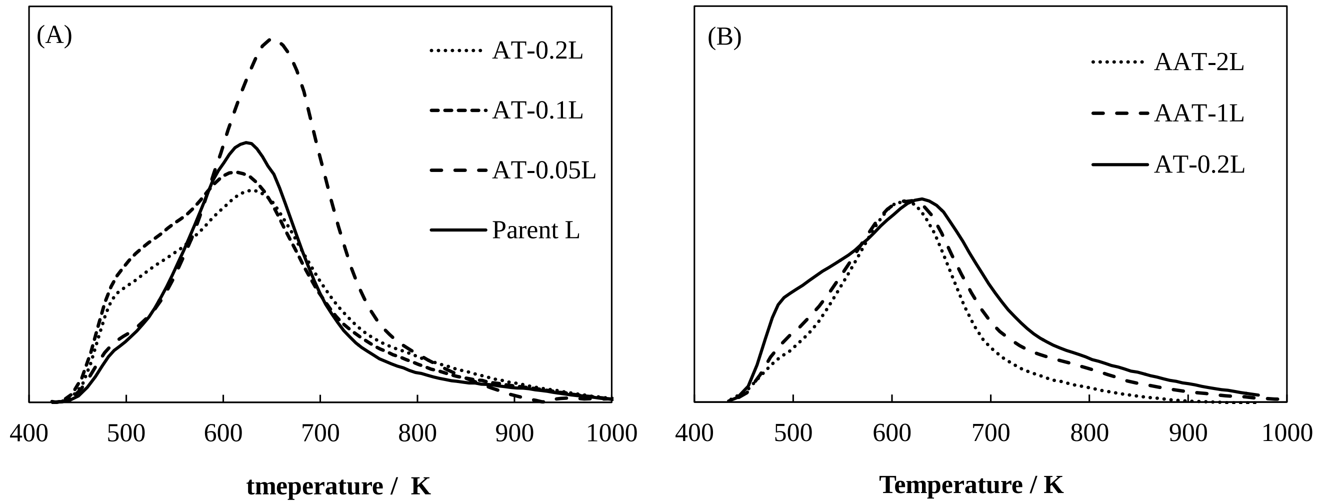

Figure 3.4

NH_3 TPD profiles of H-ZSM-5 catalysts; (A) L series, (B) AAT series

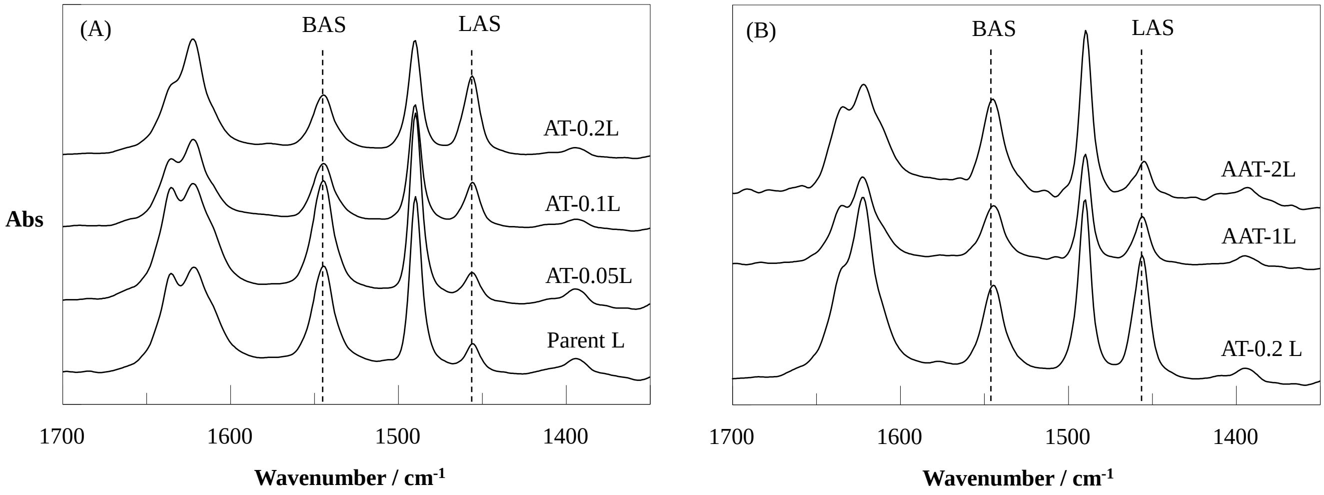

Figure 3.5

FT-IR spectra of pyridine-adsorped H-ZSM-5 catalysts; (A) L series, (B) AAT series

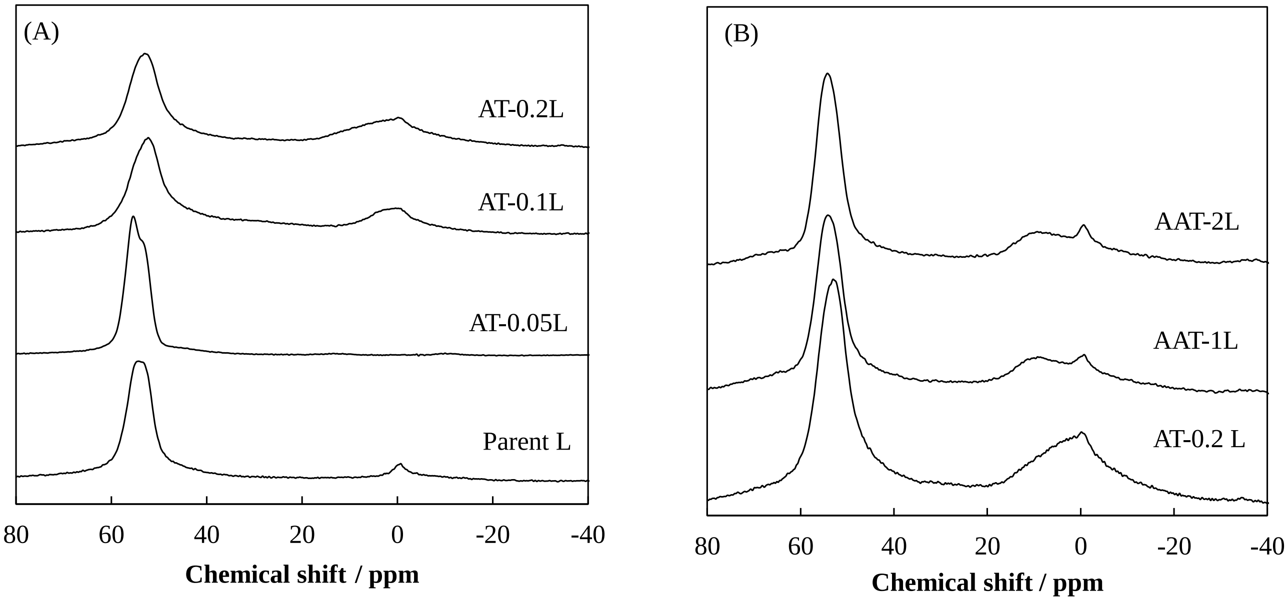

Figure 3.6

The ^{27}Al MAS NMR spectra of H-ZSM-5 catalysts; (A) L series , (B) AAT series

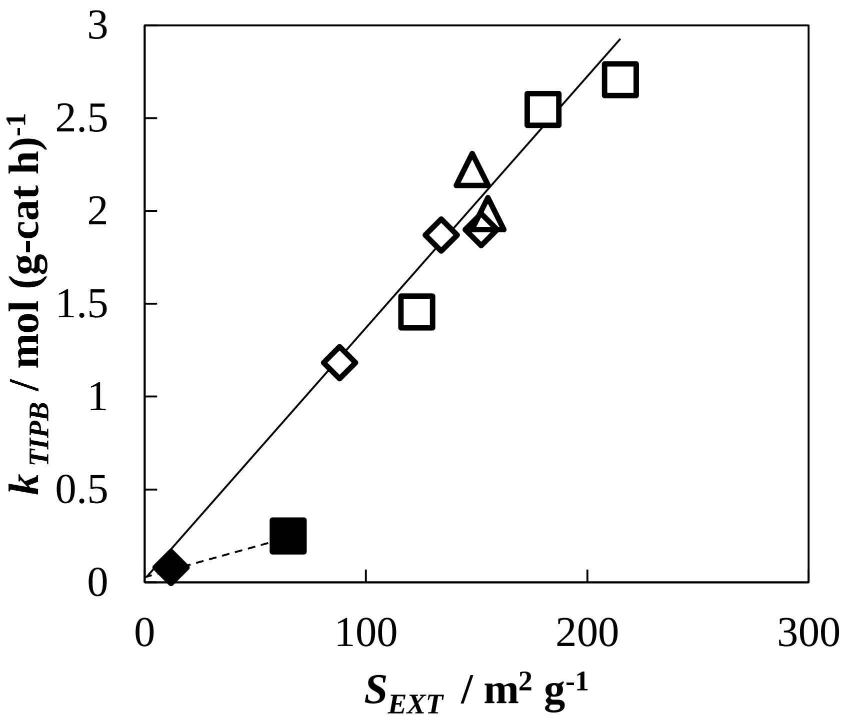

Figure 3.7

Relationship between TIPB cracking activities and external surface.

Parent (Solid symbol), Post-treated sample (Open symbol)

S series (◇), L series (□), AAT L series (△)

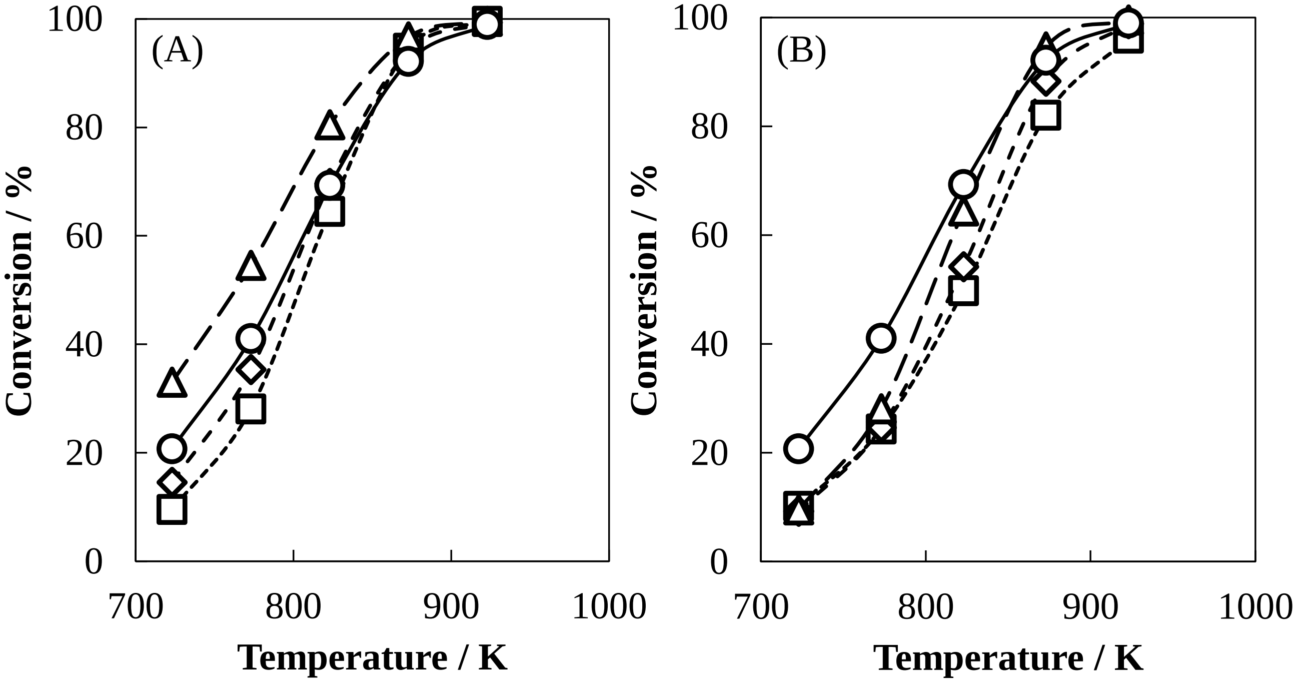

Figure 3.8

n-hexane cracking over H-ZSM-5 catalysts with the reaction temperature varied ranging from 723 to 923 K; (A) L series; Parent L (○), AT-0.05L (△), AT-0.1L (◇), AT-0.2L (□), (B) AAT L series; Parent L (○), AT-0.2L (△), AAT-1 (◇), AAT-2L (□)

Reaction conditions: 0.05 g catalyst, W/F = 16 g-cat h / mol-*n*-hexane, Partial pressure of *n*-hexane = 6.0 kPa, 723-923 K, TOS = 10 min.

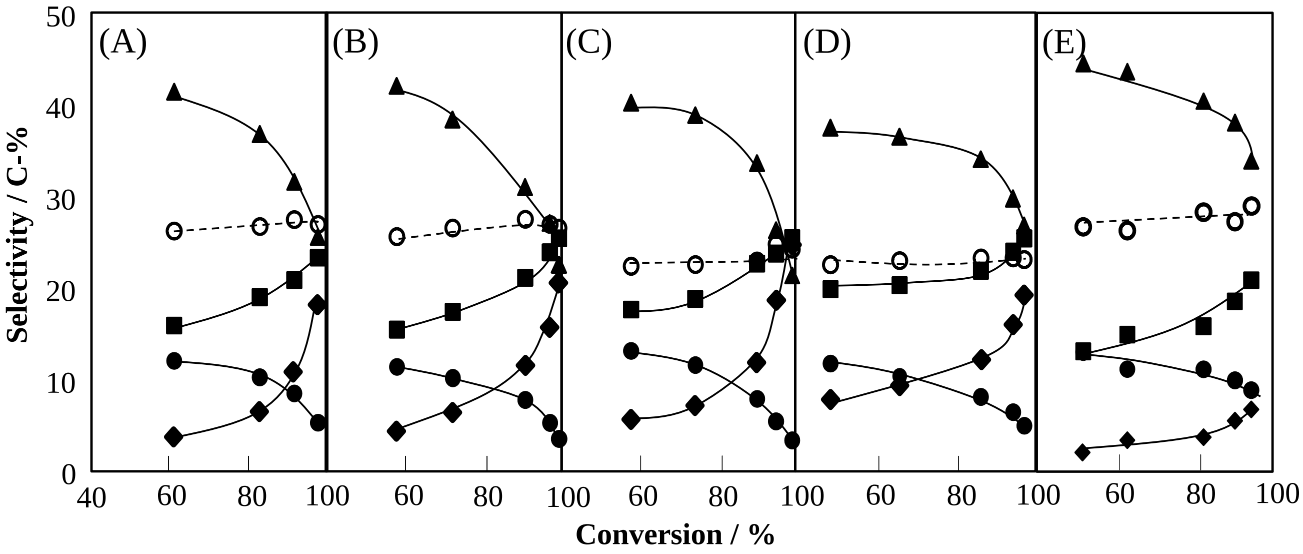

Figure 3.9

Product distribution of *n*-hexane cracking over H-ZSM-5 catalysts with the various conversions; (A) ParentL, (B) AT-0.05L, (C) AT-0.1L, (D) AT-0.2L, (E) AAT-2L

Propylene (▲), Ethylene (■), Butenes (●), BTX (◆), C1-C4 paraffins (○)

Reaction conditions: 0.01-0.1 g catalyst, W/F = 2.5-32 g-cat h / mol-*n*-hexane, Partial pressure of *n*-hexane = 6.0 kPa, 873 K, TOS = 10 min.

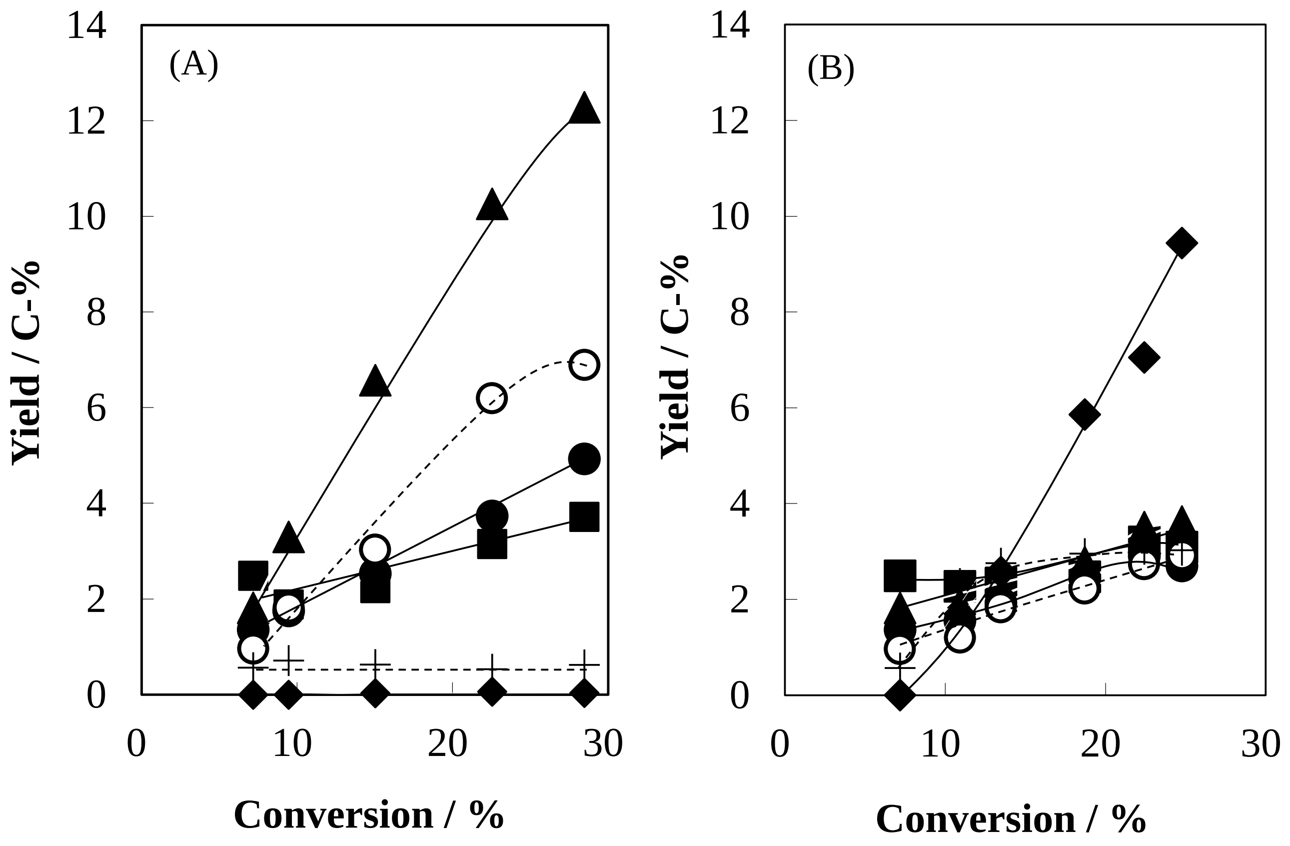

Figure 3.10

n-hexane conversion over (A) H-ZSM-5 (Si/Al = 500) and (B) γ-Al_2O_3

Propylene (▲), Ethylene (■), Butenes (●), BTX (◆), C1-C4 paraffins (○), C5+ (+)

Reaction conditions: 0.01-0.1 g catalyst, W/F = 2.5-32 g-cat h / mol-*n*-hexane, Partial pressure of *n*-hexane = 6.0 kPa, 923 K, TOS = 10 min.

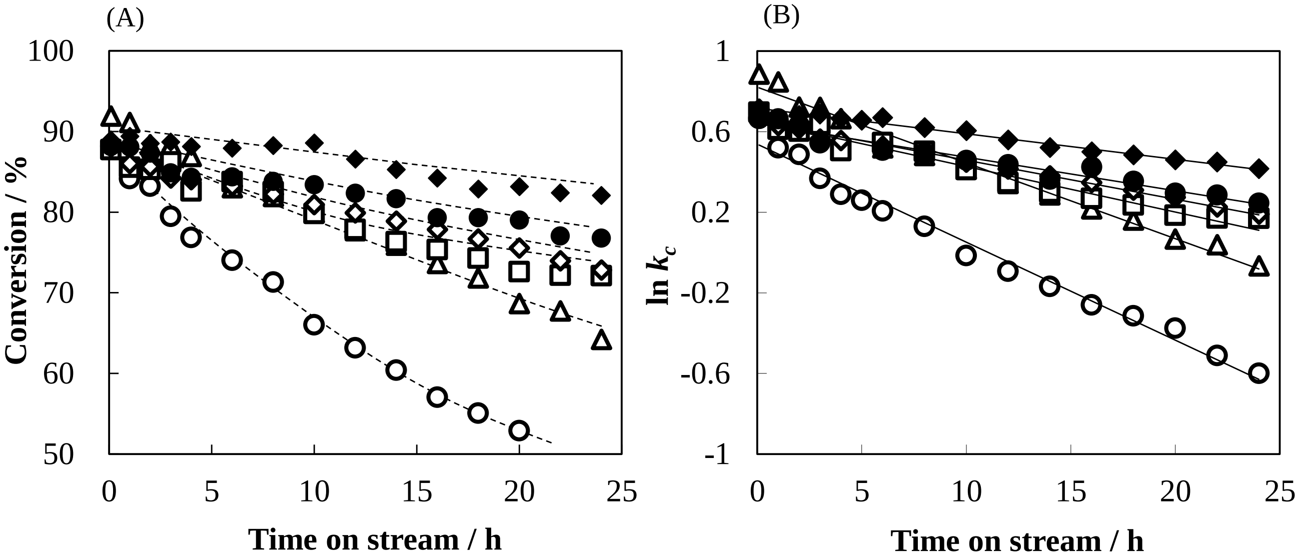

Figure 3.11

n-hexane cracking over alkali-treated H-ZSM-5 catalysts; (A) change in the conversion against time on stream, (B) change in the Ln *kc* against time on stream

Parent L (○), AT-0.05 L (△), AT-0.1 L (□), AT-0.2 L (◇), Parent S (●), AT-0.2 S (◆)

Reaction conditions: 0.01 (Parent: 0.016) g catalyst, W/F = 1 (Parent: 1.6) g-cat h / mol-*n*-hexane, Partial pressure of *n*-hexane = 23.0 kPa, 923 K.

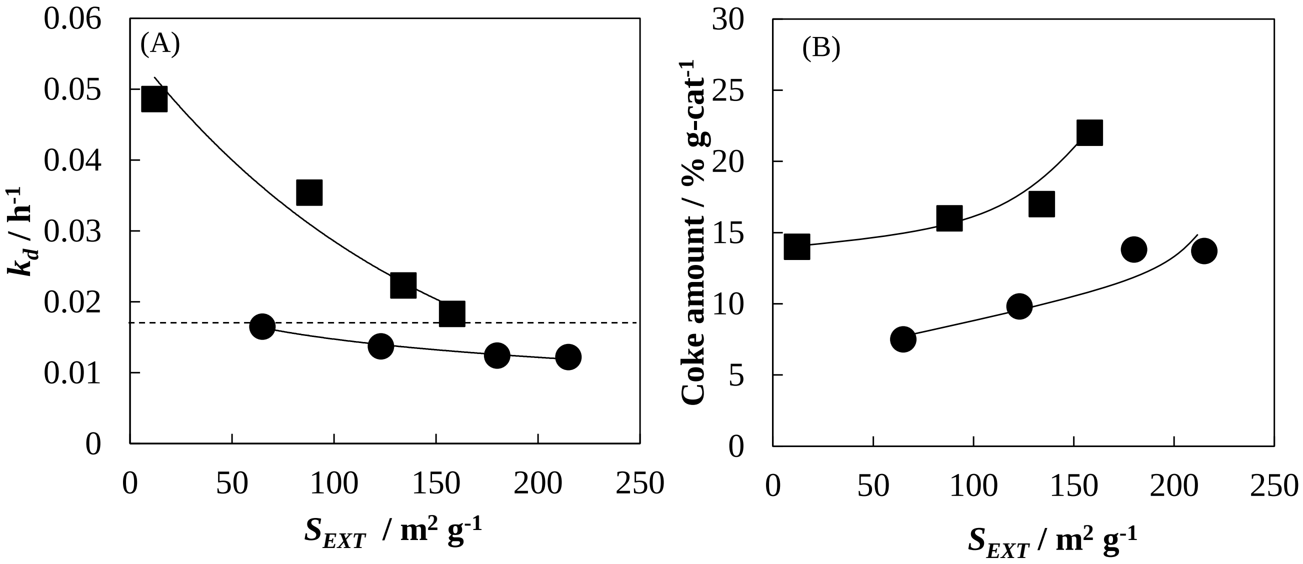

Figure 3.12

Relationship between external surface area and (A) deactivation rate constant, (B) the amount of coke formed for 24 h

L series (■), S series (●)

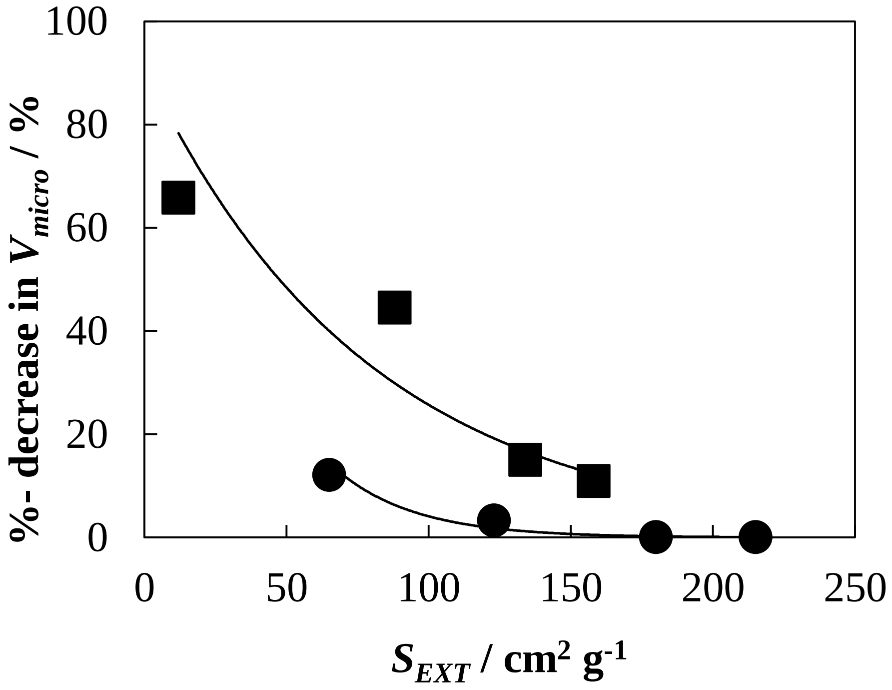

Figure 3.13

Relationship between external surface area and percent decrease in micro pore volume

L series (■), S series (●)

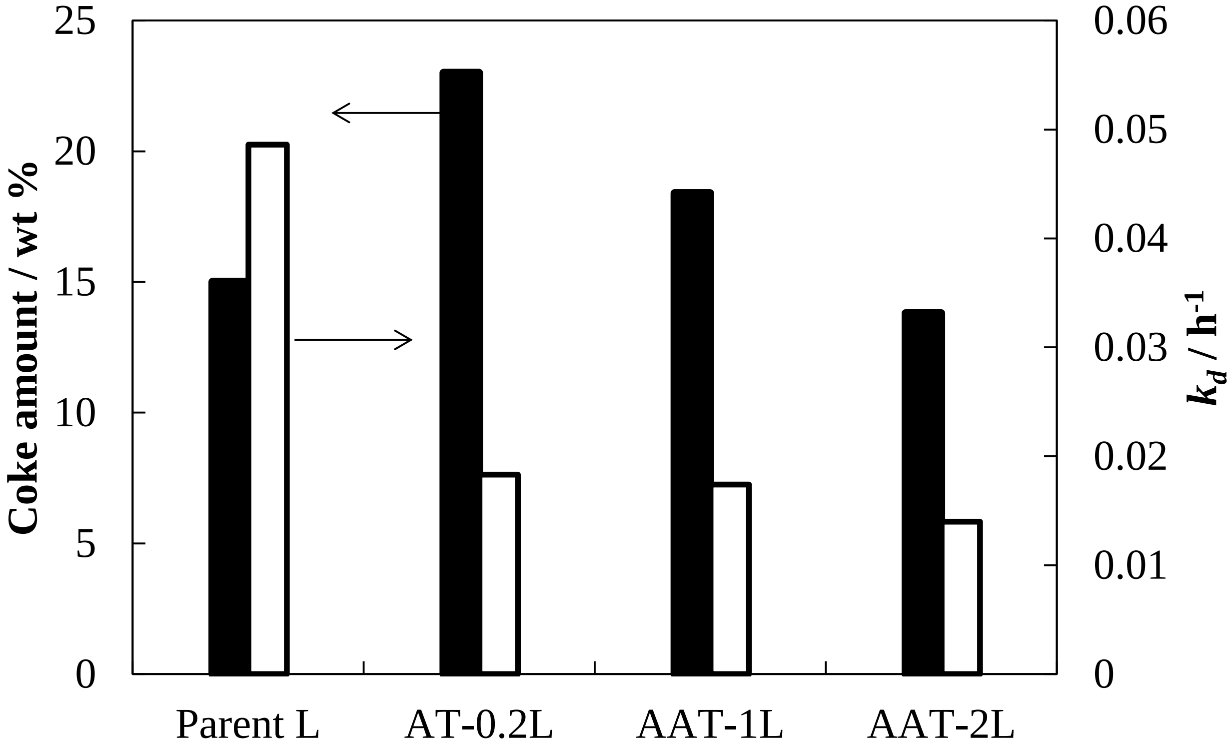

Figure 3.14

Influence of Lewis acid sites on coke formation and deactivation rate constant.

Chapter 4

Effect of Al content and Al state of H-ZSM-5 on catalytic activity for *n*-hexane cracking

4-1 Abstract

Effects of the Al content (Si/Al = 20 - 660) in the H-ZSM-5 zeolite synthesized with tetrapropylammonium and sodium cations on the distribution of Al atom in the framework over 12 crystallographically distinct T-sites, acid property, catalytic activity and mechanism of *n*-hexane cracking were examined. From ^{27}Al MAS NMR, the H-ZSM-5 zeolites with the Al contents varied differ in the distribution of Al atom. The Al atoms in the ZSM-5 zeolites with a higher Al content preferentially occupy the T-sites with smaller T-O-T angles. However, there is no marked difference in the strength of Brønsted acid on these H-ZSM-5 zeolites estimated from the CO-adsorbed FT-IR measurement. The *n*-hexane cracking was carried out at two different temperature regions (673-773 and 823-923 K). I found that the *n*-hexane cracking over the H-ZSM-5 (Si/Al = 20 - 660) catalysts obeyed the first-order kinetics, regardless of the reaction temperature and the Al content. At the lower reaction temperature region, the activity and activation energy were significantly affected by the Al content because the bimolecular cracking that requires a low activation energy is predominant at high Al contents. On the other hand, at the higher reaction temperature region, the monomolecular cracking was predominant and the Al content scarcely affected the ratio of the reaction mechanism. Furthermore, the activation energy for monomolecular cracking was decreased with an increase in the Al content. It is probably because Brønsted acid sites at the T-sites in H-ZSM-5 are not identical in the catalytic activity.

4-2 Introduction

The acidic properties of zeolites are closely related to the nature and distribution of the Al atoms in the framework. Therefore, detailed characterization of the Al environment is essential for understanding the catalytic properties. The **MFI** structure has 12 crystallographically distinct T-sites. Recently, the development of ^{27}Al MQMAS NMR experiment has advanced the study on the structure of AlO_4 in zeolite frameworks. Han and co-workers reported that ^{27}Al MAS NMR spectra of the ZSM-5 samples with different Al contents consist of two peaks irrespective of the Al content, and they concluded that the preference of Al atoms for particular T-sites in ZSM-5 depends strongly on the framework Al content [1].

There have been various discussions about the mechanism of paraffin cracking. Haag and co-workers have reported that for the cracking of various paraffins over H-ZSM-5, the intrinsic activation energies are identical, and the differences in the apparent activation energies are due to the difference in the adsorption heats of paraffins, not the acid strength [2]. Then, several groups have followed this idea [3-5]. On the other hand, Niwa and co-workers have discussed a relationship between Brønsted acid strength on the **FAU**-type zeolite and the catalytic activity and activation energy for paraffin cracking [6-8]. They concluded that the Brønsted acid strength of the zeolite is a crucial factor for influencing the activity and activation energy for paraffin cracking, rather than the adsorption heats. Gounder and Iglesia have reported that the spatial constraints of the zeolytic structure around Brønsted acid sites affect the stability of transition states, resulting in the difference in the cracking activity [9, 10]. Considering these reports, the adsorption heats, the Brønsted acid strength and the spatial constraints around Brønsted acid sites would be strongly affected by the Al position among 12 T sites in the **MFI**-type framework. Therefore, it is expected that the Al content of H-ZSM-5 would affect the catalytic activity and activation energy for paraffin cracking.

However, the activity and activation energy for paraffin cracking are strongly affected by reaction mechanism [11]. Haag and Dessau have reported that paraffin cracking proceeds along the monomolecular cracking *via* penta-coordinated carbonium ion as intermediate or the classical bimolecular cracking *via* carbenium ion as intermediate formed by a hydride transfer reaction [12-14]. The rate-limiting step for the bimolecular cracking is a hydride transfer reaction between paraffin and adsorbed carbenium ion with low activation energy. This mechanism is predominant at low reaction temperatures, high paraffin pressures, high paraffin conversions and high Al contents in zeolites. On the other hand, the monomolecular cracking requires high activation energy. This mechanism is predominant at high reaction temperatures, low paraffin pressures, low paraffin conversions and low Al contents. Therefore the activation energy should be dependent on the reaction conditions including reaction temperatures and paraffin pressures, and conversion, and the Al content, affecting the ratio of two mechanisms [11].

In the bimolecular cracking, the hydrocarbons smaller than C3 are not formed because these products need to form *via* energetically unfavorable primary carbenium ions. In contrast, in the monomolecular cracking, a penta-coordinated carbonium ion formed by protonation of paraffins decomposes to a carbenium ion and hydrogen or lower paraffins involving methane and ethane. Hence, the formation of methane, ethane and hydrogen is a parameter of the contribution of monomolecular cracking [13, 15].

In this chapter, first, the effects of Al contents in the H-ZSM-5 zeolites on the Al distribution among 12 distinct T-sites and Brønsted acid strength were examined. Then, I carried out *n*-hexane cracking over the H-ZSM-5 catalysts with various Al contents at two different temperature regions (673-773 and 823-923 K). I focus on the behavior of the formation of hydrogen, methane, and ethane to clarify the effect of the Al content on the reaction mechanism and the activation energy at high temperatures.

4-3 Experimental

4-3-1 Synthesis of ZSM-5 catalysts

ZSM-5 catalysts with various Al contents were synthesized as follows. The gels with two different compositions of 1 SiO_2: 0.02 - 0.0005 Al_2O_3: 0.25 TPAOH: 0.12 Na_2O: 20 H_2O were prepared from tetraethyl orthosilicate (TEOS), tetrapropylammonium hydroxide (TPAOH), aluminium nitrate and NaOH. Crystallization was carried out at 443 K for 72 h. The Na-type ZSM-5 (Na-ZSM-5) samples were obtained by calcination of the as-synthesized sample in an oven at 823 K to remove TPA cations. The calcined Na-ZSM-5 samples were treated with 1 M NH_4NO_3 aq. at 353 K for 3 h twice. Thus obtained NH_4^+-type zeolites (NH_4-ZSM-5) were converted into *in situ* H-forms by heating at 773-923 K under inactive gas (He or Ar) atmosphere or vacuum conditions just before the measurements and reactions to avoid dealumination [16]. The products were designated as H-ZSM-5 (*x*), where *x* is the Si/Al ratio determined by the ICP elemental analysis.

4-3-2 Characterizations

XRD patterns were collected on a Rint-Ultima III (Rigaku) using a Cu Kα X-ray source (40 kV, 20 mA). Nitrogen adsorption measurements to determine the BET surface area (S_{BET}), S_{EXT} , and micropore volume (V_{micro}) were conducted at 77 K on a Belsorp-mini II (Bel Japan). S_{EXT} and V_{micro} were estimated by the *t*-plot method. Field-emission scanning electron microscopic (FE-SEM) images of the powder samples were obtained on an S-5200 microscope (Hitachi) operating at 1-30 kV. The sample was mounted on a carbon-coated microgrid (Okenshoji Co.) without any metal coating. Si/Al ratios of the samples were determined by using an inductively coupled plasma-atomic emission spectrometer (ICP-AES, Shimadzu ICPE-9000). Na contents of the samples were determined by using atomic absorption spectrometer (AAS, Shimadzu AA-6200).

The high-resolution ^{27}Al MAS NMR and ^{27}Al 3Q MQMAS NMR spectra were obtained on a JEOL ECA-600 spectrometer (14.1 T) equipped with an additional 1 kW power amplifier. For ^{27}Al 3Q MQMAS NMR spectra, pulse durations were 5.5 μs, 2.1 μs and 0.2 ms for the 3Q excitation pulse, the 3Q-1Q conversion pulse and z-filter, respectively. The relaxation delay time was 10 ms. The ^{27}Al chemical shift was referenced to $AlNH_4(SO_4)_2{\cdot}12H_2O$ at -0.54 ppm and samples were spun at 17 kHz by using a 4 mm ZrO_2 rotor. For high-resolution ^{27}Al MAS NMR spectra at 14.1 T, which were recorded using a single pulse, the pulse width was set at 0.1 μs and 10000 scans were accumulated at a sample spinning rate of 17 kHz. A 10 ms relaxation delay was determined so as to be long enough to permit quantitative analysis of zeolite samples. $AlNH_4(SO_4)_2{\cdot}12H_2O$ was also used as a reference for the ^{27}Al chemical shift.

Temperature-programmed ammonia desorption (NH_3-TPD) profiles were recorded on a Multitrack TPD equipment (Japan BEL). Typically, 30 mg catalyst was pretreated at 923 K in He (50 mL min^{-1}) for 1 h and then cooled to 423 K. Prior to the adsorption of NH_3, the sample was evacuated at 423 K for 1 h. Approximately 2500 Pa of NH_3 was allowed to make contact with the sample at 423 K for 10 min. Subsequently, the sample was evacuated to remove weakly adsorbed NH_3 at the same temperature for 30 min. Finally, the sample was cooled to 423 K and heated from 423 to 1073 K at a ramping rate of 10 K min^{-1} in a He flow (50 mL min^{-1}). A mass spectrometer was used to monitor desorbed NH_3 (m/e = 16). The amount of acid sites was determined by using the area in the profiles.

Spectra of Fourier transform infrared spectroscopy (FT-IR) were obtained at a resolution of 4 cm^{-1} using a Jasco 4100 FTIR spectrometer equipped with a mercury cadmium telluride (MCT) detector. A total of 64 scans were averaged for each spectrum. IR spectra of the clean disk were recorded *in* *vacuo* at 153 K to obtain background spectra. The sample was pressed into a self-supporting disk (20 mm diameter, 30 - 60 mg) and placed in an IR cell attached to a conventional closed-gas circulation system. The sample was pretreated by evacuation at 773 K, followed by adsorption of CO with 2-30 Pa at 153 K. Then, the sample was evacuated at the same temperature for 30 min. The spectra were recorded at 153 K.

4-3-3 Catalytic cracking of *n*-hexane

The catalytic cracking of *n*-hexane was performed in a conventional fixed bed reactor under Argon at atmospheric pressure. The NH_4-ZSM-5 catalyst was put into a quartz reactor of 4 mm i.d. and activated in flowing Argon at 923 K for 1 h prior to the reaction, and then cooled to the reaction temperature ranging from 623 to 923 K. The initial partial pressure of *n*-hexane was set at 5 kPa. The W/F (W: amount of catalyst /g, F: total flow rate /mol h^{-1}) was adjusted to obtain < 20% of the *n*-hexane conversion. The hydrocarbon products were analyzed with an on-line gas chromatograph (Shimadzu GC-2014) with an FID detector and a capillary column (PLOT Fused Silica 30 m×0.53 mm, 6μm film thickness). Hydrogen was analyzed by a gas chromatograph (Shimadzu, GC-2014) with a TCD detector and a packed column (Molecular sieve 5A). The selectivities were expressed as mol% based on the mol number of individual product or (mol number of each individual product) / (100 moles *n*-hexane reacted).

4-4 Results and discussion

4-4-1 Physicochemical properties of H-ZSM-5

From the XRD patterns, all of the samples were identified as the **MFI**–type structure with a high crystallinity irrespective of the Si/Al ratio. The Si/Al ratios determined by ICP analysis were ranging from 20 to 660 and these samples contained little amount of Na^+ ions. FE-SEM observation indicated that the crystallite sizes of all of the prepared samples were less than 1 μm. The N_2 adsorption and desorption isotherms for all of the H-ZSM-5 zeolites exhibited a typical isotherm of microporous materials with a plateau at high relative pressures (type I, IUPAC). The BET surface area (S_{BET}), the external surface area (S_{EXT}) and micropore volume (V_{micro}) were almost the same (Table 4.1). From the XRD patterns and these results, the prepared H (NH_4) -ZSM-5 samples have similar structural qualities. The acid amounts esimated by the NH_3-TPD measurement depended on the Si/Al ratios and were nearly similar to the Al content determined by the ICP analysis in all of the H-ZSM-5 zeolites (Table 4.1). These results suggest that almost all of the Al atoms incorporated into the **MFI**-type framework worked as acid sites. The slight difference between the Al content determined by ICP analysis and the acid amount would be caused by the dealumination during calcination. When NH_4-ZSM-5 (20) was calcined in air with moisture at 923 K before NH_3-TPD measurement, the dealumination occurred and the acid amount was decreased from 0.77 to 0.50 mmol g^{-1}. Therefore, to avoid the dealumination of H-ZSM-5 zeolites, the pretreatment of several characterizations and reaction was carried out under inactive gas (He or Ar) atmosphere or vacuum conditions.

4-4-2 Al state in framework and acid properties

The state of the Al species was examined by ^{27}Al NMR. Figure 4.1 shows the ^{27}Al MAS NMR spectra of the NH_4-ZSM-5 zeolites with different Al contents. The peak at 0 ppm assigned as octahedrally coordinated Al atoms was not observed in all of the samples; there are quite a little or no extra framework Al atoms in the samples. All spectra consist of two peaks at ca. 53 (Peak VI_I) and 56 (Peak VI_{II}) ppm assigned as tetrahedrally coordinated Al atoms. The resolution of the ^{27}Al MAS NMR spectra is not high enough to detailedly characterize Al species because quadrupolar interaction at Al ($I = 5/2$) leads to a broadening of the peak; the sizable second-order quadrupolar interaction at Al, which contains higher-rank anisotropic terms, cannot be completely averaged out by MAS [17-19].

Thus, ^{27}Al MQMAS NMR was used to characterize the state of the Al coordination in detail. Figure 4.2 representatively shows the ^{27}Al MQMAS NMR spectra with 45-70 ppm on the F2 projection for the NH_4-ZSM-5 samples with the Si/Al ratios of 20, 52 and 125, indicating that two cross-sections were clearly observed irrespective of the Si/Al ratio; the Al atoms are located at two different T-sites in the 12 distinct T-sites. In the ^{27}Al MQ MAS NMR spectra, the peak VI_I of ZSM-5 with a low Al content was clearer than that of ZSM-5 with a high Al content. As shown Figure 4.1, the intensity ratio of peak VI_I to VI_{II} were decreased with a decrease in the Al contents. These results are in good agreement with the findings by Han and co-workers [1]. In several literatures, a rough linear relationship between the isotropic chemical shifts in ^{27}Al MAS NMR spectra and the average T-O-T angle is observed and the chemical shift of ^{27}Al NMR is increased with a decrease in the average T-O-T angles [1, 17, 20, 21]. Hence, the proportion of the Al atoms that occupies the T-sites with smaller T-O-T angles is increased along with the Al content. The Al distributions in the 12 distinct T-sites would be strongly affected by the synthesis conditions, such as Al or SiO_2 source, organic SDAs and presence or absence of alkali cations [22-29]. The ZSM-5 zeolites using in the present study were synthesized under the same conditions except for an Al amount. Therefore, it is concluded that thus observed difference in the Al distribution is due to the Al amount.

In order to clarify the effect of Al distribution on the acid properties, the CO-adsorbed FT-IR measurements were conducted for the H-ZSM-5 with various Al contents. In all of the H-ZSM-5 zeolites, typical IR bands characteristic for acidic OH groups at 3620 cm^{-1} and for terminal Si–OH groups at 3746 cm^{-1} were found at 153 K before the CO adsorption. The band for Al–OH groups formed by dealumination at 3650 cm^{-1} was not observed except for H-ZSM-5 (20). These results are consistent with the NH_3-TPD and ^{27}Al MAS NMR results. Figure 4.3 shows the differential FT-IR spectra for the CO-adsorbed H-ZSM-5 zeolites with the Si/Al ratios of 20, 52 and 125, and Table 4.2 summarizes the results of the CO-adsorption experiments. In the spectra of the ν(CO) region (Fig. 4.2 A), the bands at 2230 and 2175 cm^{-1} correspond to the stretching mode of ν(C≡O) on Lewis and Brønsted acid sites, respectively [30, 31]. In the H-ZSM-5 zeolites with high Al contents ($Si/Al \leq 52$), the intensity of the band at 2230 cm^{-1} was significantly low compared to that of the band at 2175 cm^{-1}. On the contrary, in the H-ZSM-5 zeolites with low Al contents ($Si/Al \geq 125$), the band at 2230 cm^{-1} were not observed, revealing that Brønsted acid sites are predominant and that Lewis sites are quite a little or none. In the spectra of the ν(OH) region (Fig. 4.3 B), the band attributed to acidic OH groups was shifted from 3620 to 3306 cm^{-1} due to the interaction of CO with acidic OH groups in all H-ZSM-5 zeolites. The magnitude of this shift (ΔOH) is related to the acid strength of the acidic OH groups [30, 31]. There is no marked difference in ΔOH between these H-ZSM-5 zeolites; the strength of Brønsted acid on these H-ZSM-5 zeolites is quite similar to each other. In conclusion, the strength of Brønsted acid would be little affected by Al position over T-site.

4-4-3 Effect of Al content in H-ZSM-5 zeolites on activity for *n*-hexane cracking

To evaluate the effect of Al content in the H-ZSM-5 zeolites on *n*-hexane cracking behavior, kinetics of *n*-hexane cracking over the H-ZSM-5 catalysts at various reaction temperatures were examined. It is known that the catalytic cracking of *n*-hexane obeys the first-order kinetics regardless of reaction mechanisms [14, 32]. Thus, the rate constant for cracking (k_c) can be expressed as follows:

$$k_c \times W/F = -\ln(1 - x) \tag{1}$$

where W is the amount of catalyst, F is the total flow rate and x is the *n*-hexane conversion. However, *n*-hexane was converted by thermal cracking at above 823 K in my reaction conditions.

Kubo and co-workers have reported that both the catalytic cracking and the thermal cracking at high temperatures obey the first-order kinetics [15]. Therefore, the following equation can be applied in the high temperature reaction:

$$k_c \times W/F + k_t \times \mathrm{V}/F = -\ln(1-x) \qquad (2)$$

$$k_c \times W/F = -\ln(1-x) - k_t \times \mathrm{V}/F \qquad (3)$$

where k_t is the rate constant for thermal cracking, V is the volume of high temperature region in the reactor. Figure 4.4 shows the effect of the W/F on the rate of *n*-hexane cracking over the H-ZSM-5 catalysts with various Al contents at 623 and 923 K. It is apparent that *n*-hexane cracking over the H-ZSM-5 zeolites obeyed the first-order kinetics regardless of the reaction temperature and the Al contents. The contribution of the bimolecular cracking of *n*-hexane over the H-ZSM-5 zeolites would be increased along with the Al content and a decrease in the reaction temperature. Therefore, *n*-hexane cracking over the H-ZSM-5 zeolite obeys the first-order kinetics regardless of the ratio of monomolecular cracking mechanism to bimolecular cracking one.

From the equations (1) and (3), the slope of the plots in Figure 4.4 exhibits the rate constant for the *n*-hexane cracking (k_c). Figure 4.5 shows the relationship between the common logarithm of k_c and that of the Al content in the H-ZSM-5 catalysts. At 623 K, the slope of the straight line obtained upon plotting log k_c vs log [Al content] is about 2.3. The slope was decreased along with the reaction temperature, suggesting that the apparent order with respect to the Al content was decreased with an increase in the reaction temperature. As shown in Figure 4.6, the apparent order with respect to the Al content is more than one at every reaction temperature. This result suggest that the reaction rate per Al atom was increased with an increase in the Al content at every reaction temperature. The order was decreased along with the reaction temperature; the order was decreased from 2.3 to 1.1 when the temperature was increased from 623 to 923 K. These findings indicate that, at low reaction temperature, the dependence of the Al content in the H-ZSM-5 zeolites on the reaction rate is significantly larger than that at high temperatures.

Figure 4.7 shows the activation energy for the *n*-hexane cracking at two different temperature regions, indicating that the activation energy was increased with a decrease in the Al content and that the activation energy at the higher reaction temperature region was higher than that at lower reaction temperature regardless of the Al content. I have reported that the crystallite sizes (100 nm -1 μm) of H-ZSM-5 do not affect the activity for *n*-hexane cracking at 823 - 923 K, and that the *n*-hexane cracking over the H-ZSM-5 zeolite with the crystallite size of below 1 μm is not limited by diffusion of *n*-hexane under such reaction conditions in chapter 2. As shown in Table 4.1, the crystallite sizes of every H-ZSM-5 zeolite used as a catalyst for the *n*-hexane cracking are smaller than 1μm. Hence, it is considered that the ratio of cracking mechanism (= monomolecular cracking / bimolecular cracking) is dependent on the Al content in the H-ZSM-5 zeolites.

4-4-4 Effect of Al content in H-ZSM-5 zeolites and reaction temperature on reaction mechanism

The reaction mechanism affects not only the reaction rate but also the selectivity. Post and co-workers reported that C1 and C2 hydrocarbons are typical products of the monomolecular cracking and iso-butane (i-C4) is a typical product resulting from β-scission reactions because the tertiary carbenium ion is the most stable carbenium ion. Post and co-workers discussed the reaction mechanism of the *n*-hexane cracking based on the cracking mechanism ratio (CMR), which has been generally applied as a parameter to estimate the cracking mechanism, as follows [11]

$$\mathrm{CMR} = (\mathrm{C1} + \Sigma\mathrm{C2})/\text{i-C4}.$$

where C1, ΣC2 and i-C4 are the molar selectivities to methane, ethane and ethylene, and iso-butane respectively. Here, I have considered the mechanism for cracking based on the CMR value; the CMR values at the conversion of ca 10 % were calculated based on the results of the *n*-hexane cracking over the H-ZSM-5 zeolites at the reaction temperatures of 623 and 923 K, and they are listed in Table 4.3 with the selectivities of the products. At 623 K, the selectivities and the values of CMR were significantly affected by the Al content; the value of CMR was increased with a decrease in the Al content (3.1 to 125), suggesting that the contribution of the monomolecular cracking is increased with a decrease in the Al content at 623 K. This consideration is consistent with that by Post and co-workers [11]. The selectivities to propylene and butenes were decreased with an increased in Al content, while those to propane and butanes were increasing with a decrease in the Al content. The increase in the selectivities to C3 and C4 paraffins would be caused by a hydride transfer reaction between propyl- or butylcarbenium ions and *n*-hexane.

On the other hand, at 923 K, the Al content in the H-ZSM-5 zeolites has little influence on the selectivities. Note that the values of CMR (ca. 134 - 210) were remarkably higher compared to those at 623 K. The selectivities to propylene and butenes were also significantly higher than those of propane and butanes. From these results, it is considered that the contribution of the hydride transfer reaction is significant low and the ratio of the reaction mechanism is little affected by the Al content at high temperature regions, being in agreement with the difference in the activation energy at different temperature regions. Note that, however, under my reaction conditions, the consideration based on the values of CMR would not be adopted to estimate the ratio of the cracking mechanism. In my system, primary carbenium ions would be formed at high reaction temperature at above 873 K, resulting in the formation of ethylene not only by the monomolecular cracking but also by the bimolecular cracking (in chapter 2). Furthermore, the selectivity to iso-butane at high reaction temperature is significantly low (Table 4.3). Therefore, the CMR value will be significantly changed by a slight formation of iso-butane.

Kubo and co-workers discussed the ratio of the cracking mechanism in *n*-heptane cracking over the H-ZSM-5 zeolites at above 723 K focusing on the total selectivities to methane, ethane and hydrogen because these molecules are formed solely by the monomolecular cracking and they are primary products at the conversion of below ca 50 % in low *n*-heptane pressure [15]. Therefore, to clarify the effect of the Al content in the H-ZSM-5 zeolites on the reaction mechanism in *n*-hexane cracking, the relationship between Al content and the total selectivities to hydrogen, methane and ethane were examined.

Figure 4.8 shows the dependence of total selectivities to hydrogen, methane and ethane at the conversion of ca. 10 % on the Al content in the H-ZSM-5 zeolites at various reaction temperatures. The total selectivity was affected by the Al content at below 723 K and the dependence of the Al content was decreased with an increase in the reaction temperature. These findings suggest that the contribution of the monomolecular cracking is increased with a decrease in the Al content and also with an increase in the reaction temperature. On the other hand, the total selectivity was not affected by the Al content at above 823 K; the contribution of the monomolecular cracking is independent on the Al content in H-ZSM-5 at such a high temperature. Under my experimental conditions, the conversion of *n*-hexane by thermal cracking was ca. 0.03 % at 823 K. At 823 K, the contribution of thermal cracking is significantly low at the conversion of ca. 10 %, and the total selectivity by the thermal cracking is negligible. Hence, it is estimated that at least ca. 65 % of *n*-hexane cracking proceeds *via* the monomolecular cracking at 823 K. Therefore, the monomolecular cracking would be dominant at high temperatures (≥ 823 K) in *n*-hexane cracking over the H-ZSM-5 zeolites. Consequently, at the high temperature region, the dependence of the activation energy on the Al content is little affected by change the ratio of reaction mechanism. On the other hand, at low temperature region, the Al content significantly affects the ratio of the reaction mechanism and activation energy.

To estimate the change in the activation energy for the monomolecular cracking of *n*-hexane, the activation energies for the formation of hydrogen, methane and ethane were examined. The formation rates of these molecules should obey the first-order kinetics in addition to the overall reaction rate. Therefore, the formation rates of these molecules constant (k_f) can be expressed as follows:

$$k_f \times W/F = -\ln(1-Y_{all}) - \ln(1-Y_t) \qquad (5)$$

where Y_t is the yields of hydrogen, methane and ethane by thermal cracking, Y_{all} is the yields of hydrogen, methane and ethane by the overall reaction. The dependence of the W/F on the formation rates of these molecules over HZSM-5 (52) at 923 K is shown in Figure 4.9. In all of the products, the proportional relationships were observed. Furthermore, the proportional relationships were also observed irrespective of the Al content. These results indicate that the formation rates of hydrogen, methane and ethane obey the first-order kinetics. Based on the plots in Figure 4.9, the activation energies for their formations are shown in Figure 4.10, indicating that the activation energies are increased with a decrease in the Al content; the activation energy for the monomolecular cracking of *n*-hexane is dependent on the Al content.

4-4-5 Effect of Al state in H-ZSM-5 zeolites on *n*-hexane monomolecular cracking

From activation energies for the formations of hydrogen, methane and ethane, the activity of Brønsted acid sites in the H-ZSM-5 samples is similar irrespective of the Al content. The strength of Brønsted acid sites should affect the formation of carbonium ion, its stabilization and the following cracking of C-C or C-H bond. Okumura and co-workers investigated the effect of Brønsted acid sites strength of **FAU** type zeolites, which is 3-dimensional large pore zeolite, on the activity and activation energy for paraffin cracking. They reported that there is a simple correlation between the acid strength H-Y and modified USY zeolites with various Brønsted acid strengths and activation energy [8]. However, as shown in Figure 4.3 and Table 4.2, the H-ZSM-5 zeolites using in present study had a similar strength of Brønsted acid sites.

The activity and the activation energy of the H-ZSM-5 zeolites would be affected by not only Brønsted acid strengths but also the local structure of around the acid sites more sensitively than those of **FAU** type zeolite, because the **MFI**-type zeolite has smaller pores and has a larger number of T-sites than the **FAU**-type zeolite. It is proposed that carbonium ion is a transition state stabilized by nearly covalent interactions of protons with negatively charged oxygens in the vicinity of the Al atom as shown in Figure 4.11 [33]. Kramer co-workers calculated the site-dependence of the rates of H/D exchange reaction of CD_4 *via* a similar transition state of the monomolecular cracking over H-ZSM-5 zeolite [34, 35]. Between the different T-sites in ZSM-5, the exchange rates will vary because it is influenced by the variation of the proton affinity between crystallographically different oxygen sites. As shown in Figure 4.1, the proportion of the Al atoms that occupy the T-sites with smaller T-O-T angles is increased along with the Al content. I also found that the activation energy for the *n*-hexane cracking was decreased with an increase in the proportion of the Al atoms occupying the T-sites with smaller T-O-T angles. Redondo and co-workers calculated the proton affinities for the 48 distinct oxygen sites in ZSM-5 by using semiempirical quantum chemical calculations [36] and they concluded that there is a direct relationship between the experimental Al-O-Si angle and the proton affinity; the proton affinity is decreased with an increase in the T-O-T angle as shown in Figure 4.12. It is considered that a basicity of lattice oxygen framework would be enhanced by the decrease in the Al-O-Si angle. As a result, the activation energy for the *n*-hexane cracking is decreased because the more Al-O-Si angle is small, the more transition state may be stabilized.

Furthermore, Gounder and Iglesia reported that the partially confinement of transition states of monomolecular cracking lead to a decrease in the free energy of transition state due to the increase in entropies for propane and butane cracking over H-MOR zeolite since the cracking activity on the acid sites within 8-MR was much higher than that on the acid sites within 12-MR [9, 10].

The **MFI** structure consists of parallel and straight 10-MR channels intersected by sinusoidal 10-MR channels. Although the size of both 10-MRs is similar to that of the aromatic ring (ca. 5.5 Å), the intersections of these 10-MRs have large spherical spaces (diameter ca. 10 Å in diameter) [37]. If the acid sites of H-ZSM-5 with high Al contents are located at narrow spaces selectively, the transition state is stabilized by confinement effect and the adsorption heat of *n*-hexane around acid sites is also increased due to van der Waals interactions between *n*-hexane and zeolite pores around the acid sites. However, in the present study, I cannot identify the exact location of active sites in the pores of H-ZSM-5. Further detail deliberation is necessary to investigate relationship between the Al-O-Si angle and the stability of transition state.

4-5 Conclusions

In the *n*-hexane cracking over H-ZSM-5 zeolite, total selectivities to hydrogen, methane and ethane can be applicable as a parameter to estimation of the contribution of the monomolecular cracking of paraffin regardless of reaction temperatures. Additionally, the changes in the activation energy for the monomolecular cracking were estimated from the activation energy for the formation of hydrogen, methane and ethane. I have successfully found that the ratio of the cracking mechanisms of the monomolecular cracking to the bimolecular cracking is dependent on the Al content at low temperatures (≤ 723 K) and that the activation energy is decreased with an increase in the Al content. On the other hand, at high reaction temperatures (≥ 823 K), the monomolecular cracking is dominant and the Al content scarcely affect the reaction mechanism ratio. However, the activation energy for the monomolecular cracking of *n*-hexane is decreased along with the Al content in despite of similar Brønsted acid strength. The H-ZSM-5 zeolites with various Al contents differ in the distribution of the Al atoms over the 12 distinct T-sites. The proportion of the Al atoms that occupy the T-sites with smaller T-O-T angles is increased along with the Al content. It is considered that transition state of the monomolecular *n*-hexane cracking might be stabilized on the active sites with small T-O-T angles.

References

1. O. H. Han, C.-S. Kim, S.B. Hong, Angew. Chem. Int. Ed., 41 (2002), 469.
2. W. O. Haag, Stud. Surf. Sci. Catal., 84 (1994) 1375.
3. T. F. Narbeshuber, H. Vinek and J .A. Lercher, J. Catal., 157 (1995) 388.
4. S. M. Babitz, B. A. Williams, J. T. Miller, R. Q. Snurr, W. O. Haag and H. H. Kung, Appl. Catal., A, 179 (1999) 71.
5. J. A. van Bokhoven, B. A. Williams, W. Ji, D. C. Koningsberger, H. H. Kung and J. T. Miller, J. Catal., 224 (2004) 50.
6. N. Katada, K. Suzuki, T. Noda, W. Miyatani, F. Taniguchi and M. Niwa, Appl. Catal., A, 373 (2010) 208.
7. K Okumura, T Tomiyama, N Morishita, T Sanada, K Kamiguchi, N Katada, M Niwa, Appl Catal A, 405 (2011) 8.
8. M. Niwa, K. Suzuki, N. Morishita, G. Sastre, K. Okumura, N. Katada, Catal. Sci. Technol. , 3 (2013) 1919.
9. R. Gounder, E. Iglesia, J. Am. Chem. Soc., 131 (2009) 1958.
10. R. Gounder, E. Iglesia, Angew. Chem. Int. Ed., 49 (2010) 808.
11. A. F. H. Wielers, M. Waarkamp, M. F. M. Post, J. Catal. 127 (1991) 51.
12. W. O. Haag, R. M. Dessau, Proc. 8th Int. Congr. Catalysis. Berlin 1984, 2, 305.
13. W. O. Haag, R. M. Dessau, R. M. Lago, Stud. Surf. Sci. Catal. 1991, 60, 255.
14. H. Krannila, W. O. Haag, B. C. Gates, J. Catal. 1992, 135, 115.
15. K. Kubo, H. Iida, S. Namba, A. Igarashi, Micropor. Mesopor. Mater. 149 (2012) 126.
16. N. Katada, T. Kanai, M. Niwa, Micropor. Mesopor. Mater. 75 (2004) 61.
17. E. Lippmaa, A. Samoson and M. Magi, J. Am. Chem. Soc., 108 (1986) 1730.
18. W. Kolodziejski, C. Zicovich-Wilson, C. Corell, J. Perez-Pariente, A. Corma, J. Phys. Chem. 1995, 99, 7002.
19. C. A. Fyfe, Y. Feng, H. Grondey, G. T. Kokotailo, H. Gies, Chem. Rev. 1991, 91, 1525.
20. S. Sklenak, J. Dědeček, C. Li, B. Wichterlova, V. Gabova, M. Sierka, J. Sauer, Angew. Chem. Int. Ed., 46 (2007) 7286.
21. S. Sklenak, J. Dědeček, C. Li, B. Wichterlova, V. Gabova, M. Sierka, J. Sauer, Phys. Chem. Chem. Phys., 11 (2009) 1237.

22. J. Dědeček, D. Kaucký, B. Wichterlová, Chem. Commun., (2001) 970.
23. J. Dědeček, D. Kaucký, B. Wichterlová, O. Gonsiorová, Phys. Chem. Chem. Phys. , 4 (2002) 5406.
24. V. Gábová, J. Dědeček, J. Čejka, Chem. Commun., (2003) 1196.
25. J. Dědeček, Z. Sobalík, B. Wichterlová, Catal. Rev.-Sci. Eng., 54 (2012) 135.
26. J. Dedecek, V. Balgová, V. Pashkova, P. Klein, B. Wichterlová, Chem. Mater., 24 (2012) 3231.
27. A. B. Pinar, C. Márquez-Álvarez, M. Grande-Casas, J. Pérez-Pariente, J. Catal., 263 (2009) 258.
28. C. Márquez-Álvarez, A. B. Pinar, R. García, M. Grande-Casas, J. Pérez-Pariente, Top. Catal., 52 (2009) 1281.
29. Y. Román-Leshkov, M. Moliner, M. E. Davis, J. Phys. Chem. C, 115 (2011) 1096.
30. J. A. Lercher, C. Gru¨ndling, G. Eder-Mirth, Catal. Today, 27 (1996) 353.
31. A. Zecchina, G. Spoto, S. Bordiga, Phys. Chem. Chem. Phys., 7 (2005) 1627.
32. S. Kotrel, M.P. Rosynek, J.H. Lunsford, J. Catal. 191 (2000) 55.
33. J.A. Lercher, R.A. van Santen, H. Vinek, Catal. Lett., 27 (1994) 91.
34. G. J. Kramer, R. A. Van Santen, C. A. Emeis, A. K. Nowak, Nature, 363 (1993) 529.
35. G. J. Kramer , R. A. van Santen, J. Am. Chem. Soc., 117 (1995) 1766.
36. A. Redondo, P. J. Hay, J. Phys. Chem. 97 (1993) 11754.
37. International Zeolite Association, Structure Commission, http://www.iza-structure.org/databases/.

Table 4.1 Physicochemical properties and acid amount of H-ZSM-5 catalysts

Si/Al[a]	**Na/Al**[b]	S_{BET}[c]	S_{EXT}[d]	V_{micro}[e]	**Size**[f]	**Acid amount**[g]	**Al content**
		$m^2\ g^{-1}$	$m^2\ g^{-1}$	$cm^3\ g^{-1}$	mm	mmol g^{-1}	mmol g^{-1}
20	0.0014	415	22	0.18	0.1-1	0.77	0.79
35	n.d.	437	12	0.19	0.1-1	0.45	0.46
52	n.d.	423	15	0.18	0.1-0.8	0.32	0.31
125	n.d.	409	15	0.19	0.5	0.13	0.13
295	n.d.	415	14	0.19	0.6	0.053	0.056
660	n.d.	420	15	0.19	0.8	0.025	0.025

a) Si/Al: atomic ratio of Si/Al in the sample determined by ICP.

b) Na/Al: atomic ratio of Na/Al in the sample determined by AAS.

c) S_{BET}: BET surface.

d) S_{EXT}: External surface area estimated by t-plot method.

e) V_{micro}: Micropore volume estimated by t-plot method.

f) Crystallite size: Determined by SEM.

g) Acid amount: Estimated by the NH_3-TPD.

Table 4.2 Results of CO-IR measurement

Si/Al	ΔOH[a] cm^{-1}	Lewis cm^{-1}	Brønsted cm^{-1}
20	314	2230 (little)	2175
35	315	2230 (little)	2174
52	314	2230 (little)	2175
125	315	n.d.	2175
295	314	n.d.	2175
660	316	n.d.	2174

a) ΔOH increase along with acid strength

Table 4.3 Product distribution and CMR value of H-ZSM-5 with various Al contents at ca 10 % conversion at 623 and 923 K

Temperature	**623 K**					**923 K**					
Si/Al[a]	**20**	**35**	**52**	**125**	**295**	**20**	**35**	**52**	**125**	**295**	**660**
CH_4	0.8	1.4	2.2	3.0	3.8	15.2	14.9	14.5	15.0	15.6	15.8
C_2H_6	4.7	7.6	11.6	15.9	15.2	7.2	7.2	8.1	8.2	8.8	8.7
C_3H_8	35.4	36.3	25.5	18.1	15.5	6.0	6.7	5.5	6.4	7.4	7.8
n-C_4H_{10}	11.1	8.9	5.1	3.8	2.9	0.7	0.7	0.8	0.8	0.9	1.0
i-C_4H_{10}	5.0	3.7	1.0	0.6	0.2	0.3	0.3	0.3	0.3	0.2	0.2
C_2H_4	10.0	8.2	7.4	6.2	6.0	17.8	17.4	15.8	16.6	15.6	16.1
C_3H_6	20.6	22.3	33.5	34.5	36.7	45.9	46.1	47.8	45.5	44.1	42.4
C_4H_8[b]	8.0	8.9	10.1	13.2	13.5	5.0	4.7	5.0	5.2	5.6	6.0
C5+	4.4	2.7	3.6	4.7	6.2	1.9	1.9	2.3	2.1	1.9	2.2
CMR[c]	3.1	4.7	21.2	41.8	125	134	131	128	132	200	210

[a] Si/Al: atomic ratio of Si/Al in the sample determined by ICP.

[b] Total selectivities to butenes

[c] CMR = (C1 +ΣC2)/i-C4 [27]

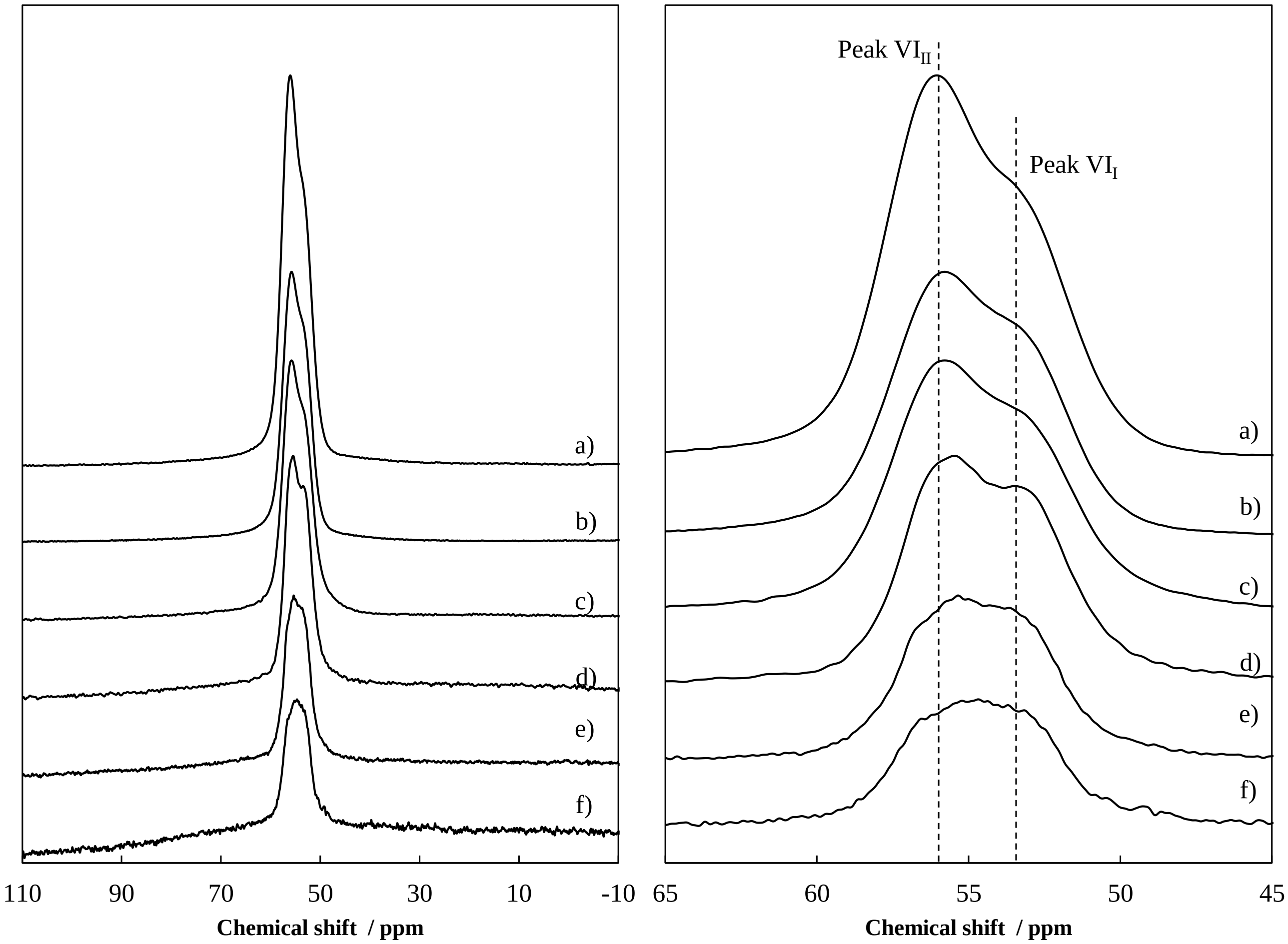

Figure 4.1

^{27}Al MAS NMR spectra of NH_4-ZSM-5 zeolites with various Si/Al ratios: a) 20, b) 35, c) 52, d) 125, e) 295, and f) 660.

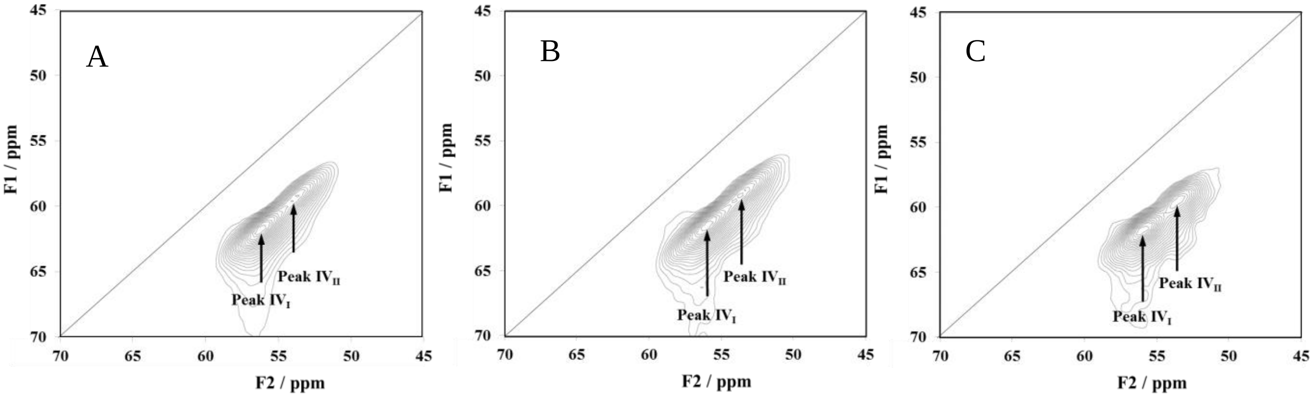

Figure 4.2

^{27}Al MQ MAS NMR spectra of NH$_4$-ZSM-5 zeolites with Si/Al ratio (A) 20, (B) 52 and (C) 125.

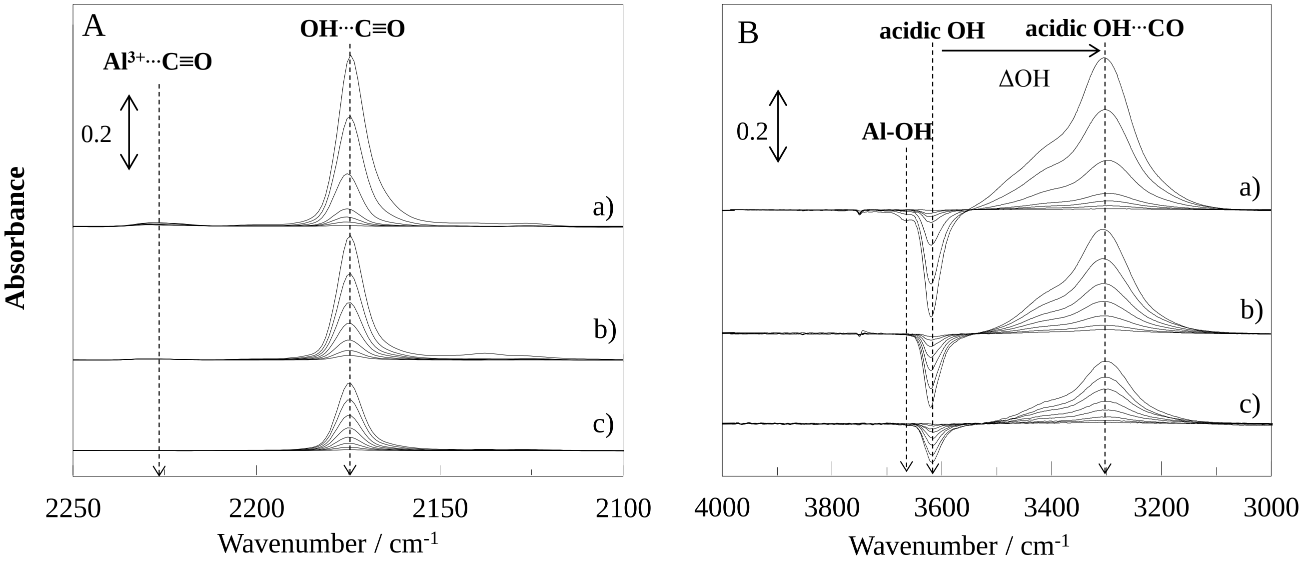

Figure 4.3

Differential FT-IR spectra for CO-adsorbed H-ZSM-5 zeolites with various Si/Al ratios: a) 20, b) 52 and c) 125.

(A) ν(CO) region; (B) ν(OH) region

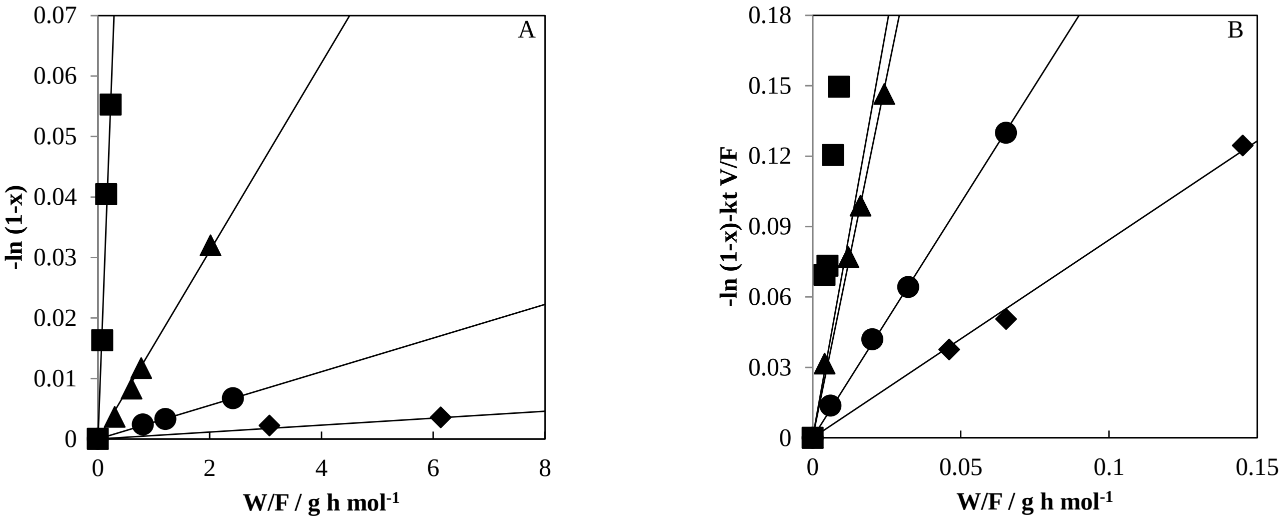

Figure 4.4

Effect of W/F on cracking rate of *n*-hexane over H-ZSM-5 catalysts with various Si/Al ratios: (■) 20, (▲) 52, (●) 125 and (◆) 295.

(A) 623 K (B) 923 K

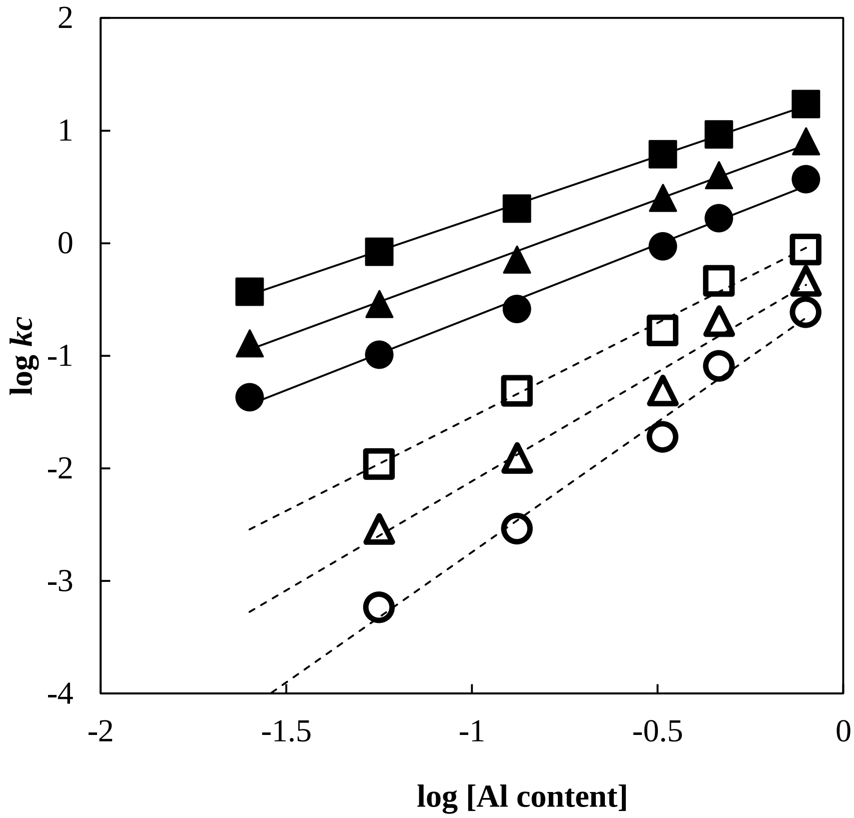

Figure 4.5

Activity as a function of Al content for H-ZSM-5 catalysts at (○) 623 K, (△) 673 K, (□) 723 K, (●) 823 K, (▲) 873 K and (■) 923 K.

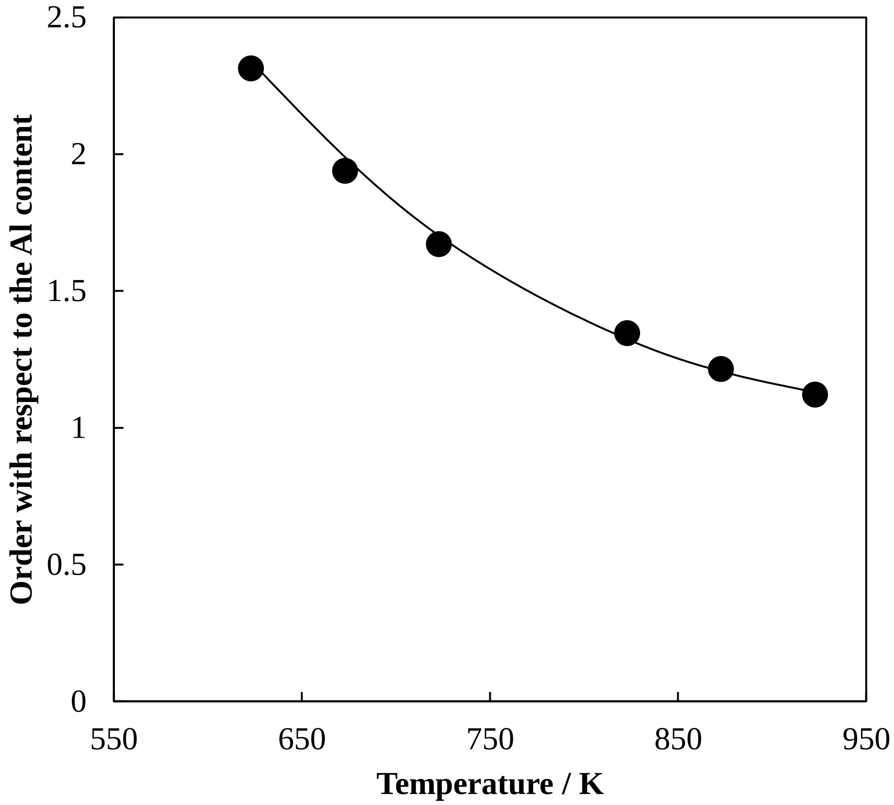

Figure 4.6

Effect of reaction temperature on order with respect to the Al content.

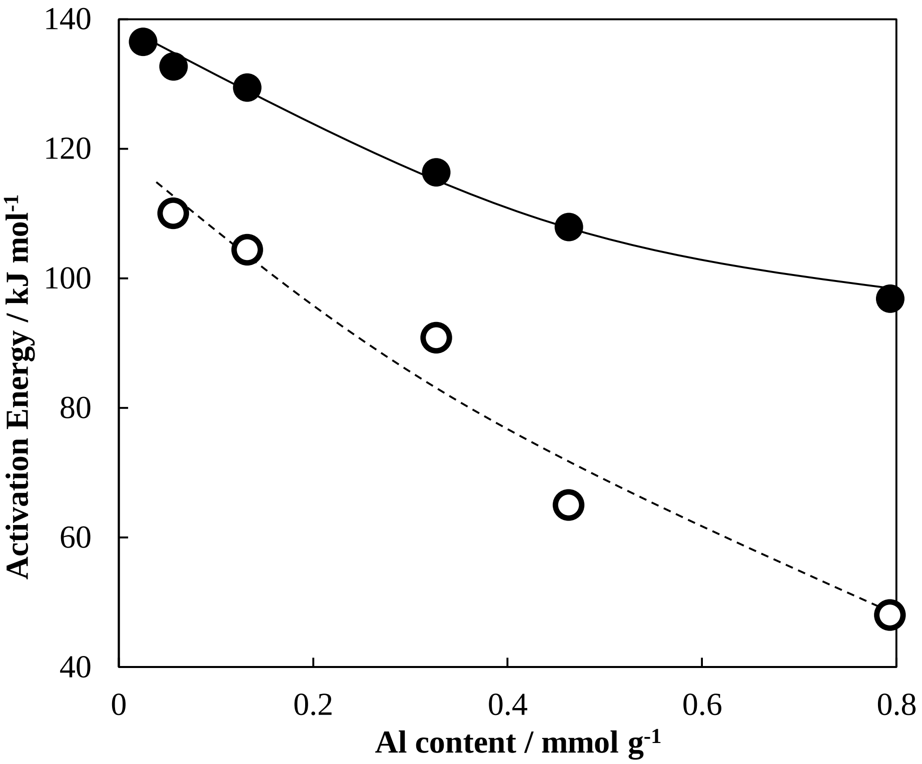

Figure 4.7

Dependence of activation energies for *n*-hexane cracking on the Al content of H-ZSM-5.

(○) Low temperature region, (●) High temperature region

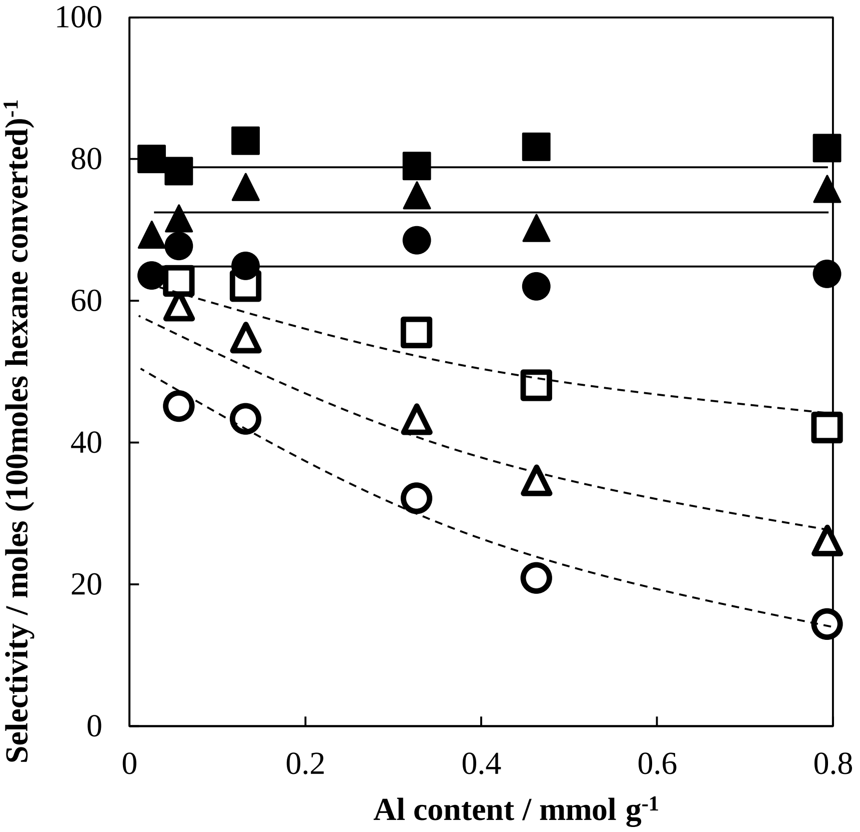

Figure 4.8

Dependence of selectivity to H_2 + CH_4 + C_2H_6 at 10 % conversion on Al content of H-ZSM-5 at (○) 623 K, (△) 673 K, (□) 723 K, (●) 823 K, (▲) 873 K and (■) 923 K.

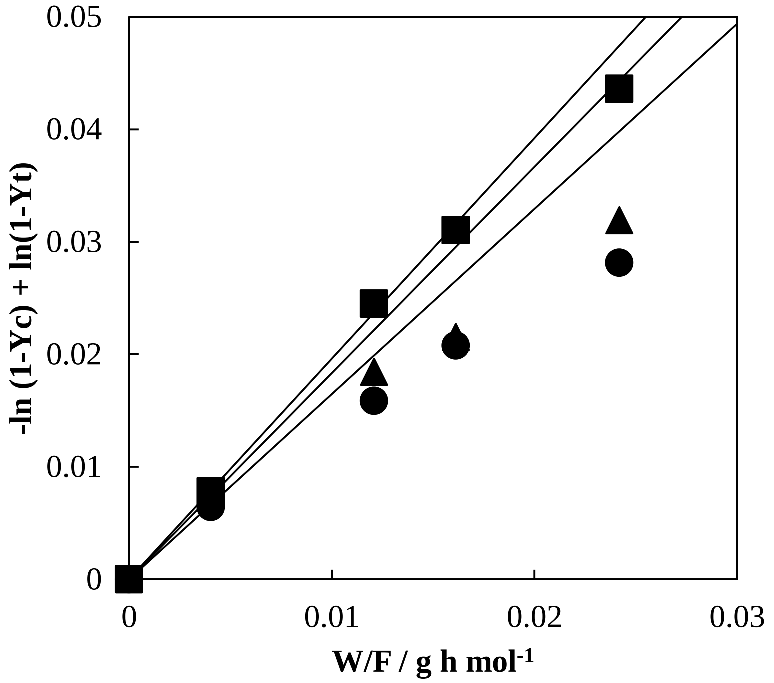

Figure 4.9

Dependence of W/F on formation rate of (■) H_2, (▲) CH_4 and (●) C_2H_6 over H-ZSM-5 at 923 K (Si/Al = 52).

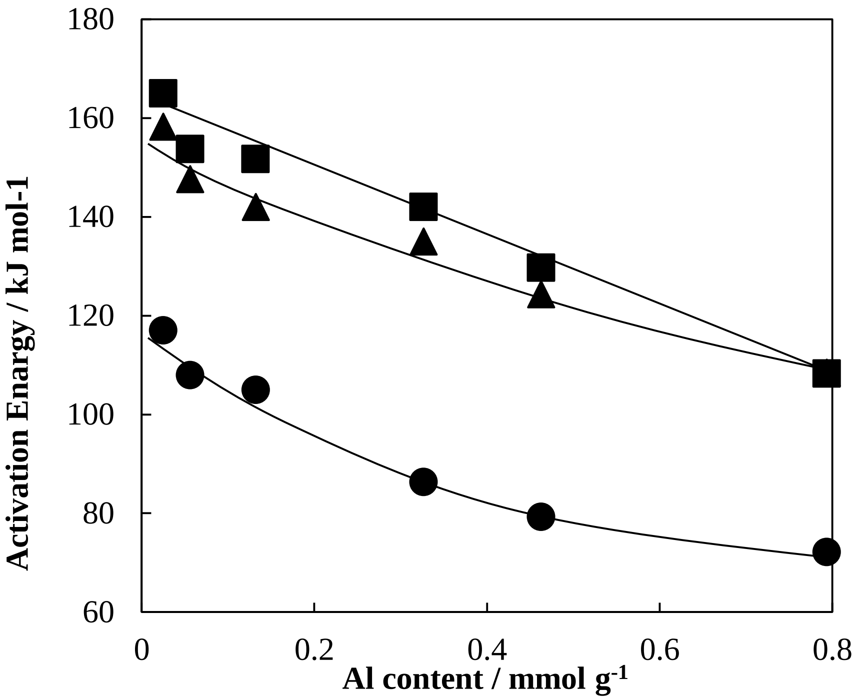

Figure 4.10

Dependence of activation energies for formation of (■) H_2, (▲) CH_4 and (●) C_2H_6 on the Al content of H-ZSM-5.

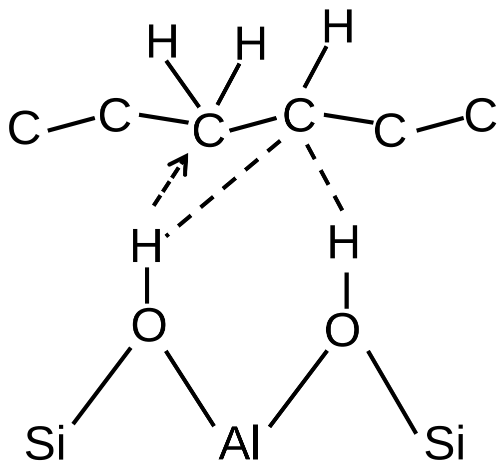

Figure 4.11

The proposed transition states for monomolecular cracking of *n*-hexane on H+ sites in zeolites proposed based on computational studies [33].

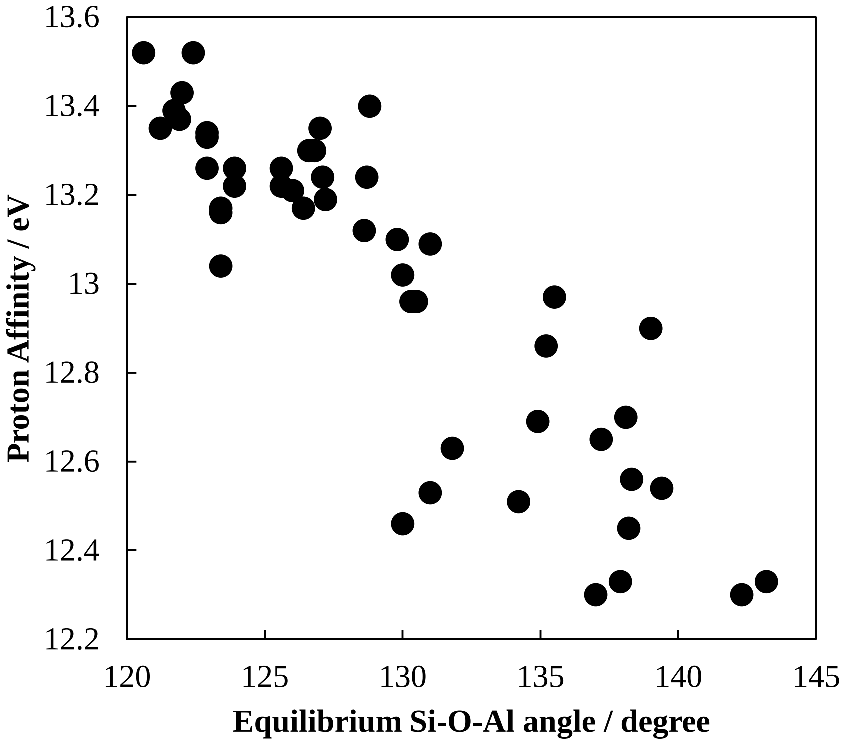

Figure 4.12

Calculated proton affinity vs Al-O-Si equilibrium angle [36].

Chapter 5

Effect of acid site distributions in the pores of H-ZSM-5 zeolites on their catalytic properties

5-1 Abstract

To aim at the development of a new class of ZSM-5 catalyst with the distribution of acid sites in the pores controlled, ZSM-5 zeolites with the **MFI** topology are synthesized using four kinds of organic structure-directing agents (OSDAs) including tetrapropylammonium hydroxide (TPA) cations, dipropylamine, cyclohexylamine and hexamethyleneimine with or without Na cations.

The obtained zeolites synthesized with different OSDAs were characterized by using various techniques in order to investigate the influence of type of OSDAs and presence or absence of Na cations on the Al distribution over twelve distinct tetrahedral sites (T-site). In addition to high resolution ^{27}Al MAS and MQMAS NMR techniques, constraint index (CI) was applied to estimate the distribution of acid sites in the micropore. The acid site distributions are considered based on the difference in the transition-state shape-selectivity through the cracking of *n*-hexane and 3-methylpentane. Furthermore, the relationship between the acid site distributions in the pore of H-ZSM-5 zeolite and the catalytic performance in the cracking of different type of paraffins and conversion of aromatic compounds was examined.

5-2 Introduction

Zeolites are widely used as heterogeneous catalysts in industrial chemical processes, because of their strong acid properties and shape selectivities. The acidic properties of aluminosilicate-type zeolites originate from the presence of protons balancing the negative charge induced by the framework Al in tetrahedral sites (T-sites). The catalytic properties of zeolites depend on many factors such as pore structure, acid strength and acid amounts. In addition these factors, recently, the location and distribution of Al atoms in the zeolite framework has been recognized as an important factor for activity and selectivity, because they would profoundly affect the accessibility of molecules to acid sites and the spatial constraints of the reaction field in the pores [1-4]; however, their control is difficult to achieve. Furthermore, the relationship between Al distribution and the acid strength has not been fully understood. Thus, many zeolite researchers have seriously tackled the estimation of the distribution of framework Al atoms as well as the control of the location of acid sites in the pores.

H-ferrierite with different distributions of acid sites has been synthesized by using different organic structure-directing agents (OSDAs) [2-4]. Davis and co-workers investigated the relationship between the size of cyclic amine used as OSDA and the distribution of acid sites [4]. Very recently, it has reported that the high-resolution ^{27}Al MAS NMR and ^{27}Al MQMAS NMR techniques revealed that the Al distribution over the **RTH**-type framework was clearly dependent on the type of SDA including alkaline cations [5]. The location of the SDA species within the micropores will affect the distribution of Al atoms in the framework because the positive charges of the SDAs are balanced by Al atoms, meaning that the location of acid sites is controlled by rational choice of appropriate SDAs. Thus, this concept should be applicable to the control of acid site location in other zeolites.

Among diverse zeolite catalysts, I have tackled the location and distribution of Al atoms in the **MFI**-type aluminosilicate zeolite (ZSM-5). ZSM-5 zeolite has been widely used as solid acid catalyst in many petrochemical catalytic processes such as cracking, isomerization, aromatization and alkylation processes [6]. In particular, by controlling the location and distribution of Al atoms in the pore, I have aimed to develop the ZSM-5 catalyst that shows a high catalytic performance in the catalytic cracking of naphtha to selectively produce light olefins such as ethylene and propylene, which are important basic raw materials for the petrochemical industry.

The **MFI** structure has crystallographically distinct 12 T-sites and consists of parallel and straight 10-membered ring (MR) channels intersected by sinusoidal 10-MR channels [7]. Although the sizes of both 10-MR are similar to that of the aromatic ring (ca. 5.5 Å), the intersections of these 10-MR have large spherical spaces (diameter ca. 10 Å in diameter). ZSM-5 zeolite with a wide variety of Si/Al ratios ranging from 20 to ∞ has been hydrothermally synthesized with tetrapropylammonium (TPA) cation [8-12]. The TPA cation species are located at the channel intersections with the propyl chains extending into both the straight and sinusoidal channels [9-12]. Thus, it has been assumed that the acid sites in H-ZSM-5 synthesized with TPA cations in the absence of Na cations are selectively located solely at the intersections, and that the acid sites in H-ZSM-5 synthesized with TPA cations and Na cations are located not only at the intersections but also in narrow straight and/or sinusoidal channels. Furthermore, there are many reports that ZSM-5 can be synthesized using various amines and alcohols as OSDAs [13-17]. I have expected that the distributions of acid site in the pores of H-ZSM-5 zeolite can be controlled by the types of OSDAs and alkaline metals used.

The accurate method for the evaluation of the distribution of the acid site in the pores has attract a considerable interest and also been extensively investigated. In this study, the strategy for estimating the distribution of acid sites in the micropore is based on the constraint index (CI), which is defined as the cracking rate of *n*-hexane to that of its isomer 3-methylpentane, and is expressed as follows, Equation (1) [18-21].

$$\mathrm{CI} = k_{n\text{-}hexane} / k_{3\text{-}methylpentane} = \log [1 - X_{n\text{-hexane}}] / \log [1 - X_{3\text{-methylpentane}}] \qquad (1)$$

where $k_{n\text{-}hexane}$ and $k_{3\text{-}methylpentane}$ are the rates of the cracking of *n*-hexane and 3-methylpentane, respectively. Haag and Dessau have reported that the cracking of paraffin proceeds through the "monomolecular cracking" *via* the penta-coordinated carbonium ion and/or the classical "bimolecular cracking" route *via* the carbenium ion/β-scission mechanism involving a hydride transfer reaction [22-24]. In the bimolecular cracking, the transition state of 3-methylpentane is significantly larger than that of *n*-hexane [19].

In general, the reactivity of paraffins with a tertiary carbon atom in the cracking *via* the carbenium ion/β-scission mechanism is higher than that of *n*-paraffins. However, in medium pore (10-MR) zeolites, the Cl value is increased with a decrease in the size of void space [18-21]. This would be because narrow spaces impose more severe steric constraint on the bulky transition state of 3-methylpentane than on that of *n*-hexane. Therefore, it is expected that the H-ZSM-5 zeolite with a larger amount of acid sites in the intersections exhibits a lower CI value, and also that the distributions of acid sites on H-ZSM-5 zeolite should affect catalytic properties for several reactions involving bulky transition states.

Here I report on a new class of ZSM-5 zeolite catalyst with the distribution of acid sites in the pores controlled, which are synthesized by using various OSDAs with or without Na cations. As a control, OSDA-free ZSM-5 was prepared and tested. The distribution of acid sites was evaluated by the CI value as well as ^{27}Al MAS NMR. Finally, thus prepared H-ZSM-5 catalysts are applied for the cracking of other paraffins and the conversion of aromatic compounds to clarify the influence of acid site distributions on the catalytic performance.

5-3 Experimental

5-3-1 Synthesis of calcined silicalite-1 seeds

Nano-sized silicalite-1 was synthesized. The gels with compositions of 1 SiO_2: 0.25 TPAOH: 8.3 were prepared from tetraethyl orthosilicate (TEOS, Tokyo Kasei, >96 %), tetrapropylammonium hydroxide (TPAOH, 40 % aqueous solution, Alfa Aesar). The gels was stirred at 80 ºC for 24 h before crystallization. Crystallization was carried out at 443 K for 24 h. The calcined silicalite-1 was obtained by calcination of the as-synthesized sample in an oven at 823 K to remove TPA cations.

5-3-2 Synthesis of zeolite catalysts

ZSM-5 zeolites were synthesized using four kinds of organic structure-directing agents (OSDAs) including tetrapropylammonium hydroxide (TPA) cations, dipropylamine, cyclohexylamine and hexamethyleneimine with or without Na cations. ZSM-5 zeolites using TPA cation as an OSDA with or without Na cation was synthesized. The gels with two different compositions of 1 SiO_2: 0.01 Al_2O_3: 0.25 TPAOH: 0.1 NaCl: 8.3 H_2O and 1 SiO_2: 0.01 Al_2O_3: 0.5 TPAOH: 8.3 H_2O were prepared from TEOS, TPAOH aqueous solution, aluminium nitrate nonahydrate (Wako, 99.9 %) and sodium chloride (Wako, 99.5 %). The gels were stirred at 80 ºC for 24 h before crystallization. Crystallization of the gels congaing or non-containing Na cations was carried out at 443 K for 3 and 7 days, respectively. ZSM-5 zeolites synthesized by using TPA cation as an OSDA with or without Na cation were denoted by [TPA, Na] and [TPA], respectively.

ZSM-5 zeolites using dipropylamine (DPa, Tokyo Kasei, >99.0 %) and cyclohexlyamine (Cha, Sigma-Aldrich, 99 %) as OSDAs with Na cation were synthesized as follows. The gels with compositions of 1 SiO_2: 0.01 Al_2O_3: 0.4 DPa or Cha: 0.1 Na_2O: 25 H_2O were prepared from colloidal silica (Ludox HS-40, Sigma-Aldrich), DPa or Cha, aluminium nitrate nonahydrate and sodium hydroxide

(Wako, 97 %). The resulting gels were stirred at ambient temperature for 30 min. Then, 5 wt% of the calcined silicalite-1 was added to the mixture as a seed. Thereafter, the prepared mother gel was crystallized in an oven. Crystallization was carried out at 443 K for 2days. ZSM-5 zeolites synthesized by using DPa or Cha as OSDAs with Na cation were denoted by [DPa, Na] and [Cha, Na], respectively.

ZSM-5 zeolites using hexamethyleneimine (HMi, Sigma-Aldrich, 99 %) as OSDAs with Na cation were synthesized as follows. The gel with compositions of 1 SiO_2: 0.01 Al_2O_3: 0.5 HMi: 0.1 Na_2O: 25 H_2O: 0.07H_2SO_4 was prepared from colloidal silica (Ludox HS-40, Sigma-Aldrich), HMi, aluminium nitrate nonahydrate, sodium hydroxide and sulfuric acid (Wako, 95 % +). The resulting gels were stirred at ambient temperature for 30 min. Then, 5 wt% of the calcined silicalite-1 was added to the mixture as a seed. Thereafter, the prepared mother gel was crystallized in an oven. Crystallization was carried out at 433 K for 2days. ZSM-5 zeolites synthesized by using HMi as an OSDA with Na cation were denoted by [HMi, Na].

All of the as-synthesized ZSM-5 zeolites were calcined in an oven at 823 K to remove OSDAs. The NH_4-ZSM-5 zeolites were obtained by ion-exchanging the calcined ZSM-5 zeolites with 1 M NH_4NO_3 aq. at 353 K for 3 h twice.

As a control, NH_4-ZSM-22 and NH_4-ZSM-12 with a Si/Al ratio of ca. 50 were synthesized by hydrothermal synthesis and the following ion exchange using an NH_4NO_3 solution [25]. H-mordenite with a Si/Al ration 45 is a JRC reference catalyst (JRC-Z-HM90).

5-3-3 Characterizations

XRD patterns were collected on a Rint-Ultima III (Rigaku) using a Cu Kα X-ray source (40 kV, 20 mA). Nitrogen adsorption measurements to determine the BET surface area (S_{BET}) and micropore volume (V_{micro}) were conducted at 77 K on a Belsorp-mini II (Bel Japan). S_{EXT} and V_{micro} were estimated by the *t*-plot method. Field-emission scanning electron microscopic (FE-SEM) images of the powder samples were obtained on an S-5200 microscope (Hitachi) operating at 1-30 kV. The sample was mounted on a carbon-coated microgrid (Okenshoji Co.) without any metal coating. Si/Al ratios of the samples were determined by using an inductively coupled plasma-atomic emission spectrometer (ICP-AES, Shimadzu ICPE-9000). Na content of the samples was determined by using atomic absorption spectrometer (AAS, Shimadzu AA-6200). The amount of OSDAs and coke formed during the reaction was determined from the weight loss from 573 to 1073 K in a thermogravimetric (TG) profile, which was performed on a thermogravimetric-differential thermal analyzer (TG-DTA, RigakuThermo plus EVO II). Elemental and chemical analysis data were obtained from vario MACRO cube (Elementar Analysensysteme GmbH).

The high-resolution ^{27}Al MAS NMR and ^{27}Al 3Q MQMAS NMR spectra were obtained on a JEOL ECA-600 spectrometer (14.1 T) equipped with an additional 1 kW power amplifier. For ^{27}Al 3Q MQMAS NMR spectra, pulse durations were 5.5 μs, 2.1 μs and 0.2 ms for the 3Q excitation pulse, the 3Q-1Q conversion pulse and z-filter, respectively. The relaxation delay time was 10 ms. The ^{27}Al chemical shift (δ) was referenced to $AlNH_4(SO_4)_2 \cdot 12H_2O$ at -0.54 ppm and samples were spun at 17 kHz by using a 4 mm ZrO_2 rotor. For high-resolution ^{27}Al MAS NMR spectra at 14.1 T, which were recorded using a single pulse, the pulse width was set at 0.1 μs and 10000 scans were accumulated at a sample spinning rate of 17 kHz. A 10 ms relaxation delay was determined so as to be long enough to permit quantitative analysis of zeolite samples. $AlNH_4(SO_4)_2 \cdot 12H_2O$ was also used as a reference for the ^{27}Al chemical shift.

Temperature-programmed ammonia desorption (NH_3-TPD) profiles were recorded on a Multitrack TPD equipment (Japan BEL). Typically, 30 mg catalyst was pretreated at 923 K in He (50 mL min^{-1}) for 1 h and then cooled to 423 K. Prior to the adsorption of NH_3, the sample was evacuated at 423 K for 1 h. Approximately 2500 Pa of NH_3 was allowed to make contact with the sample at 423 K for 10 min. Subsequently, the sample was evacuated to remove weakly adsorbed NH_3 at the same temperature for 30 min. Finally, the sample was cooled to 423 K and heated from 423 to 1073 K at a ramping rate of 10 K min^{-1} in a He flow (50 mL min^{-1}). A mass spectrometer was used to monitor desorbed NH_3 (m/e = 16). The amount of acid sites was determined by using the area in the profiles.

Spectra of Fourier transform infrared spectroscopy (FT-IR) were obtained at a resolution of 4 cm^{-1} using a Jasco 4100 FTIR spectrometer equipped with a mercury cadmium telluride (MCT) detector. A total of 64 scans were averaged for each spectrum. IR spectra of the clean disk were recorded in vacuo at 153 K to obtain background spectra. The sample was pressed into a self-supporting disk (20 mm diameter, 30 - 60 mg) and placed in an IR cell attached to a conventional closed-gas circulation system. The sample was pretreated by evacuation at 773 K, followed by adsorption of 2-30 Pa CO at 153 K. Then, the sample was evacuated at the same temperature for 30 min. The spectra were recorded at 153 K.

5-3-4 Reaction procedure

Catalytic reactions were performed by using a fixed-bed reactor equipped with an on-line gas-chromatograph. The catalytic reactions were carried out in a 6 mm quartz tubular flow microreactor loaded with 10 to 200 mg of 50/80 mesh zeolite pellets without a binder. The catalyst was centered at the reactor in a furnace. Argon was used as a carrier gas. The hydrocarbon products were analyzed with an on-line gas chromatograph (Shimadzu GC-2014) with an FID detector. Hydrogen was analyzed by a gas chromatograph (Shimadzu, GC-2014) with a TCD detector.

The constraint index test were carried out at 673 K by using single-component feeds in order to unambiguously assess the true ratio of the rates of *n*-hexane (Sigma-Aldrich, >99.0 %) and 3-methylpentane (Tokyo Kasei, >99.0 %) cracking. The catalyst was activated in flowing Argon at 823 K for 1 h prior to the reaction, and then cooled to the desired reaction temperatures. The initial partial pressure of C6 paraffins was set at 40 kPa. The W/F (W: amount of catalyst /g, F: total flow rate /mol h^{-1}) was adjusted to obtain 15 -20 % of the *n*-hexane conversion and the cracking of 3-methylpentane was carried out under same conditions in *n*-hexane cracking. The selectivities and the yields were expressed as mol% defined as (mol number of each individual product) / (mol number of C6 paraffins reacted).

The cracking of 1,3,5-triisopropylbenzene (1,3,5-TIPB, Tokyo Kasei, 95.0%) was carried out at 673 K. The catalyst was activated in flowing Argon at 823 K for 1 h prior to the reaction, and then cooled to the desired reaction temperatures. The initial partial pressure of 1,3,5-TIPB was set at 0.5 kPa. The W/F was 0.2 g h mol_{total}^{-1}. The cracking was carried out in the presence or absence of 2,4-dimethylquinoline (2,4-DMQ, Tokyo Kasei, >95.0 %) to poison selectively the acid sites on the external surfaces [26].

The cracking of C6 paraffins (*n*-hexane, 3-methypentane, 2,3-dimethylbutane (Tokyo Kasei, >99.0 %) and 2,2-dimethylbutane (Tokyo Kasei, >99.0 %)) was carried out at 623-673 K. The catalyst was activated in flowing Argon at 823 K for 1 h prior to the reaction, and then cooled to the desired reaction temperatures. The initial partial pressure of C6 paraffins was set at 40 kPa. The W/F was adjusted to obtain < 20 % of the C6 paraffin conversion. The cracking was carried out in the presence of 2,4-DMQ. The selectivities and the yields were expressed as mol% defined as (mol number of each individual product) / (mol number of C6 paraffins reacted). The paraffin conversion follows a first-order kinetic model. From the slopes of First-order kinetics plot, the reaction rate constant were calculated [27].

The cracking reactions of *n*-hexane and methylcyclohexane (Tokyo Kasei, >99.0 %) were carried out at 923 K. The catalyst was activated in flowing Argon at 923 K for 1 h prior to the reaction and following reaction at same temperature. The initial partial pressure of paraffins was set at 40 kPa and the W/F was 2.7 g-cat h mol_{total}^{-1}. The yields were expressed as mol % calculated based on mol number of products (mol number of each individual product) divided by (mol number of reactant fed).

The amount of coke formed during the reaction was determined from the weight loss from 673 to 1073 K in a thermogravimetric (TG) profile, which was performed on a thermogravimetric - differential thermal analyser (TG-DTA, Rigaku Thermo plus EVO II)

The conversion of toluene and *m*-xylene was carried out at 573-648 K. The catalyst was activated in flowing Argon at 823 K for 1 h prior to the reaction, and then cooled to the desired reaction temperatures. The initial partial pressure of aromatic compound was set at 20 kPa. In toluene conversion, the W/F was adjusted to obtain < 3 % of the toluene conversion. In *m*-xylene conversion, the W/F was adjusted to obtain < 35 % of the *m*-xylene conversion. The reactions were carried out in the presence of 2,4-DMQ. The yields were expressed as mol % calculated based on the mol number of product. (mol number of each individual product) divided by (mol number of reactant fed). In toluene conversion, the reaction rate calculate from dependence of W/F on conversion under differential reaction conditions In *m*-xylene conversion, the reaction rate constant were calculated form the dependence slopes of First-order kinetics plot. [28].

5-4 Results and discussion

5-4-1 Synthesis and physicochemical properties of H-ZSM-5

The XRD patterns of the products synthesized with various OSDAs are shown in Fig. 5.1, indicating that all of the samples were identified as the **MFI** structure with a high crystallinity. The FE-SEM images (in Fig. 5.2) revealed that the crystallite sizes of [TPA] and [TPA, Na] were ca. 100 nm regardless of with or without Na cations. The crystallite size of [HMi, Na] as an OSDA were 200 - 300 nm. On the other hand, larger sized crystals were formed when DPa and Cha were used as OSDAs and the crystallite size of these products was ca. 500 - 800 nm.

The Al contents determined by ICP analysis were 0.31-0.38 mmol/g for all of the samples (Table 5.1), being close to those of their synthesis gels. It was confirmed by the AAS measurements that the as-synthesized [TPA] sample did not contain Na species; the negative charges of Al atom in the zeolite framework are balanced by only TPA cations. On the other hand, the amount of Na specie in other samples synthesized with Na cationswas lower than that of Al atoms, indicating that the negative charges of Al atom re balanced by OSDAs in addition to Na cations.

The OSDAs contents of the as-made samples are summarized in Table 5.1. The C/N atomic ratios, calculated from the CHN elemental analysis, for [TPA], [TPA, Na] [DPa, Na] [Cha, Na] and [HMi, Na) are 12.3, 12.3, 6.0, 6.2 and 6.1, respectively, being similar to the C/N ratios for these molecules (12 for TPA and 6 for the others). By the ^{13}C CP MAS NMR spectra of the as-synthesized samples, the molecular structures of all of the OSDAs are completely retained (Fig. 5.3). Considering the size of intersection of the **MFI**-structure (ca. 9 Å in diameter), the OSDA molecule used would be located in the micropores with its molecular structure intact.

Based on the TG-DTA and CHN elemental analyses, the numbers of the OSDA molecule per unit cell of the **MFI**-structure are estimated at approximately 4.2, 4.1, 4.6, 3.5 and 6.5 for [TPA], [TPA, Na], [DPa, Na], [Cha, Na] and [HMi, Na], respectively. Considering that one unit cell consists of four intersections, all of the intersection are fully occupied by the OSDA molecules. By the ^{27}Al MAS NMR spectra (Fig. 5.4), all of the the Al species in solid are in the framework irrespective of the samples. Hence, the amounts of Al atom per unit cell contents were calculated to be 1.8 - 2.2. For Na cation, it was calculated to be A-B. These results indicate that the total contents of OSDAs and Na cations are higher than that of Al atoms, and that the positive charges introduced by the OSDAs and Na cations would be balanced by structural defects, namely silanol groups as well as Al atoms.

The physicochemical properties of H-ZSM-5 samples are listed in Table 5.2. The N_2 adsorption and desorption isotherms for all of the H-ZSM-5 zeolites exhibited a typical isotherm of microporous materials with a plateau at high relative pressures (type I, IUPAC). The BET surface area (S_{BET}) and the external surface area (S_{EXT}) of [TPA], [TPA, Na] and [HMi, Na] were larger than those of [DPa, Na] and [Cha, Na]. The micropore volume (V_{micro}) was almost the same (ca. 0.16 - 0.18 cm^3 g^{-1}) and the internal (micropore) surface areas, which are defined as the difference between S_{BET} and S_{EXT}, are similar for all the products (ca. 380 - 400 m^2/g). These results indicated that the prepared H-ZSM-5 samples have similar structural qualities. The acid amounts estimated by NH_3-TPD measurement are dependent on the Al content, and are nearly consistent with the amount of Al content in the bulk, which was determined by ICP analysis. These results suggest that all of the Al atoms incorporated work as acid sites in most of the samples and any dealumination hardly occurred during the preparation.

5-4-2 Al state in framework and acid properties

The state of Al atoms in the framework was examined by ^{27}Al NMR techniques. Figure 5.4 shows the ^{27}Al MAS NMR spectra of a series of the NH_4-ZSM-5 zeolites synthesized using various OSDAs with or without Na cations. The NMR spectra of ZSM-5 zeolites exhibited a high peak at ca. 55 ppm, which are assigned to tetrahedrally coordinated Al in the framework. The peak at 0 ppm assigned to octahedral coordinated Al atom was not observed in all of the samples; there are no extra framework Al atom in these samples.

The resolution of ^{27}Al MAS NMR spectra is not high enough to detailedly characterize Al species because a quadrupolar interaction at Al (I = 5/2) leads to a broadening of the peak; the sizable second-order quadrupolar interaction at Al, which contains higher-rank anisotropic terms, cannot be completely averaged out by MAS [30-32]. Thus, ^{27}Al MQMAS NMR was applied to characterize the state of Al atoms in the **MFI** framework. For all samples, only tetrahedrally coordinated Al atoms were observed in the MQMAS spectra, showing isotropic distributions as a result of variations in Al–O–Si bond angle [33]. The ^{27}Al MQMAS NMR spectrum of [TPA] is shown in Figure 5.5 (A), indicating that two cross-sections were clearly observed. The isotropic projection in the F1 dimension gives a 1D high resolution spectrum of Al without quadrupolar second-order broadening. Figure 5.5 (B) shows the ^{27}Al MQMAS F1 projections of the NH_3-ZSM-5 zeolites. In all of the spectra, the peaks assigned to tetrahedrally coordinated Al atom consist of at least two different peaks, suggesting that all of the samples have at least two crystallographically distinct Al sites in the framework. The ZSM-5 zeolites synthesized with various OSDAs with or without Na cations gave different proportions of each peak, implying that the Al distribution over twelve distinct T-site of **MFI** structure depends on the type of OSDAs and/or the presence Na cations.

In the **MFI**-type zeolite, there are ten T-sites facing to intersection in the **MFI** framework, while only two T-sites (T4 and T10 sites) do not face to the intersection [7], and they are located in the sinusoidal channel. It is reported that the peak assigned to the Al atoms in the T4 site is observed in right peak group, while the peak assigned to the Al atoms in the T10 site is observed in left peak group [34]. The Brønsted acid site is formed on an O atom in the vicinity of the tetrahedral Al atom in the framework. Therefore, there are forty eight types of crystallographically distinct O atoms exist; forty eight types of Brønsted acid site are structurally possible, meaning that the attribution of each peak and cross-section in the ^{27}Al MAS and MQMAS NMR spectrua to a specific T site would not be achieved by only the NMR techniques.

In-situ FT-IR spectroscopy was applied to the evaluation of the acidic property using CO as a probe molecule. The acidic properties of the H-ZSM-5 zeolites obtained using various OSDAs with similar Al contents, but different Al distributions were investigated by *in-situ* FT-IR using CO as a probe molecule. The advantages of CO as probe are its very weak basicity compared with pyridine and ammonia, which are generally used as probe molecules for estimation of acidic properties and high sensitivity of the IR band frequency to the strength of the acid sites [35, 36].

Difference FT-IR spectra for CO-adsorbed H-ZSM-5 zeolites are shown in Fig. 5.6. In the spectra of the ν(CO) region (Fig. 5.6 (B)), the strong band at 2175 cm^{-1}, which corresponds to the stretching mode of ν(C≡O) on Brønsted acid site [35, 36] was observed in the all of the samples. Note that the band at 2230 cm^{-1}, which corresponds to the stretching mode of ν(C≡O) on Lewis acid site, was hardly observed. Therefore, the H-ZSM-5 zeolites prepared have predominantly Brønsted sites and have an extremely low concentration of Lewis sites.

In general, the band of acidic OH groups was shifted from 3620 to 3306 cm^{-1} due to the interaction of CO with acidic OH groups, and this shift is related to the acid strength [35, 36]. In my case, the difference of ΔOH was not observed in these H-ZSM-5 zeolites (Fig. 5.6 (A)), suggesting that the strength of Brønsted acidity of these H-ZSM-5 zeolites are almost the same.

5-4-3 Constraint index of various zeolites

In this study, "constraint index (CI)" was applied to estimate the distribution of acid sites in the micropore. First, I evaluated the CI value of the zeolites with the **TON**, **MFI**, **MTW** and **MOR** topologies. H-ZSM-22 with the **TON** topology and H-ZSM-12 with the **MTW** topology have 10- and 12-MR 1-dimensional straight channels without a large cavity, respectively. H-mordenite with the **MOR** topology has 12-MR straight channels and 8-MR side-pockets [7]. From XRD patterns, all of the samples were identified as zeolites with their own crystal phases with a high crystallinity (Fig. 5.7. The Si/Al molar ratio of these zeolites was around 50 and the amount of acid sites estimated from NH_3-TPD was almost similar to the Al contents (Table 5.3).

In the cracking of *n*-hexane (*n*-Hx) and 3-methylpentane (3-MP), the amount of catalysts and the total flow rate of reaction gas (W/F) were adjusted to obtain 15 - 20% of *n*-hexane conversion. Figure 5.8 shows the CI values for these zeolites at the reaction temperature of 673 K, indicating that the CI value is strongly dependent on the structure of the zeolite. Except for [TPA], the CI values are in good agreement with those reported in literature [18-21]. The CI values are decreased with an increase in the size of the pore. In the bimolecular cracking, hydrogen and hydrocarbons below C3 are scarcely formed, because these products are only formed through energetically unfavorable primary carbenium ions. In contrast, in the monomolecular cracking, a penta-coordinated carbonium ion formed by the protonation of paraffins decomposes into a carbenium ion and hydrogen or lower paraffins containing methane and ethane (scheme 1). Hence, the total selectivity to methane, ethane and hydrogen can be regarded as a parameter of the contribution of the monomolecular cracking [22, 37]. The total selectivities to these molecules are listed in Table 5.4. The total selectivity to these molecules in 3-methylpentane cracking was decreased with an increase in the size of the pore, suggesting that the bimolecular cracking of 3-methylpentane *via* a bulky transition state proceeds more easily in a wider reaction space. In the cracking of 3-methylpentane, the bimolecular cracking hardly occurred over H-ZSM-22, which has one-dimensional 10-MR straight channels.

Note that the CI value for [TPA] was remarkably smaller than that for [TPA, Na] although their structures are identical. These two H-ZSM-5 zeolites have similar crystallite size and S_{EXT}. Therefore, the difference in the CI value between the two H-ZSM-5 zeolites are not caused by the diffusional restriction of 3-methylpentane and acid sites on the external surface. Additionally, CO-adsorbed FT-IR analysis revealed that the acid strength of the Brønsted acid sites in both samples is quite similar. From these experimental facts, it is concluded that the observed difference in the CI values between the [TPA, Na] and [TPA] catalysts would be caused by the difference in the distribution of acid sites, which would be influenced by TPA cations and Na cations.

5-4-4 C6 paraffin cracking over various H-ZSM-5 zeolites

In general, the monomolecular cracking requires a higher activation energy than the bimolecular cracking [23, 24]. Therefore, to clarify the reaction mechanism of the cracking of *n*-hexane and 3-methylpentane over H-ZSM-5 zeolites, the activation energy and product distributions were examined. In order to selectively poison the acid sites on the external surfaces of ZSM-5, the zeolites were treated with 2,4-DMQ because its size is too large to enter the 10MR channels of ZSM-5 [26]. The complete poisoning of the acid sites on the external surface was confirmed by the cracking of 1,3,5-triisopropylbenzene (1,3,5-TIPB), which is too large to enter the pore of H-ZSM-5 and will be cracked only by the acid site on the external surface [38]. H-ZSM-5 poisoned with 2,4-DMQ were completely inactive for the 1,3,5-TEPB cracking, indicating the complete poisoning of external surface (Fig. 5.9).

The Arrhenius plots for the cracking of *n*-hexane and 3-methylpentane over the [TPA, Na] and [TPA] samples from 623 to 673 K are shown in Fig. 5.10. In the cracking of *n*-hexane, the reaction rate constant and activation energy were almost the same; activation energies of [TPA] and [TPA, Na] were estimated at 66.3 and 65.7 kJ mol^{-1}, respectively. Additionally, the total selectivity to hydrogen, methane and ethane at 10 % of the conversion between the two H-ZSM-5 samples were almost the same (ca. 13 mol%). Therefore, the apparent activation energy should vary with the ratio between the two mechanisms. These results suggest that the ratio of the monomolecular cracking to the bimolecular cracking is not drastically changed and that the bimolecular cracking mechanism is predominant. In contrast, in the cracking of 3-methylpentane, the activation energy for [TPA] was about half of that for [TPA, Na]. In addition, the total selectivity to hydrogen, methane and ethane over [TPA, Na] (56.4 mol%) was much higher than that over [TPA] (31.3 mol%). Thus, the bimolecular cracking proceeds predominantly over [TPA] unlike over [TPA, Na].

In the cracking of 3-methylpentane over H-ZSM-22, the bimolecular cracking was not observed (Table 5.4). This result strongly suggests that the cracking of 3-methylpentane over acid sites located at straight or sinusoidal channels of H-ZSM-5 proceeds solely *via* the monomolecular cracking mechanism. The spaces of straight and sinusoidal channels of the **MFI** sturcure are too small to accommodate the bimolecular transition state consisting of 3-methylpentane and carbenium ions. In contrast, the intersections are large enough to cause the bimolecular reaction, which occurs predominantly. Therefore, it is considered that the most of the acid sites of [TPA] are located at the intersections.

The relationship between activation energy and total selectivity to hydrogen, methane and ethane at 10 % of the conversion for cracking of *n*-hexane and 3-methylpentane over various H-ZSM-5 samples are shown in Fig. 5.11. In the cracking of *n*-hexane, the cracking activation energy and total selectivity among these H-ZSM-5 samples were almost the same. In contrast, in the cracking of 3-methylpentane, the activation energy was different and there is a positive correlation between activation energy and total selectivity. Haag and co-workers have reported that crystallite size does not affect the activity in both the cracking of *n*-hexane and 3-methylpentane over H-ZSM-5 at conventional cracking temperatures (600-800 K) [19]. Therefore, the differences in the activation energy and total selectivity in 3-methylpentane cracking among H-ZSM-5 zeolites are not caused by the diffusional restriction of 3-methylpentane. Thus, these differences in the behaviors for the 3-methylpentane cracking over the H-ZSM-5 catalysts should be caused by the difference in the distribution of acid sites in the pores. These findings give us an insight that the type of OSDAs and the presence or absence of alkaline cations during crystallization clearly affects the distribution of acid sites of H-ZSM-5. In the present study, ZSM-5 zeolites were synthesized using various OSDAs with Na cations except for [TPA]. Therefore, it is difficult to clarify the detail influence of type of amines on acid site distributions in the H-ZSM-5. However, if ZSM-5 zeolites can be synthesized using various OSDAs without using Na cations, it is possible to clarify the detail location of OSDAs. It is noteworthy that [TPA] exhibited the lowest activation energy and the lowest total selectivity to hydrogen, methane and ethane in 3-methylpentane cracking. These findings indicated that the bimolecular cracking proceeds more predominantly over [TPA] than over the other H-ZSM-5 samples. Thus, it is considered that the acid sites in [TPA] are selectively located solely at the intersections because the negative charges of Al atoms in the **MFI** framework are balanced by large TPA cations that located in the intersections during the crystallization of the ZSM-5.

Furthermore, to clarify the influence of the distribution of acid sites on the cracking of dimethylbutanes, the cracking behaviors over [TPA] and [TPA, Na] were investigated (Table 5.5). The reaction rate constants for deimethylbutans cracking were significantly lower than that of *n*-hexane cracking. It is because the diffusional resistance of dimethylbutanes is significantly higher than that of *n*-hexane and 3-methylpentane. In the cracking of 2,2-dimethylbutane (2,2-DMB), there is no marked differences in the cracking rate constant at 623 K and activation energy between [TPA] and [TPA, Na]. In contrast, in the cracking of 2,3-dimethylbutane (2,3-DMB), the cracking rate constant and activation energy were significantly different between [TPA] and [TPA, Na]. Additionally, like the cracking of 3-methylpentane, the total selectivity in the 2,3-DMB cracking over [TPA, Na] was much higher than that over [TPA]. Therefore, these differences should be caused by the difference in the distribution of acid sites in the pores. The bimolecular cracking of 2,3-DMB *via* bulky transition states would proceed more easily over [TPA] than over [TPA, Na]. Moreover the total selectivity for both catalysts was increased with an increase in bulkiness of the reactant. Thus, the bimolecular cracking of *n*-hexane over [TPA] proceeds with a similar rate to that over [TPA, Na], but that of 3-MP and 2,3-DMB over [TPA] proceeds more predominantly than over [TPA, Na]. In the 2,2-DMB cracking over both catalysts, the total selectivities reached at almost 100 %. This finding indicates that the cracking proceeds solely via the monomolecular cracking, because the size of the transition state of 2,2-DMB in the bimolecular cracking is too large to form even in intersections.

5-4-5 Influence of acid site distributions in H-ZSM-5 pores on conversion of aromatic compounds

The disproportionation and the alkylation of toluene and the *m*-xylene isomerization over 10MR zeolites, which are important reactions to produce the *p*-xylene, are used for the production of intermediate for polymer production. The H-ZSM-5 catalysts with the size of pore opening controlled by the modification with coke, SiO_2, P, B and Mg [39-43] have been good catalysts for *p*-xylene production because the kinetic diameters of the *p*-toluene is very close to the 10-MR pores of the **MFI**-type zeolite. Additionally, the disproportionation of aromatic compounds, especially *m*-xylene has been used as a test reaction to investigate the size of reaction space in zeolites [44]. In this study, the influence of the distribution of acid sitein the pore of H-ZSM-5 zeolite on the conversions of toluene and *m*-xylene was examined.

Figure 5.12 shows the results of the toluene conversion over [TPA] and [TPA, Na] at 623 K. The reaction rate of [TPA] was higher than that of [TPA, Na] as shown Fig. 5.12 (A). Figure 5.12 (B) shows the change in the yields of xylene and benzene along with the W/F, indicating that the formation rate of xylene and benzene over [TPA] and [TPA, Na] are also different, and that the benzene/xylene molars ratios are almost the same (ca. 1.1). . These findings clearly indicated that toluene disproportionation is predominant compared to the alkylation of toluene. It has been reported that the disproportionation of toluene over H-ZSM-5 zeolite proceeds via bulky diphenylmethane-like transition states [44]. Thus, it is considered that the disproportionation of toluene via bulky transition states would proceed more easily over acid sites in intersections than over those in narrow channels. This is the reason why [TPA] exhibited a higher catalytic performance than [TPA,Na]

In contrast, the overall reaction rates for *m*-xylene conversion for [TPA] and [TPA, Na] were almost the same as shown Fig. 5.13 (A). In *m*-xylene conversion, large amount of xylene isomers and significantly small amount of toluene (and 1,2,4-trimethylbenzene) were formed (Fig. 5.13 (B)). From these results, the isomerization proceeds simultaneously with the disproportionation in *m*-xylene conversion and the rate of isomerization is significantly faster than that of disproportionation over H-ZSM-5 zeolites. It is noteworthy that the rate of disproportionation of *m*-xylene over [TPA] was faster than that that over [TPA, Na] like toluene disproportionation. On the other hand, there is no marked difference in the reaction rate of *m*-xylene isomerization between [TPA] and [TPA, Na]. It is because xylene isomerization proceeds via the monomolecular reaction and therefore, the isomerization of xylene should proceed in the absence of steric constraint [45, 46]. Thus, the isomerization is not affected by acid site distributions in the pores.

Furthermore, the activation energies of [TPA] and [TPA, Na] for the toluene and *m*-xylene conversion were considered. The Arrhenius plots for the toluene and *m*-xylene conversion over the [TPA, Na] and [TPA] samples ranging from 573 to 648 K are shown in Fig. 5.14. In the *m*-xylene conversion, there are no marked differences in the reaction rate constant at each reaction temperature and activation energy between [TPA and [TPA, Na]; activation energies of [TPA] and [TPA, Na] were 30.2 and 28.6 kJ mol^{-1}, respectively. This is because the isomerization that proceeds in absence of steric hindrance is predominantly. On the other hand, in the toluene conversion, [TPA] exhibited a smaller activation energy than [TPA, Na]; activation energies of [TPA] and [TPA, Na] were 60.0 and 78.9 kJ mol^{-1}, respectively. These findings indicated that the disproportionation of toluene proceeds via bulky transition state not only on the acid sites in intersections but also on those in narrow space of straight and sinusoidal channels. The disproportionation of toluene via bulky transition states over acid sites located in the intersections should proceed with a lower activation energy than that over acid site located at narrow space, resulting in the different overall activation energies of [TPA] and [TPA, Na] .

It is concluded that the acid site distributions in the pores of H-ZSM-5 zeolite affect the several reactions via bulky transition states such as bimolecular cracking of *iso*-hexanes, disproportionation of aromatic compounds.

5-4-6 Influence of acid site distributions in H-ZSM-5 pores on the cracking of *n*-hexane and methylcyclohexane

Light olefins, such as ethylene, propylene and butenes, are important basic raw materials for the petrochemical industry. The catalytic cracking of naphtha over acidic zeolite catalysts may be a promising alternative to produce the light olefins [47, 48]. Among various zeolites, ZSM-5 with the **MFI** structure has been recognized as a prime candidate for the practical catalytic cracking, because of its high thermal and hydrothermal stabilities and its considerably high resistance to deactivation by coking as well as its strong acidity [49-57]. However, zeolites are generally subject to deactivation mainly due to pore blocking by coke formed during the cracking. The clarification of the influence acid sites distribution on the deactivation in the naphtha cracking has been strongly desired in order to design of good catalysts for this process. Therefore, the influence of the acid site distributions of H-ZSM-5 zeolite on the deactivation for the cracking of *n*-hexane and methylcyclohexane, which are constituents of naphtha, was examined.

The change in the conversions of *n*-hexane and methylcyclohexane over [TPA] and [TPA, Na] along with time-on-stream (TOS) was examined under a higher initial pressure of hydrocarbons of 40 kPa and at high temperature (923 K), which should result in a faster deactivation. There are no marked difference in the reaction rate constants for *n*-hexane and methylcyclohexane cracking at 923 K between [TPA] and [TPA, Na] (Table 5.6). Figure 5.15 shows the results of *n*-hexane cracking over [TPA] and [TPA, Na]. The initial conversion of *n*-hexane on both catalysts was ca. 100 % as shown in Figs. 5.15 (A, B) and the conversions were decreased along with TOS. The deactivation rate and the change in the product distributions were almost the same on [TPA] and [TPA, Na]. Figures 5.15 (C, B) shows the amount of deposited coke during reaction and the decrease in the micropore volume due to coke formation, respectively. The coke formation rates were almost the same in both catalysts. The degree in the decrease in the micropore volume was also the same; the micropore volumes of [TPA,Na] and [TPA] after the TOS of 25 h were found to be 0.09 and 0.07 cm^3 g^{-1}, respectively. These findings imply that the deactivation for *n*-hexane cracking over H-ZSM-5 zeolite is not drastically affected by acid site distributions. Note that it is revealed by ^{27}Al MAS NMR that the change in the Al conditions, e.g., dealumination, hardly occurred in both catalysts during the reaction. Therefore, thus observed deactivation is caused by coking.

In *n*-hexane cracking, the deactivation rate and the decrease in the micropore volume of the nano-sized H-ZSM-5 catalysts were smaller than those of the macro-sized catalysts, and that the coke is mainly deposited on the external surface of the nano-sized H-ZSM-5 due to their shorter average diffusion path lengths [ref.]. Considering that the crystallite sizes of [TPA] and [TPA, Na] are less than ca. 100 nm, the reactant and products involving coke precursors may easily diffuse out from the pores regardless of acid site distributions. As a result, the coke was mainly deposited on the external surface of the each H-ZSM-5, and thus the difference of deactivation rate between [TPA] and [TPA, Na] was not observed.

In contrast, in methylcyclohexane cracking, the deactivation behaviors of [TPA] and [TPA, Na] were clearly different. Figure 5.16 (A, B) shows the changes in the conversion and product distributions of methylcyclohexane cracking over [TPA, Na] and [TPA] along with TOS. The initial conversion was also ca. 100 % and the product distributions at 100 % of the conversion were almost the same. However, [TPA] was drastically deactivated in comparison with [TPA, Na] and the conversion at 10 h on stream of [TPA] was below half of that of [TPA, Na] (ca.15 % and ca. 41 %, respectively). Furthermore, it was clear that the decrease in the micropore volume of [TPA] was larger than that of [TPA, Na], while the coke formation rate of [TPA] was slightly faster than that of [TPA, Na] as shown

Fig. 5.16 (C, D). These findings indicated that the pore plugging by coke formation occurred more seriously on [TPA] than on [TPA, Na].

The degrees of the deactivation and decrease in the micropore volume of [TPA, Na] and [TPA] in methylcyclohexane cracking were higher compared to those in *n*-hexane cracking. These results were in good agreement with Konno and co-workers [53]. However, the amounts of coke deposited during methylcyclohexane cracking were smaller than those during *n*-hexane cracking, suggesting that the location of coke deposition on the H-ZSM-5 zeolite is different from *n*-hexane and methylcyclohexane. In the *n*-hexane cracking, small olefins (C2-C6), small paraffins (C2-C5), methane and hydrogen are known as primary products. In contrast, in methylcyclohexane cracking, in addition to the formation of these molecules via the cracking reaction, aromatics (especially toluene) were also produced as primary products via dehydrogenation in the pores, resulting in the formation of a large amount of benzene, toluene and xylene (BTX) [58]. These aromatic compounds contribute to the formation of heavy hydrocarbons inside the pores and/or on the external surface. Additionally, the diffusion resistances of these aromatic compounds should be larger than other products (i.e. light olefins). Therefore, it is considered that the amount of BTX formed in the pores is related with the amount of coke inside the pores. In the initial stage of reaction, the amount of BTX in the methylcyclohexane cracking was 3 times as much as that in the *n*-hexane cracking (ca. 15 mol% in methylcyclohexane cracking and ca. 5 mol% in *n*-hexane cracking,) as shown Figures 5.15 and 16. A large amount of BTX formation would lead to a large amount of coke formed inside the pores, resulting in the pore plugging.

The coke formation inside the pores in H-ZSM-5 zeolite would occur more easily over acid sites in the intersections than those in the narrow straight or the sinusoidal channels, whilethe limitation of steric constraint in the intersections should be smaller than that in the narrow spaces. The coke formation would proceed through the several reactions via bulky transition sate such as alkylation of aromatics, cyclization and hydrogen transfer reaction [59]. Therefore, the difference in the deactivation rate and the decrease in the micropore volume between [TPA] and [TPA, Na] would be ascribed to the difference in the amount of coke inside the pores. For [TPA], the acid sites located in the intersection would contribute to the formation of coke inside the pores, resulting in rapid deactivation.

The catalyst lifetime is dependent on the acid site distributions in H-ZSM-5 zeolite. The coke formation inside the pores in H-ZSM-5 zeolite would occur over acid sites in the intersections due to large reaction spaces. If H-ZSM-5 zeolite having acid sites located only in narrow straight and/or sinusoidal channels can be synthesized, it is expected that its catalytic lifetime should be longer than that of the conventional one.

5-5 Conclusions

The ZSM-5 with the **MFI**-type aluminosilicate zeolites were successfully synthesized by using tetrapropylammonium cations, dipropylamine, cyclohexylamine or hexamethyleneimine as organic structure-directing agents with or without Na cations. The high-resolution ^{27}Al MAS NMR and ^{27}Al MQMAS NMR techniques revealed that the Al distribution in the framework T sites was clearly dependent on the cation and/or amine used. All of the prepared H-ZSM-5 zeolites exhibited a similar activity for *n*-hexane cracking which proceeded *via* small-sized transition state. However, the activities of these H-ZSM-5 zeolites in 3-methylpenatne cracking were markedly different. From the considerations of the values of the constraint index, in the cracking of 3-methylpentane, the bimolecular cracking proceeds *via* a significantly bulky transition state over the acid sites located at the channel intersections . Accordingly, the acid sites on the H-ZSM-5 synthesized using tetrapropylammonium cations without Na cations are predominantly located in large spaces, namely channel intersections. The acid site distributions estimated based on above consideration affect the catalytic activity for 2,3-dimethylbutane cracking and disproportionation of aromatic compounds which proceed bulky transition state, while activity for *m*-xylene isomerization which proceeds in absence of steric constraint was not affected by acid site distributions. Furthermore, the acid site distributions affect catalytic lifetime for methylcyclohexane cracking. The obtained results indicate that the local distribution of acid sites in the pores has a significant effect on the catalytic performance in transformation of hydrocarbons. These findings will contribute to the design of the zeolite catalyst not only for cracking reaction but also for other several acid-catalyzed reactions.

References

1. R. Gounder, E. Iglesia, Acc. Chem. Res. 2012, 45, 229-238.
2. A. B. Pinar, C. Márquez-Álvarez, M. Grande-Casas, J. Pérez-Pariente, J. Catal. 2009, 263, 258-265.
3. C. Márquez-Álvarez, A. B. Pinar, R. García, M. Grande-Casas, J. Pérez-Pariente, Top. Catal. 2009, 52, 1281-1291.
4. Y. Román-Leshkov, M. Moliner, M. E. Davis, J. Phys. Chem. C 2011,115, 1096-1102.
5. M. Liu, T. Yokoi, M. Yoshioka, H. Imai, J. N. Kondo, T. Tatsumi, Phys. Chem. Chem. Phys., DOI:10.1039/C3CP54297A.
6. W. Vermeiren, J.-P. Gilson, Top. Catal., 2009, 52, 1131-1161
7. International Zeolite Association, Structure Commission, http://www.iza-structure.org/databases/.
8. E.M. Flanigen, J. M. Bennett, R. W. Grose, J. P. Cohen, R. L. Patton, R. M. Kirchner, J. V. Smith, *Nature* **1978**, 271, 512-516.
9. G. D. Price, J. J. Pluth, J. V. Smith, J. M. Bennett, R. L. Patron, *J. Am. Chem. Soc.* **1982**, 104, 5971-5977.
10. K. J. Chao, J. C. Lin, Y. Wang, G. H. Lee, *Zeolites* **1986**, 6, 35-68.
11. Chang, C. D.; Bell, A. T. *Catal. Lett.* **1991**, 8, 305-316.
12. Burkett, S. L.; Davis, M. E. *J. Phys. Chem.* **1994**, 98, 4647-4653.
13. B.M. Lok, T.R. Cannan, C.A. Messina, Zeolites, **1983**, 3, 282-291
14. F.J. Van der Gaag, J.C. Jansen, H. van Bekkum, Appl. Catal., **1985**, 17, 261-271
15. A. Araya, B.M. Lowe, Zeolites, **1986**, 6, 111-118
16. S. Schwarz, M. Kojima, C.T. O'Connor, Appl. Catal., **1991**, 73, 313-330
17. S. Sang, F. Chang, A. liu, C. He, Y. He, L. Xu, Catal. Today, **2004,** 93-95, 729-734
18. V. J. Frilette, W. O. Haag, R. M. Lago, J. Catal. **1981**, 67, 218-222.
19. W. O. Haag, R. M. Lago, P. B. Weisz, *Faraday Discuss. Chem. Soc.* **1981**, 72, 317-330.
20. S. I. Zones, T. Harris, Micropor. Mesopor. Mater. **2000**, 35, 31-46.
21. J. R. Carpenter, S. Yeh, S. I. Zones, M. E. Davis, *J. Catal.* **2010**, 269, 64-70.
22. W. O. Haag, R. M. Dessau, *Proc. 8th Int. Congr. Catalysis. Berlin* **1984**, 2, 305-316.
23. W. O. Haag, R. M. Dessau, R. M. Lago, *Stud. Surf. Sci. Catal.* **1991**, 60, 255-265.
24. H. Krannila, W. O. Haag, B. C. Gates, *J. Catal*. **1992**, 135, 115-124.

25. Q. Wang, Z. M. Cui, C. Y. Cao, W. G. Song, *J. Phys. Chem. C* **2011**, 115, 24987-24992.
26. S.Namba, S Nakanishi, T. Yashima, *J. Catal.* **1984**, 88, 505-508.
27. J. Abbot, Appl. Catal., 57 (1990) 105-125
28. M. Richter, W. Fiebig, H.G. Jerschkewitz, G. Lischke, G. Ohlmann, Zeolites, 9 (1989) 238-246
29. C.S. Cundy, P.A. Cox, Micropor. Mesopor. Mater. 2005, 82, 1-78.
30. E. Lippmaa, A. Samoson, M. Magi, *J. Am. Chem. Soc.* 1986, *108*, 1730-1735.
31. W. Kolodziejski, C. Zicovich-Wilson, C. Corell, J. Perez-Pariente, A. Corma, *J. Phys. Chem.* 1995, *99*, 7002-7008.
32. C. A. Fyfe, Y. Feng, H. Grondey, G. T. Kokotailo, H. Gies, *Chem. Rev.* 1991, 91, 1525-1543.
33. L.B. Alemany, Appl. Magn. Reson. 4 (1993) 179–201.
34. O. H. Han, C.-S. Kim, S.B. Hong, Angew. Chem. Int. Ed., 41 (2002), 469.
35. J. A. Lercher, C. Gründling, G. Eder-Mirth, Catal. Today, 27 (1996) 353-376
36. A. Zecchina, G. Spoto, S. Bordiga, Phys. Chem. Chem. Phys., 7 (2005) 1627-1642
37. K. Kubo, H. Iida, S. Namba, A. Igarashi, Micropor. Mesopor. Mater. 149 (2012) 126-133.
38. S. Namba, A. Inaka and T. Yashima, Zeolites 6 (1986) 107-110.
39. W.W. Kaeding, C. Chu, L.B. Young, B. Weinstein, S.A. Butter, J. Catal., 67 (1981) 159-174
40. L.B. Young, S.A. Butter, W.W. Kaeding, J. Catal., 76 (1982) 418-432
41. S. Cavallaro, L. Pino, P. Tsiakaras, N. Giordano, B.S. Rao, Zeolites, 7 (1987) 408-411
42. T. Hibino, M. Niwa, Y. Murakami, J. Catal., 128 (1991) 551-558
43. J. Čejka, N. Žilková, B. Wichterlová, G. Eder-Mirth, J.A. Lercher, Zeolites, 17 (1996) 265-271
44. Y.S Xiong, P.G Rodewald, C.D Chang, J. Am. Chem. Soc., 117 (1995) 9427-9431
45. A. Corma, A. Cortes, I. Nebot, F. Tomas. J. Catal.. 57 (1979) 444-449.
46. J.A. Martens, J. Pérez-Pariente, E. Sastre, A. Corma, P.A. Jacobs, Appl. Catal., 45 (1988) 85-101
47. Y. Yoshimura, N. Kijima, T. Hayakawa, K. Murata, K. Suzuki, F. Mizukami, K. Matano, T. Konishi, T. Oikawa, M. Saito, T. Shiojima, K. Shiozawa, K. Wakui, G. Sawada, K. Sato, S. Matsuo, N. Yamaoka, Catal. Surv. Jpn. 4 (2000) 157-167.
48. N. Rahimi, R. Karimzadeh, Appl. Catal. A: Gen. 398 (2011) 1–17.
49. S. Inagaki, S. Shinoda, Y. Kaneko, K. Takechi, R. Komatsu, Y. Tsuboi, H. Yamazaki, J. N. Kondo, Y. Kubota, ACS Catal., 3 (2013) 74-78
50. K. Kubo, H. Iida, S. Namba, A. Igarashi, Catal. Commun. 29 (2012) 162-165
51. H. Konno, T. Okamura, Y. Nakasaka, T. Tago, T. Masuda J. Jpn. Pet. Inst., 55 (2012) 267-274

52. H. Konno, T. Okamura, Y. Nakasaka, T. Tago, T. Masuda Chem. Eng. J., 207–208 (2012) 490-496
53. H. Konno, T. Tago, Y. Nakasaka, R. Ohnaka, J. Nishimura, Takao Masuda, Micropor. Mesopor. Mater. 175 (2013) 25-33
54. Y. Nakasaka, T. Okamura, H. Konno, T. Tago, T. Masuda, Micropor. Mesopor. Mater. 182 (2013) 244-249
55. A. Corma, J. Mengual, P. J. Miguel, Appl. Catal. A: Gen. 417 (2012) 220-235.
56. A. Corma, J. Mengual, P. J. Miguel, Appl. Catal. A: Gen. 421-422 (2012) 121-134.
57. A. Corma, J. Mengual, P. J. Miguel, Appl. Catal. A: Gen. 460-461 (2013) 106-115.
58. H.S. Cerqueira, P.C. Mihindou-Koumba, P. Magnoux, M. Guisnet, Ind. Eng. Chem. Res. 40 (2001) 1032-1041.
59. M. Guisnet, P. Magnoux, Appl. Catal., 54 (1989) 1-27

Table 5.1 Chemical analysis and organic content of the ZSM-5 samples.

Sample	**Al content**[a)]	**Na content**[b)]	**C/N**[c)]	**TGA**[d)]	**OSDA content**	**(Na+OSDA)/Al**
	mmol g^{-1}	mmol g^{-1}	molar ratio	wt %	mmol g^{-1}	molar ratio
[TPA]	0.31	n.d.	12.3	14.3	0.70	2.3
[TPA, Na]	0.31	0.28	12.3	13.9	0.68	3.1
[DPa, Na]	0.38	0.28	6.0	7.7	0.76	2.8
[Cha, Na]	0.32	0.09	6.2	5.9	0.59	2.1
[HMi, Na]	0.34	0.11	6.1	10.5	1.06	3.4

[a)] Determined by ICP.

[b)] Determined by AAS.

[c)] Determined by elemental analysis.

[d)] Weight loss in the range 573 to 1073 K as measured by thermogravimetric analysis.

Table 5.2 Physicochemical properties and acid amount of H-ZSM-5 catalysts

Sample	**Si/Al**[a)]	S_{BET}[b)]	S_{EXT}[c)]	V_{micro}[d)]	**Acid amount**[e)]
		$m^2\ g^{-1}$	$m^2\ g^{-1}$	$cm^3\ g^{-1}$	$mmol\ g^{-1}$
[TPA]	53	438	47	0.18	0.29
[TPA, Na]	52	424	43	0.17	0.30
[DPa, Na]	42	412	13	0.17	0.37
[Cha, Na]	51	406	5	0.17	0.31
[HMi, Na]	48	433	41	0.16	0.34

a) Si/Al: atomic ratio of Si/Al in the sample determined by ICP.

b) S_{BET}: BET surface.

c) S_{EXT}: External surface area estimated by t-plot method.

d) V_{micro}: Micropore volume estimated by t-plot method.

e) Acid amount: Estimated by the NH_3-TPD.

Table 5.3 Structure and properties of zeolites used in this study

Sample	**Pore size**	**Pore structure**	**Si/Al**[a)]	S_{BET}[b)]	**Acid amount**[c)]
	Å			m^2 g^{-1}	mmol g^{-1}
H-ZSM-22	4.6 ×5.7	1-D 10MR Straight	52	255	0.28
H-ZSM-5 [TPA,Na]	5.1×5.5 5.3×5.6	3-D 10MR Intersection Sinusoidal	52	424	0.31
H-ZSM-5 [TPA]			53	438	0.29
H-ZSM-12	5.6×6.0	1-D 12MR Straight	48	351	0.27
H-mordenite	6.5×7.6 (2.6×5.7)	1-D 12MR 8MR Side pocket	45	511	0.36

[a)] Si/Al: atomic ratio of Si/Al in the sample determined by ICP.

[b)] S_{BET}: BET surface.

[c)] Acid amount: Estimated by the NH_3-TPD.

Table 5.4 Conversion, total selectivity to methane, ethane and hydrogen and CI values for C6 paraffins cracking over various zeolite

Catalyst	**Conversion** %		**Selectivity to CH_4+C_2H_6+H_2** moles (100 moles cracked)$^{-1}$		**CI**
	n-Hx[a)]	3-MP[b)]	*n*-Hx[a)]	3-MP[b)]	
H-ZSM-22	15	1.6	35	99	9.9
H-ZSM-5 [TPA, Na]	15	3.1	13	69	4.4
H-ZSM-5 [TPA]	16	10.1	13	28	1.7
H-ZSM-12	19	8.4	7.4	37	2.4
H-mordenite	15	14.7	4.8	5.5	1.0

[a)] *n*-hexane cracking

[b)] 3-methylpentane cracking

Reaction conditions

W/F_{total}: 2.0 - 11.2 g h mol_{total}^{-1}, Partial pressure of C6 paraffins: 40 kPa, Reaction temperature: 673 K, Date at 10 min on stream.

n-Hexane cracking and 3-methylpentane cracking were carried out under the same conditions over each zeolite.

Table 5.5 Results of cracking of C6 paraffins over H-ZSM-5 zeolites

Reactant	**Catalysts**	k_{C6} [a]	**Conv.** [b]	**Selectivity to $H_2 + CH_4 + C_2H_6$** [b]	**Ea** [c]
		10^2 mol g^{-1} h^{-1}	%	moles (100 mol cracked C6)$^{-1}$	kJ mol^{-1}
n-Hx[d]	[TPA,Na]	10.5	9.9	13.1	65.7
	[TPA]	11.3	10.2	12.8	66.3
3-MP[e]	[TPA,Na]	1.7	9.5	56.4	81.0
	[TPA]	5.6	11.7	31.3	47.1
2,3-DMB[f]	[TPA,Na]	0.8	2.3	86.5	91.1
	[TPA]	2.2	2.3	55.4	59.1
2,2-DMB[g]	[TPA,Na]	0.5	1.4	96.5	111.6
	[TPA]	0.6	1.6	95.3	107.3

[a] Reaction rate constant at 673 K

[b] Total selectivity to methane, ethane and hydrogen below 10% conversion at 673 K

[c] Activation energy

[d] *n*-Hexane

[e] 3-Methylpentane

[f] 2,3-Dimetylbutane

[g] 2,2-Dimethylbutane

Reaction conditions

W/F_{total}: 1.0 - 6.2 g h mol_{total}^{-1}, Partial pressure of C6 paraffins: 40 kPa, Reaction temperature: 623 - 673 K, Date at 10 min on stream, 2,4-Dimethylquinoine : 1.1 μLmin^{-1}

Table 5.6 Reaction rate constants for *n*-hexane and methylcyclohexane cracking over [TPA] and [TPA, Na] at 923 K.

Catalyst	$k_{n\text{-}hexane}$ [a]	$k_{methylcyclohexane}$ [b]
	/ mol g^{-1} h^{-1}	
[TPA,Na]	2.0	2.2
[TPA]	1.9	2.2

[a] *n*-hexane cracking rate constant

[b] methylcyclohexane cracking rate constant

Reaction conditions

W/F_{total}: 0.1 – 0.3 g h mol_{total}^{-1}, Partial pressure of hydrocarbon: 40 kPa, Reaction temperature: 923 K, Date at 10 min on stream.

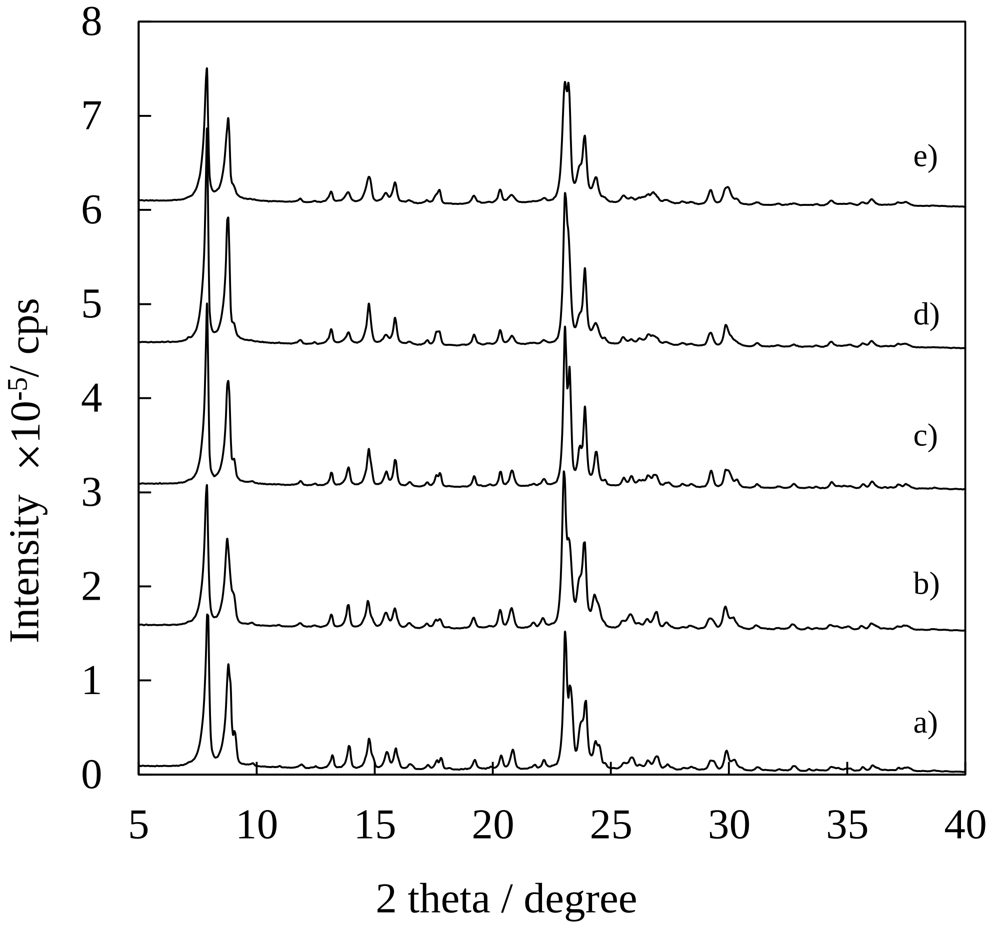

Figure 5.1

XRD patterns of NH_4-ZSM-5 zeolites: a) [TPA], b) [TPA, Na], c) [DPa, Na], d) [Cha, Na] and e) [HMi, Na].

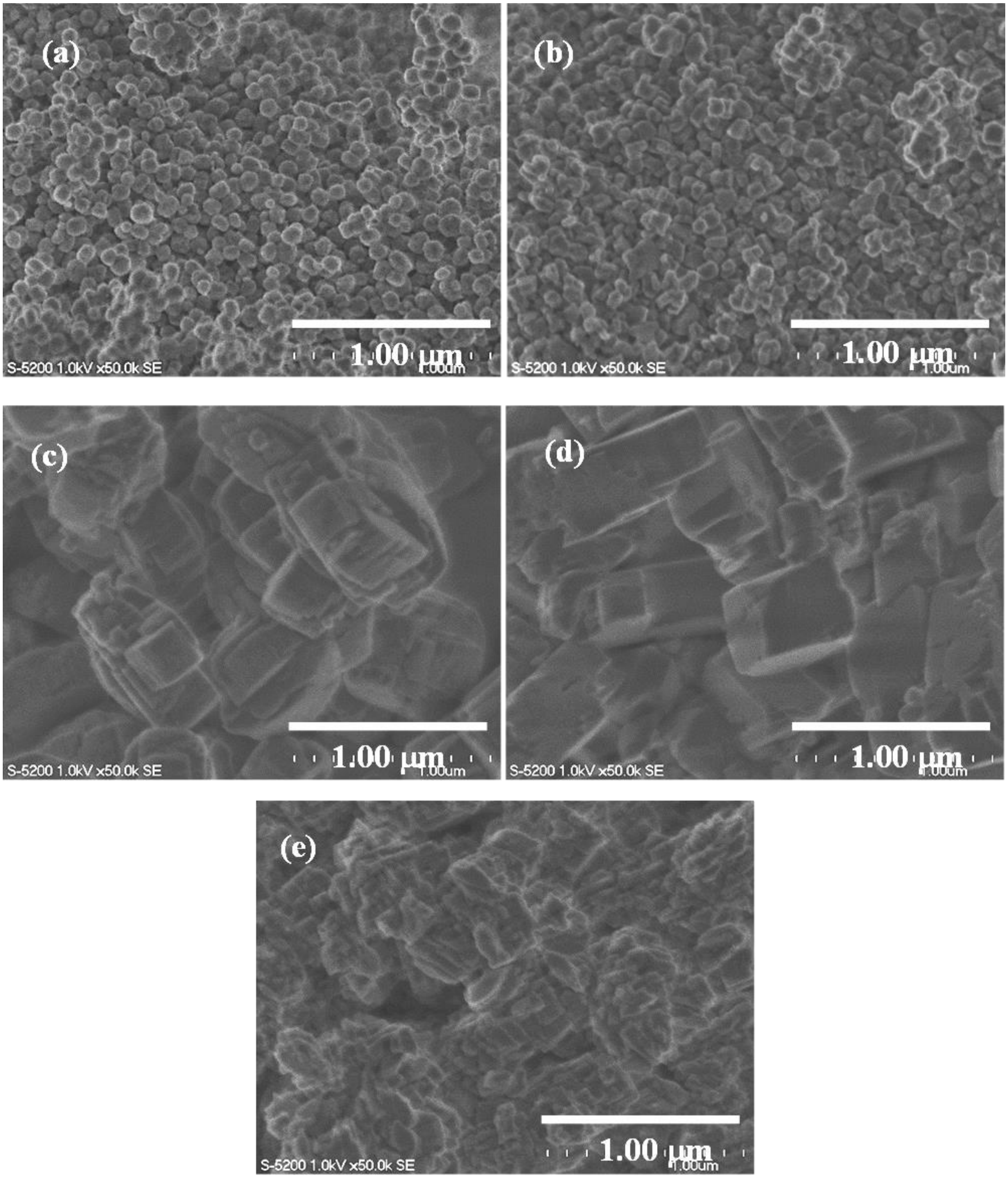

Figure 5.2

FE-SEM and TEM images of NH_4-ZSM-5 catalysts; a) [TPA], b) [TPA, Na], c) [DPa, Na], d) [Cha, Na] and e) [HMi, Na].

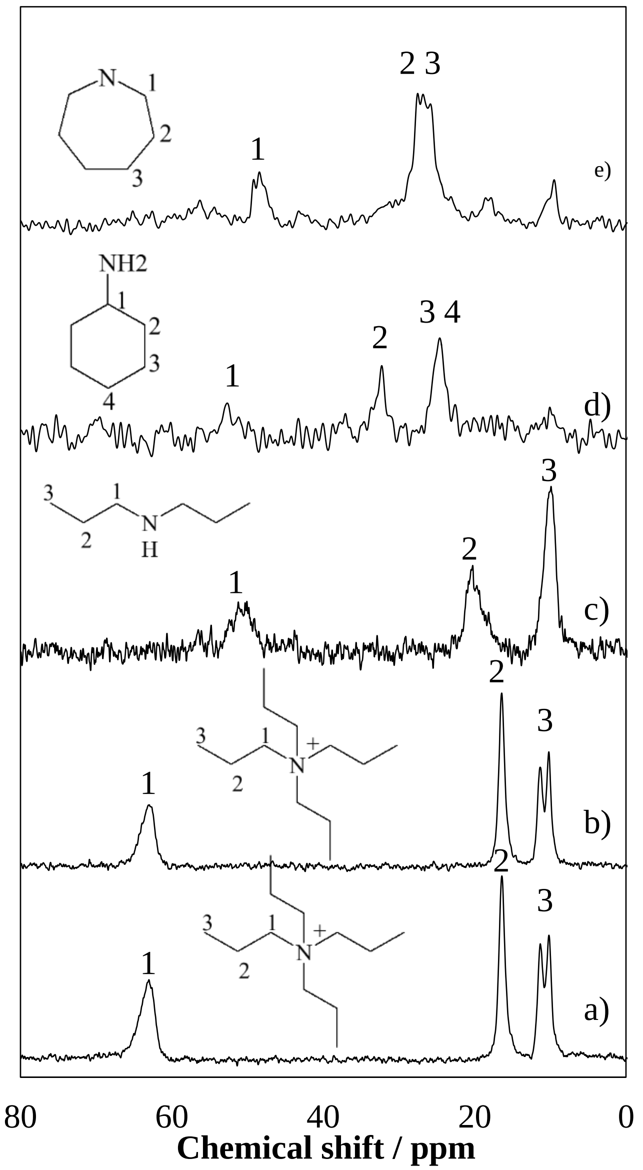

Figure 5.3

^{13}C CP MAS NMR of as-made ZSM-5 samples: a) [TPA], b) [TPA, Na], c) [DPa, Na], d) [Cha, Na] and e) [HMi, Na].

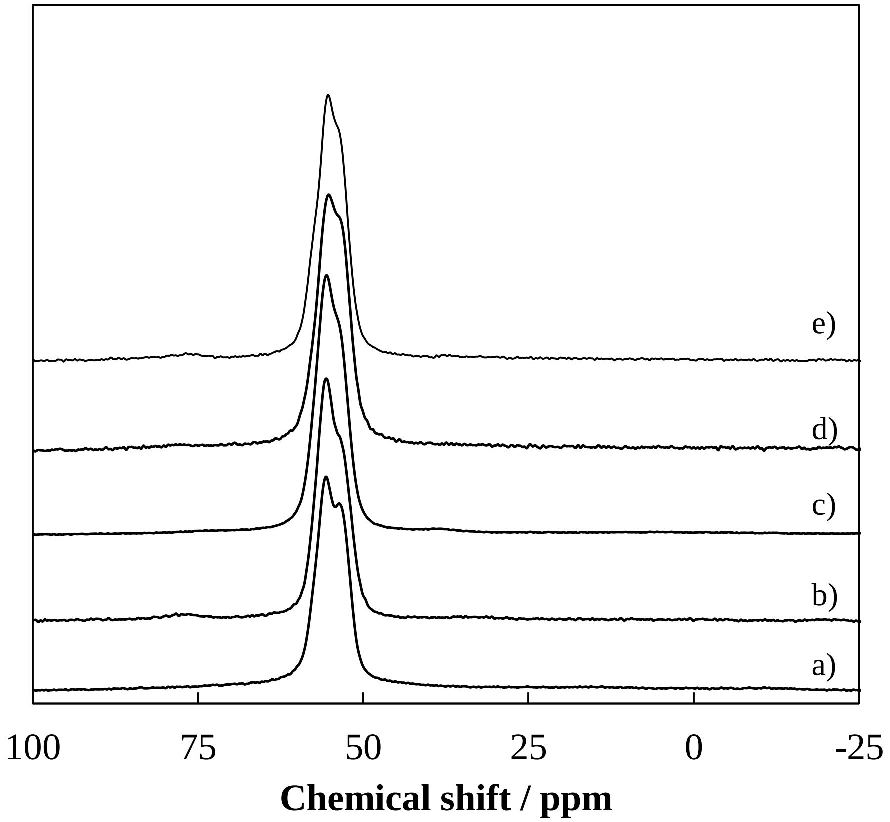

Figure 5.4

^{27}Al MAS NMR spectra of NH_4-ZSM-5 zeolites: a) [TPA], b) [TPA, Na], c) [DPa, Na], d) [Cha, Na] and e) [HMi, Na].

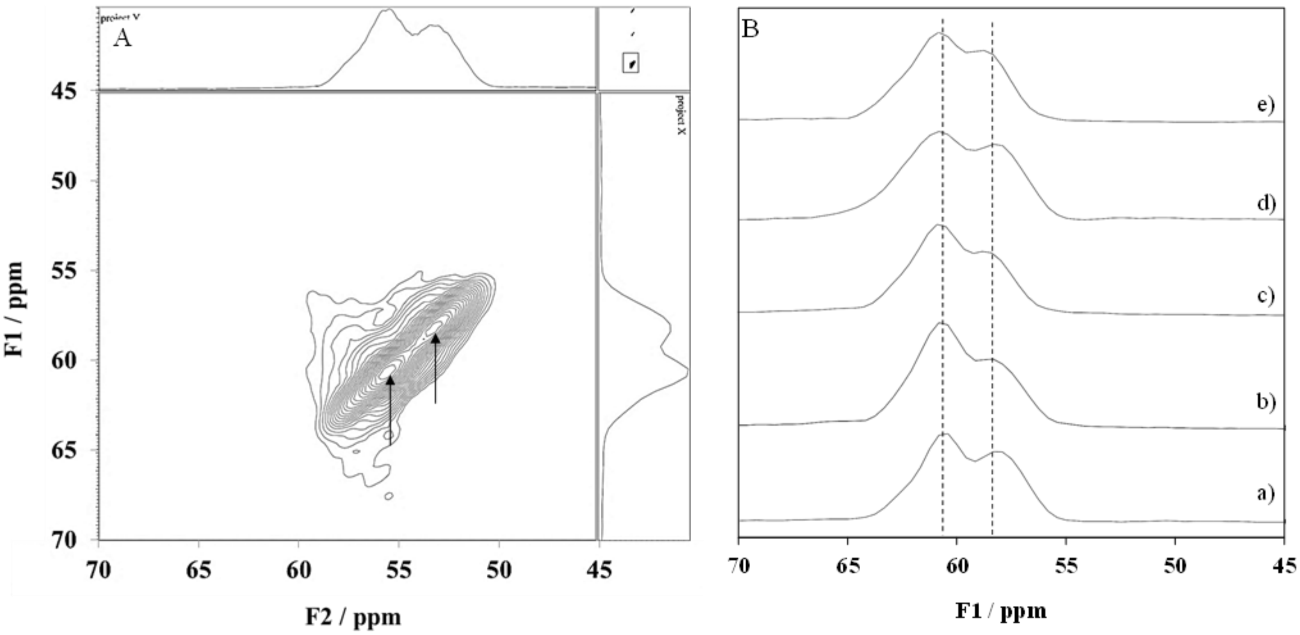

Figure 5.5

(A) Aluminum in different T sites in the ^{27} Al MQMAS of [TPA]. (B) ^{27}Al MQMAS F1 projection of NH_4-ZSM-5: a) [TPA], b) [TPA, Na], c) [DPa, Na], d) [Cha, Na] and e) [HMi, Na].

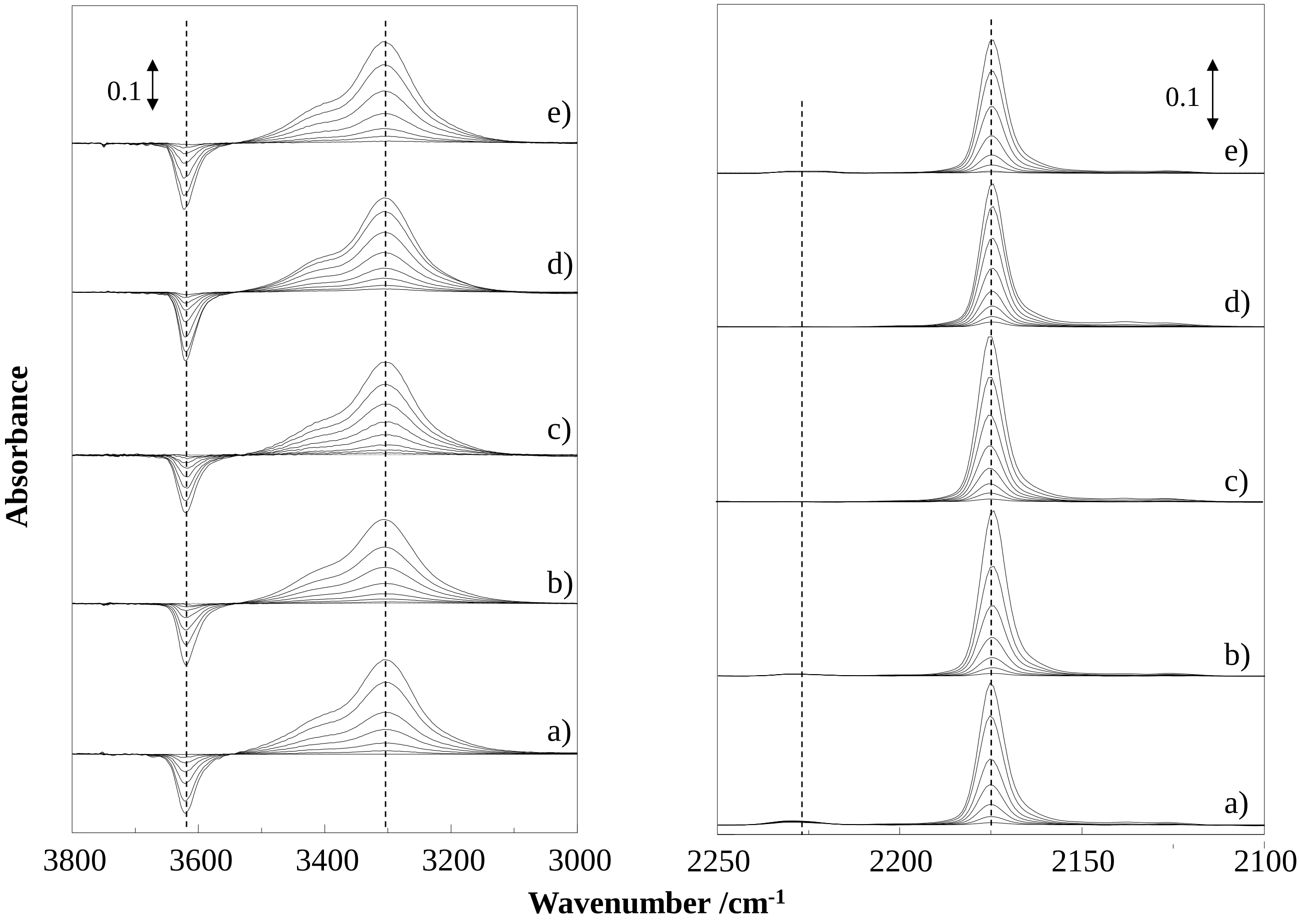

Figure 5.6

Differential FT-IR spectra for CO-adsorbed H-ZSM-5 zeolites a) [TPA], b) [TPA, Na], c) [DPa, Na], d) [Cha, Na] and e) [HMi, Na].

(A) ν(OH) region; (B) ν(CO) region

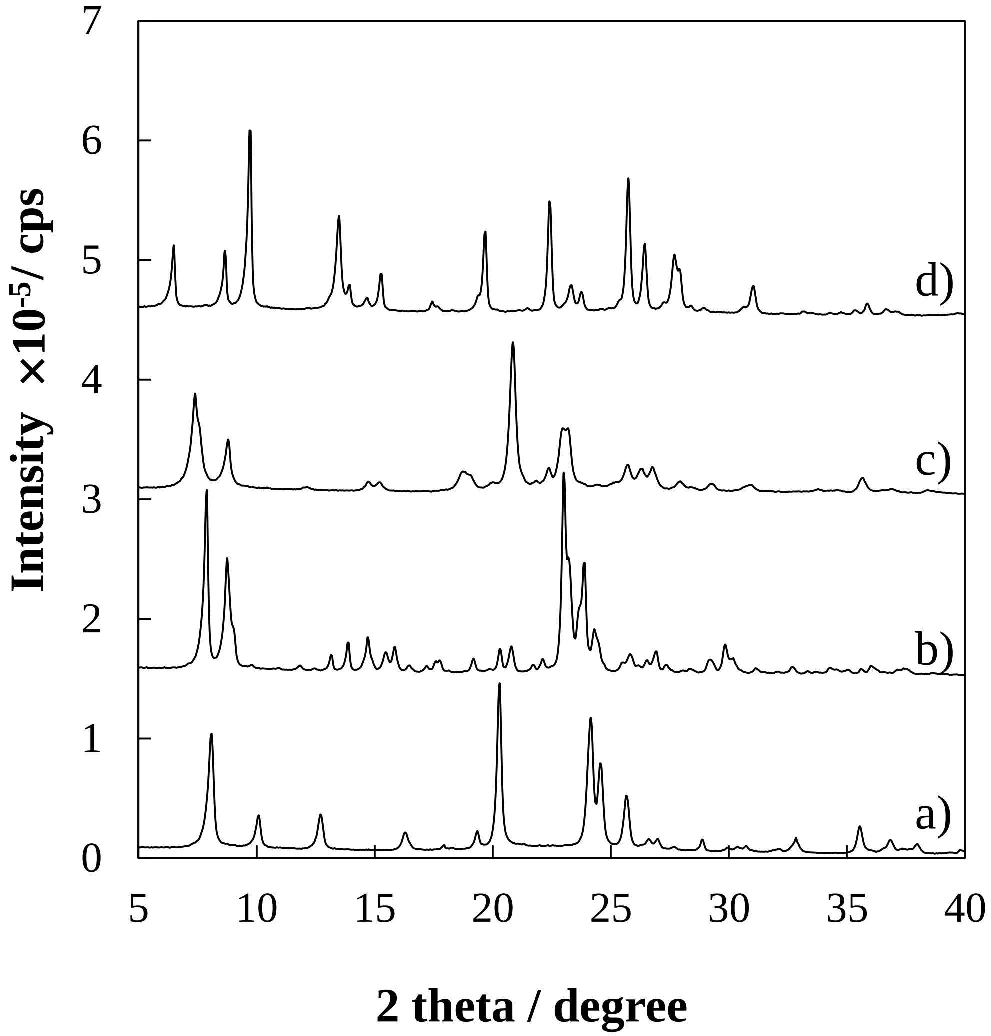

Figure 5.7

XRD patterns of various zeolites: a) ZSM-22, b) ZSM-5 [TPA, Na], c) ZSM-12, d) mordenite.

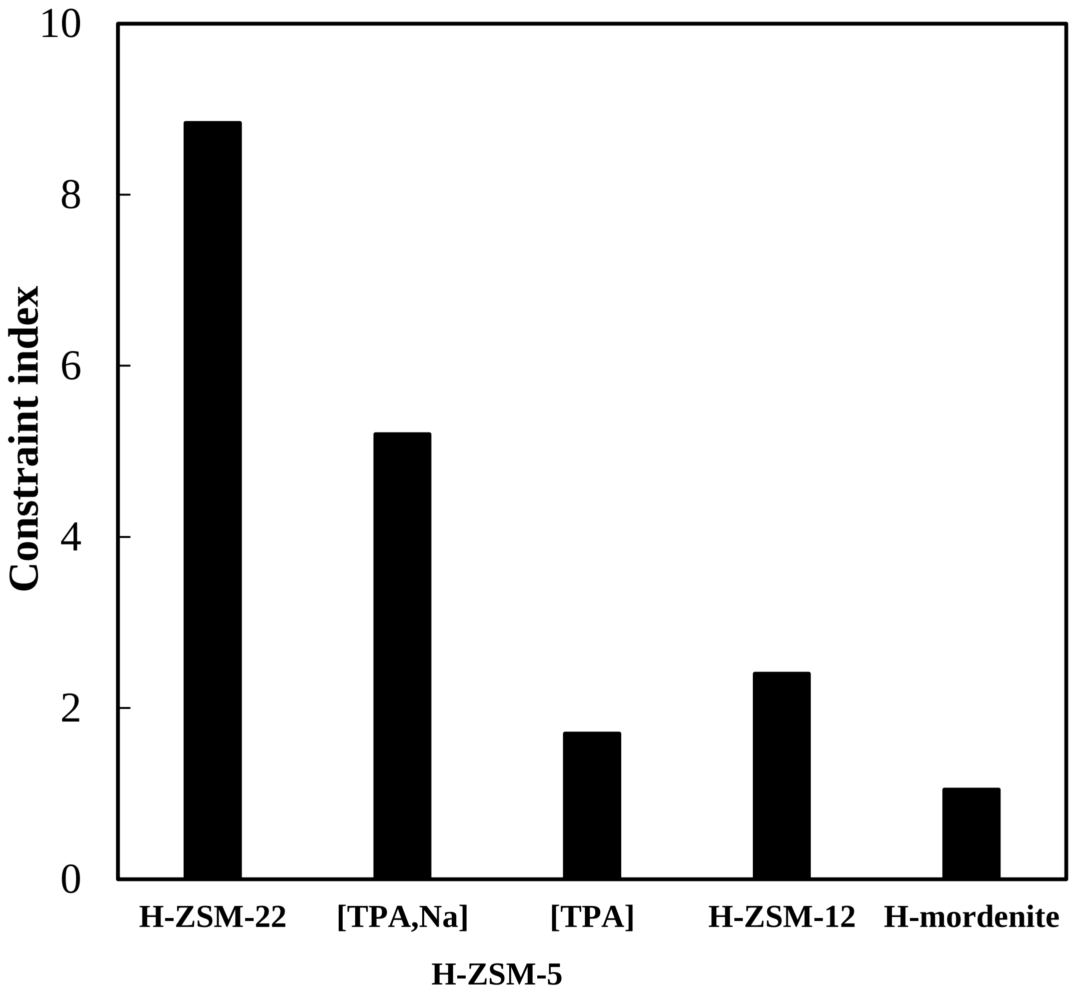

Figure 5.8

Constraint index values for various zeolites at 673 K.

Reaction conditions

W/F$_{total}$: 2.0 - 11.2 g h mol$_{total}^{-1}$, Partial pressure of C6 paraffins: 40 kPa, Reaction temperature: 673 K, Date at 10 min on stream.

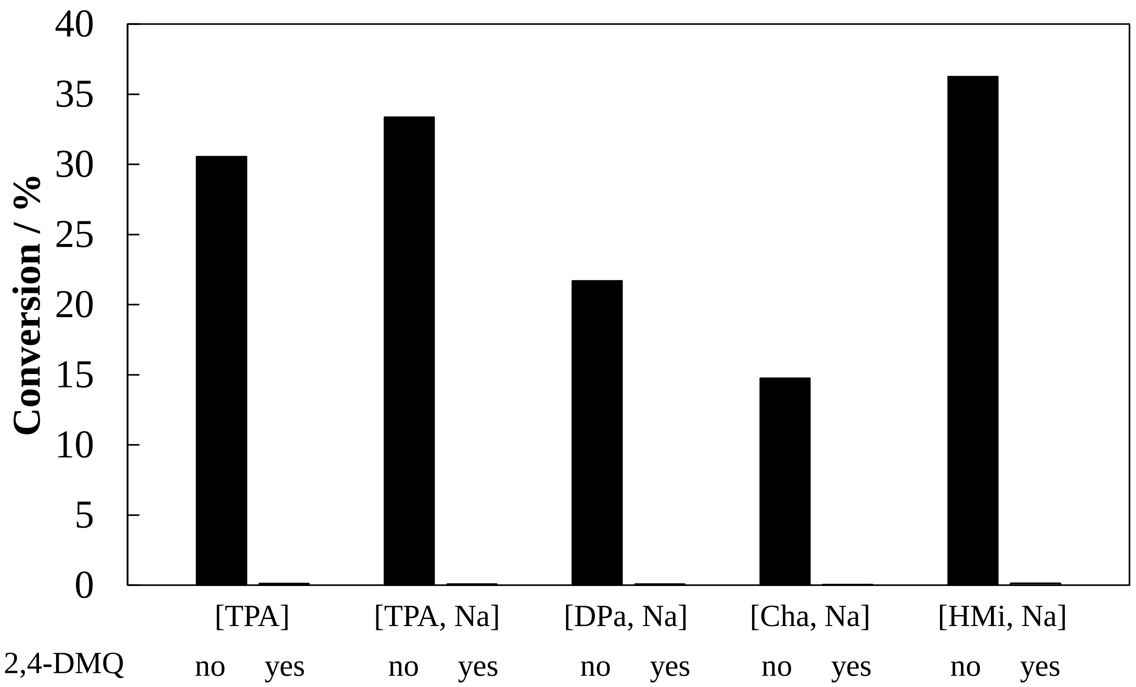

Figure 5.9

1,3,5-TIPB cracking over H-ZSM-5 zeolites with or without 2,4-DMQ.

Reaction conditions

W/F_{total}: 0.2 g h mol_{total}^{-1}, Partial pressure of 1,3,5-TIPB: 0.5 kPa, Reaction temperature: 673 K, 2,4-DMQ: 10 wt % added in 1,3,5-TIPB (ca. 0.22 μl min^{-1}), Date at 10 min on stream.

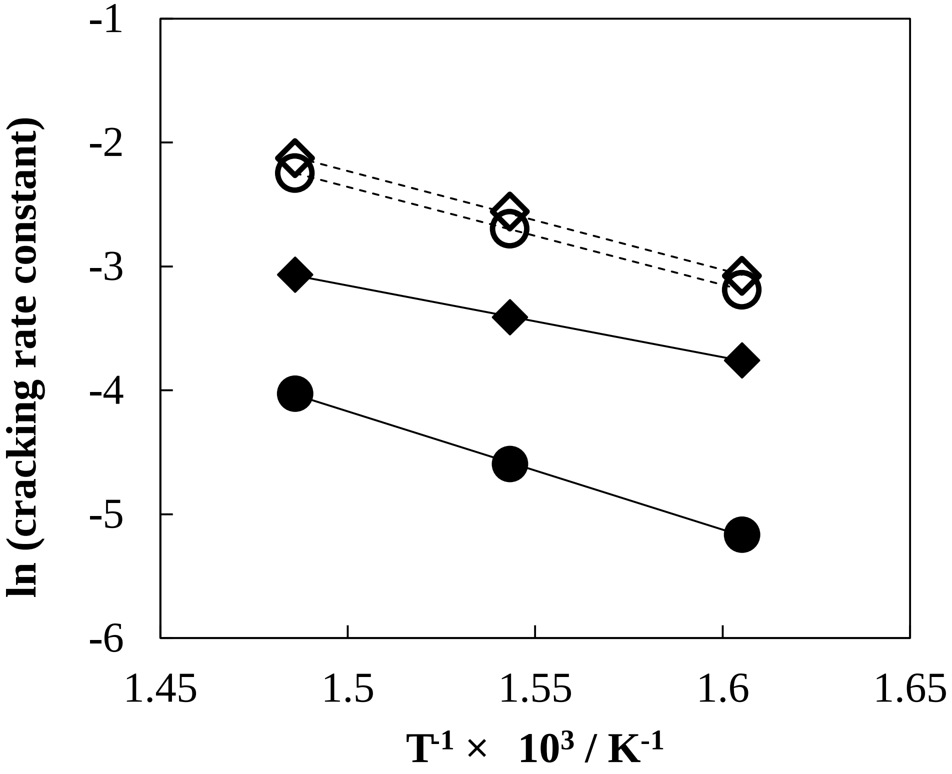

Figure 5.10

Arrhenius plots for *n*-hexane (open symbol) and 3-methyl-pentane (solid symbol) cracking: [TPA, Na] (●), [TPA] (◆).

Reaction conditions

W/F$_{total}$: 1.0 - 2.7 g h mol$_{total}$$^{-1}$, Partial pressure of C6 paraffins: 40 kPa, Reaction temperature: 623 - 673 K, Date at 10 min on stream, 2,4-Dimethylquinoine : 1.1 μLmin^{-1}

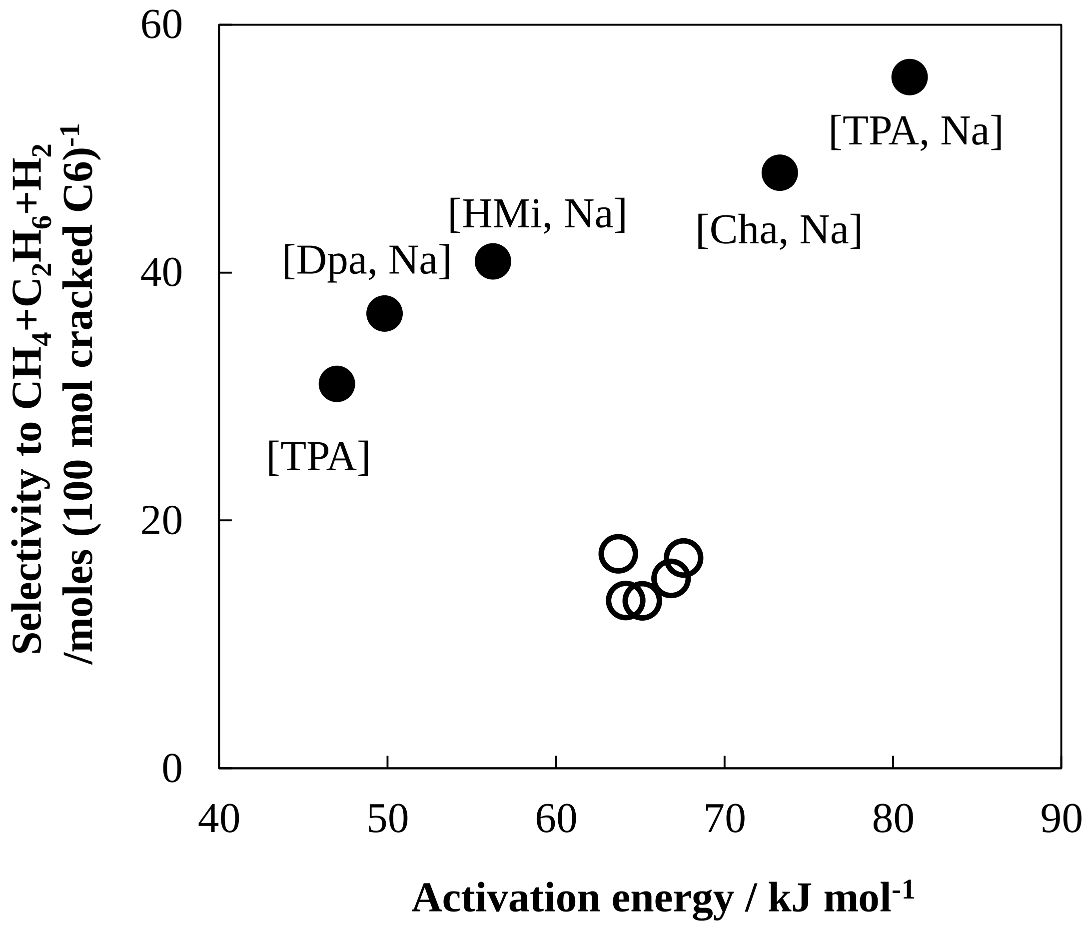

Figure 5.11

Relationship between activation energy and total selectivity to H_2 + CH_4 + C_2H_6 at 10 % conversion* for *n*-hexane (open symbol) and 3-methylpenatne (solid symbol) cracking over H-ZSM-5 zeolites.

* Reaction temp: 673 K

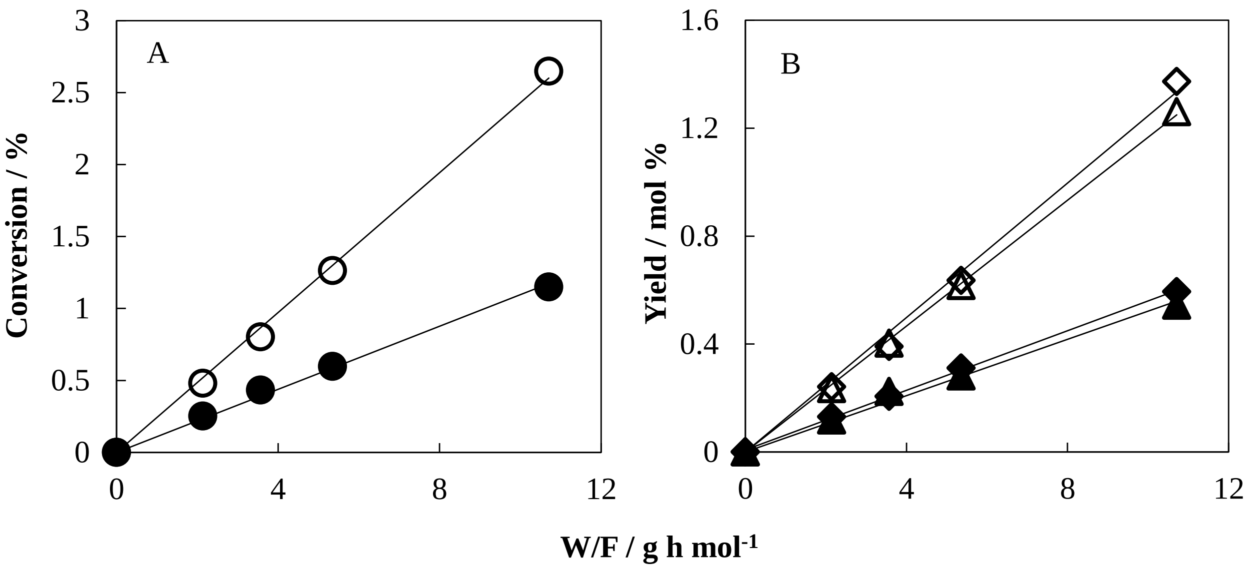

Figure 5.12

Dependence of W/F on (A) toluene conversion (B) formation of benzene (◆) and xylene (▲) over [TPA] (open symbol) and [TPA, Na] (solid symbol).

Reaction conditions

W/F$_{total}$: 2.1 - 10.7 g h mol$_{total}^{-1}$, Partial pressure of toluene paraffins: 20 kPa, Reaction temperature: 623 K, Date at 10 min on stream, 2,4-Dimethylquinoine : 1.1 μLmin^{-1}

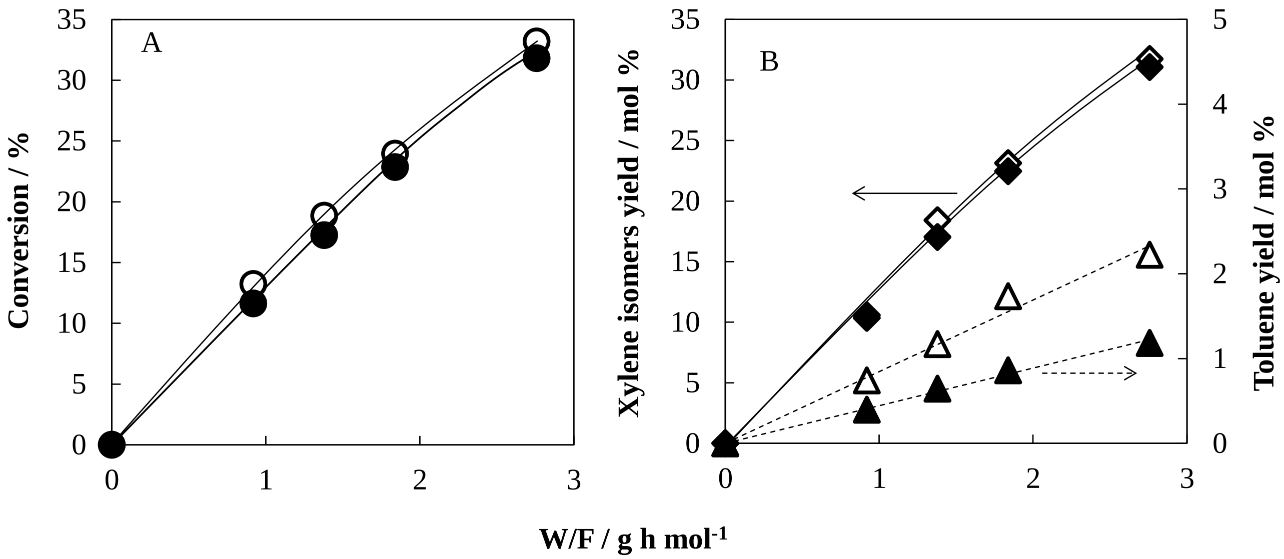

Figure 5.13

Dependence of W/F on (A) *m*-xylene conversion (B) formation of xylene isomer (◆) and toluene (▲) over [TPA] (open symbol) and [TPA, Na] (solid symbol).

Reaction conditions

W/F_{total}: 1.0 – 2.7 g h mol_{total}^{-1}, Partial pressure of *m*-xylene: 20 kPa, Reaction temperature: 623 K, Date at 10 min on stream, 2,4-Dimethylquinoline: 1.1 μ$Lmin^{-1}$

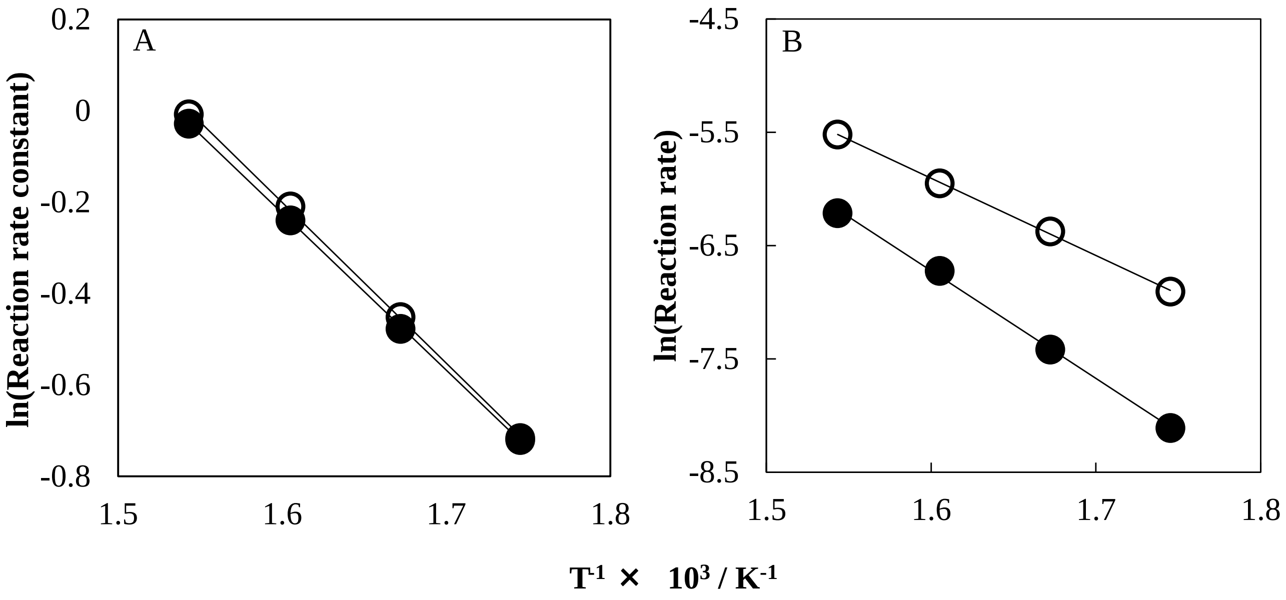

Figure 5.14

Arrhenius plots for (A) *m*-xylene conversion (B) toluene conversion over [TPA] (open symbol) and [TPA, Na] (solid symbol).

Reaction conditions

W/F$_{total}$: 0.1 - 10.7 g h mol$_{total}$$^{-1}$, Partial pressure of aromatic compounds: 20 kPa, Reaction temperature: 573 - 648 K, Date at 10 min on stream, 2,4-Dimethylquinoine : 1.1 μLmin^{-1}

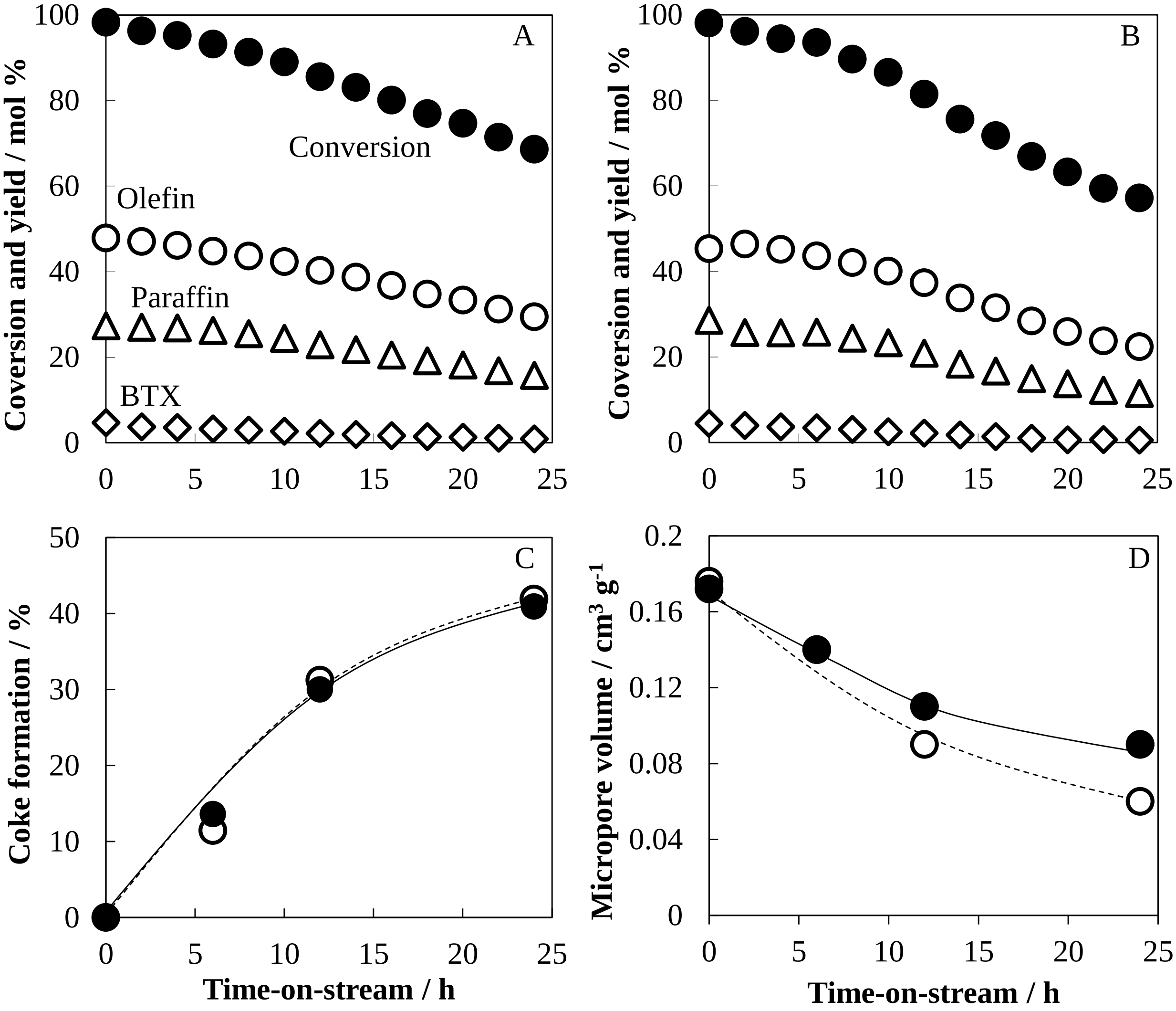

Figure 5.15

Results of *n*-hexane cracking at 923 K

(A, B) Change in the conversion and product yields[a)] against time on stream of (A) [TPA, Na] and (B) [TPA]. (C) Relationship between reaction time and coke amount[b)]. (D) Relationship between reaction time and micropore volume[b)].

[a)] Olefin: Total yield of ethylene, propylene and butenes. Paraffin: Total yield of ethane, propane and butanes. BTX: Total yield of benzene, toluene and xylenes

[b)] [TPA] (open symbol), [TPA, Na] (solid symbol)

Reaction conditions

W/F_{total}: 2.7 g h mol_{total}^{-1}, Partial pressure of *n*-hexane: 40 kPa, Reaction temperature: 923 K

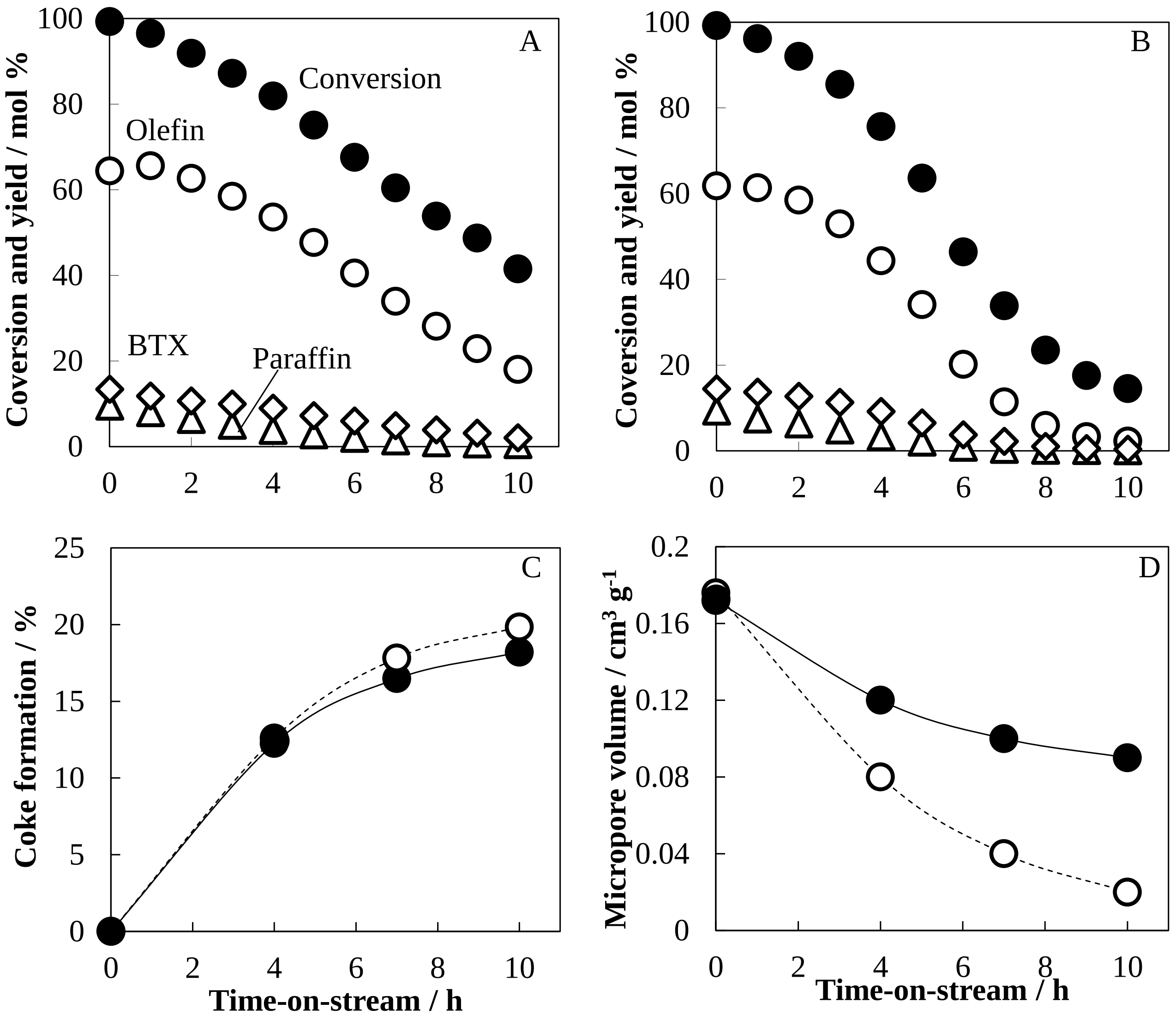

Figure 5.16

Results of methylcyclohexane cracking at 923 K

(A, B) Change in the conversion and product yields$^{a)}$ against time on stream of (A) [TPA, Na] and (B) [TPA]. (C) Relationship between reaction time and coke amount$^{b)}$. (D) Relationship between reaction time and micropore volume$^{b)}$.

$^{a)}$ Olefin: Total yield of ethylene, propylene and butenes. Paraffin: Total yield of ethane, propane and butanes. BTX: Total yield of benzene, toluene and xylenes

$^{b)}$ [TPA] (open symbol), [TPA, Na] (solid symbol)

Reaction conditions

W/F_{total}: 2.7 g h mol_{total}^{-1}, Partial pressure of methylcyclohexane: 40 kPa, Reaction temperature: 923 K

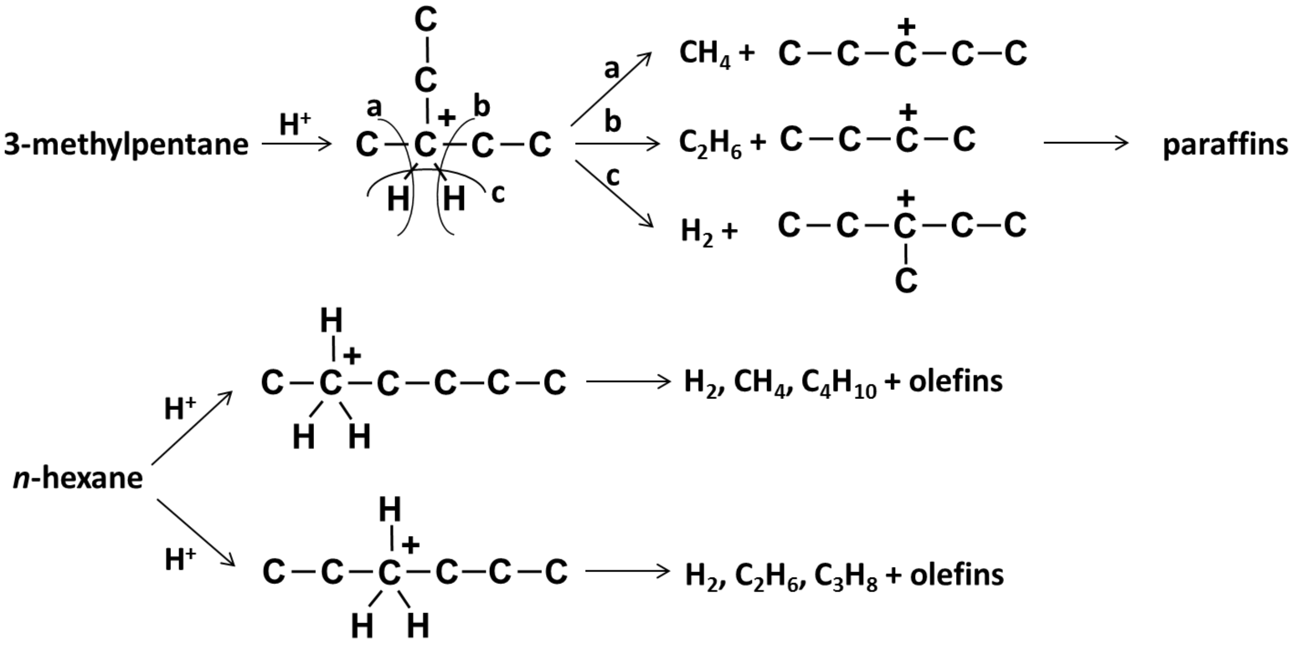

Scheme 5.1
Monomolecular cracking of C6 paraffins [22]

Chapter 6

Summary

Chapter 2

The ZSM-5 zeolites with different crystallite sizes (65 nm - 1.0 μm) were successfully synthesized by tuning of synthesis conditions. Crystallite sizes of ZSM-5 were strongly affected by the amount of water in the starting gel and pre-aging conditions before crystallization. Both the optimized pre-aging process and the small amount of water in the synthesis gel are indispensable for preparing the ZSM-5 nanocrystals. In *n*-hexane cracking over H-ZSM-5 zeolites with different crystallite sizes (100 nm, 400 nm and 1.0 μm), the crystallite size little affected the initial activity and selectivity of H-ZSM-5 zeolite catalysts. Therefore, the cracking of *n*-hexane over H-ZSM-5, whose crystallite size is less than 1.0 μm, is not limited by diffusion of *n*-hexane. The small-sized H-ZSM-5 catalyst exhibited the slowest deactivation rate among these H-ZSM-5 catalysts. The coke formation rate decreased with a decrease in crystallite size because of short diffusion path length. Additionally, when a similar amount of coke was deposited on each catalyst, the smaller-sized catalyst suffered from the less deactivation than the larger-sized catalyst, because of large number of pore entrances. From these findings, the reduction in the crystallite size of ZSM-5 is highly effective in improving the catalytic lifetime in the *n*-hexane cracking, because of large external surface areas and short diffusion path lengths.

Chapter 3

The catalytic performance of alkali- and alkali-acid treated H-ZSM-5 in the *n*-hexane cracking was studied. External surface areas and the amount of Lewis acid sites were increased with an increase in the NaOH concentration. The deactivation rate was decreased with an increase in external surface area. The deactivation rate on the large-sized H-ZSM-5 catalyst treated with 0.2 M NaOH aq. solution is less than half of that on the parent H-ZSM-5 catalyst. The larger number of pore entrances and shorter diffusion path lengths should retard the deactivation due to blocking by coke formed during the reaction. The small-sized H-ZSM-5 catalysts are more stable against coke deposition than the large-sized catalysts, because of their shorter average diffusion path lengths. The external surface hardly affects the selectivity in *n*-hexane cracking. However, Lewis acid sites enhance dehydrogenation and aromatization at high temperatures (≥873 K), resulting in the formation of large amount of aromatic compounds and coke. The Lewis acid sites on the alkali treated H-ZSM-5 can be removed by the acid treatment. The conversion for the alkali-acid treated H-ZSM-5 is slightly low compared with the parent alkali-treated H-ZSM-5. However, it exhibits the higher selectivity to propylene and a less amount of coke formed during *n*-hexane cracking. Therefore, the alkali-acid treatment of H-ZSM-5 is an effective and simple post-treatment method, leading to a high propylene yield and a long lifetime.

Chapter 4

The high-resolution ^{27}Al MAS NMR and ^{27}Al MQMAS NMR techniques revealed that the Al distributions in the framework T sites were different among H-ZSM-5 zeolites with various Al contents used in the present study. The proportion of Al atoms occupying the T-sites with smaller T-O-T angles is increased with an increase in the Al content. However, the Brønsted acid strengths of these H-ZSM-5 zeolites are quite similar to each other. In *n*-hexane cracking over H-ZSM-5 zeolite, total selectivity to hydrogen, methane and ethane can be applicable as a parameter to estimation of contribution of monomolecular cracking of paraffin regardless of reaction temperature. Additionally, the changes in the activation energy for monomolecular cracking can be estimated from the activation energy for the formation of these molecules. The cracking mechanism ratio depends on the Al content at low temperatures (≤ 723 K), as a result the activation energy is decreased with an increase in the Al content. On the other hand, at high reaction temperatures (≥ 823 K), the monomolecular cracking is dominant and the Al content scarcely affect the reaction mechanism ratio [(monomolecular cracking rate)/(bimolecular cracking rate)]. However, the activation energy for the monomolecular cracking of *n*-hexane is decreased along with the Al content in despite of similar Brønsted acid strength. It is considered that transition state in monomolecular *n*-hexane cracking may be more stabilized on active sites with the smaller T-O-T angles.

Chapter 5

The **MFI**-type aluminosilicate zeolites (ZSM-5) were successfully synthesized by using tetrapropylammonium cations, dipropylamine, cyclohexylamine or hexamethyleneimine as organic structure-directing agents with or without Na cations. The high-resolution ^{27}Al MAS NMR and ^{27}Al MQMAS NMR techniques revealed that the Al distribution in the framework T sites was clearly dependent on kinds of cation or amine used. All the prepared H-ZSM-5 zeolites exhibited a similar activity for *n*-hexane cracking which proceeded via small sized transition states. However, the activities these H-ZSM-5 zeolites for 3-methylpenatne cracking were essentially different. From the results of constraint index test for various zeolite, it is considered that the bimolecular cracking proceeds via a significantly bulky transition state over acid sites located at the channel intersections in the cracking of 3-methylpentane over H-ZSM-5 zeolites. Accordingly, the acid sites on H-ZSM-5 synthesized using tetrapropylammonium cations without Na cations are most selectively located in large spaces, namely channel intersections. The acid site distributions estimated based on above consideration affect the catalytic activity for 2,3-dimethylbutane cracking which proceed bulky transition state. Furthermore, the acid site distributions affect catalytic lifetime in methylcyclohexane cracking. The coke formation inside the pores in H-ZSM-5 zeolite would occur more readily over acid sites located at the intersections due to large reaction spaces. If H-ZSM-5 zeolite having acid sites located only in narrow straight and/or sinusoidal channels can be synthesized, it is expected that its catalytic lifetime should be longer than that of the conventional one.

List of Publications

1. Hiroshi Mochizuki, Toshiyuki Yokoi, Hiroyuki Imai, Ryota Watanabe, Seitaro Namba, Junko N. Kondo, Takashi Tatsumi “Facile control of crystallite size of ZSM-5 catalyst for cracking of hexane” Microporous and Mesoporous Materials, 145 (2011) 165 (Chapter 2)
2. Hiroshi Mochizuki, Toshiyuki Yokoi, Hiroyuki Imai, Seitaro Namba, Junko N. Kondo, Takashi Tatsumi “Effect of desilication of H-ZSM-5 by alkali treatment on catalytic performance in hexane cracking” Applied Catalysis A: General, 449 (2012) 188 (Chapter 3)
3. Hiroshi Mochizuki, Toshiyuki Yokoi, Seitaro Namba, Junko N. Kondo, Takashi Tatsumi “Interpretation of catalytic performance of H-ZSM-5 with different aluminum contents for hexane cracking based on reaction mechanism” in preparation. (Chapter 4)
4. Hiroshi Mochizuki, Toshiyuki Yokoi, Seitaro Namba, Junko N. Kondo, Takashi Tatsumi “A new calss of ZSM-5 catalyst: Design, synthesis and catalytic performance of ZSM-5 zeolite with the distribution of acid site in the pores controlled” in preparation. (Chapter 5)

List of Conference presentations

1. Poster presentation at international conference

1. ○Hiroshi Mochizuki, Hiroyuki Imai, Toshiyuki Yokoi, Junko N. Kondo, Seitaro Namba, Takashi Tatsumi “The effect of crystal sizes of H-ZSM-5 on catalytic cracking of *n*-hexane”, YP20-128, TOCAT6/APCAT5, Sapporo Convention Center, Hokkaido,Japan, 7/18-23, 2010.
2. ○Hiroshi Mochizuki, Hiroyuki Imai, Toshiyuki Yokoi, Junko N. Kondo, Seitaro Namba, Takashi Tatsumi“Influence of particle size of zeolite on catalytic properties for *n*-hexane cracking”, YP20-128, Pacifichem 2010, Hawaii Convention Center; Hilton Hawaiian Village; Sheraton Waikiki; and the Royal Hawaiian Hotel, Honolulu, Hawaii, USA, 12/15-20, 2010.
3. ○Hiroshi Mochizuki, Hiroyuki Imai, Toshiyuki Yokoi, Junko N. Kondo, Seitaro Namba, Takashi Tatsumi“The influence of alkali treatment of H-ZSM-5 on catalytic cracking of *n*-hexane”, PP-102, The 13th Korea - Japan Symposium on Catalysis, Seogwipo KAL Hotel, Jeju Island, Korea, 5/23-25, 2011.
4. ○Hiroshi Mochizuki, Hiroyuki Imai, Toshiyuki Yokoi, Seitaro Namba, Junko N. Kondo, Takashi Tatsumi“Effect of alkali treatment on lifetime of H-ZSM-5 zeolite for hexane cracking” , CRC International Symposium on Green & Sustainable Catalysis: from Theoretical and Fundamental Aspects to Catalyst Design, Catalysis Research Center (CRC), Hokkaido University, Japan, 1/26-27, 2012.
5. ○Hiroshi Mochizuki, Hiroyuki Imai, Toshiyuki Yokoi, Seitaro Namba, Junko N. Kondo, Takashi Tatsumi “Effect of aluminum content of H-ZSM-5 on hexane cracking activity”, P-178, International Symposium on Zeolites and Micro Porous Crystals, Aster Plaza, Hiroshima, Japan, 7/28-8/1, 2012.
6. ○Hiroshi Mochizuki, Toshiyuki Yokoi, Seitaro Namba, Junko N. Kondo, Takashi Tatsumi “Hexane Cracking Over H-ZSM-5 with Different Al Contents” , 287160, 2012 AIChE (American institute of Chemical Engineers) Anuual Meeting, The David L. Lawrence Convention Center, Pittsburgh, PA, USA, 10/28-11/2, 2012.
7. ○Hiroshi Mochizuki, Toshiyuki Yokoi, Seitaro Namba, Junko N. Kondo, Takashi Tatsumi “Estimation of acid site distribution in pores of H-ZSM-5 zeolite”, PB-007, 7th International Symposium on Acid-Base Catalysis, TKP Garden City Shinagawa, Tokyo, Japan, 5/12-5/15, 2013.
8. ○Hiroshi Mochizuki, Toshiyuki Yokoi, Seitaro Namba, Junko N. Kondo, Takashi Tatsumi “Control

of acid site distribution in the pores of H-ZSM-5 zeolite", YP07, The 14th Japan-Korea Symposium on Catalysis, Winc Aichi, Nagoya, Japan 7/1-3, 2013.

9. ○Hiroshi Mochizuki, Toshiyuki Yokoi, Seitaro Namba, Junko N. Kondo, Takashi Tatsumi "Estimation of acid site distribution in pores of H-ZSM-5 zeolite prepared with various structure-directing agents" , P-1.1-12, 17th International Zeolite Conference, Congress Center of the Izmailovo complex, Moscow, Russia, 7/7-12, 2013.
10. ○Hiroshi Mochizuki, Toshiyuki Yokoi, Seitaro Namba, Junko N. Kondo, Takashi Tatsumi "Effects of Acid Sites Location in H-ZSM-5 Zeolite on Cracking of Alkanes" , Mon-P1-201, The 6 Asia-Pacific Congress on Catalysis, Taipei International Convention Center, Taipei, Taiwan, 10/13-17, 2013.

2. Oral presentation at international conference

11. ○Hiroshi Mochizuki, Hiroyuki Imai, Toshiyuki Yokoi, Junko N. Kondo, Seitaro Namba, Takashi Tatsumi, "Catalytic Cracking of Hexane over H-ZSM-5 Zeolite", 24aHeO02, Joint Conference of The Fifth International Conference on the Science and Technology for Advanced Ceramics (STAC5) and The 2nd International Conference on Advanced Materials Development and Integration of Novel Structured Metallic and Inorganic Materials (AMDI2), Mielparque-Yokohama, Yokohama, Japan, 6/22-24, 2011.
12. ○Hiroshi Mochizuki, Hiroyuki Imai, Toshiyuki Yokoi, Seitaro Namba, Junko N. Kondo, Takashi Tatsumi "Improvement of catalytic lifetime of H-ZSM-5 in hexane cracking by alkali treatment", 2.02_7519, 15th International Congress on Catalysis, International Congress Center Munich, Munich, Germany, 7/1-6, 2012. (Poster symposia)

3. Poster presentation at domestic conference

13. ○望月大司，今井裕之，横井俊之，難波征太郎，辰巳敬，"ナノサイズ ZSM-5 によるヘキサンの接触分解"，C-7，第 10 回 GSC シンポジウム，学術総合センター・一橋記念講堂，東京，3/4-5, 2010.
14. ○望月大司，難波征太郎，今井裕之，横井俊之，野村淳子，辰巳 敬，"修飾 ZSM-5 触媒によるヘキサンの接触分解"，P38，石油学会第 59 回研究発表会　第 15 回 JPIJS 若手研究者のためのポスターセッション，タワーホール船堀，東京, 5/20, 2010.

15. ○望月大司，今井裕之，横井俊之，難波征太郎，野村淳子，辰巳 敬，“ゼオライトの酸性質がヘキサン接触分解に及ぼす影響検討”, 2P74, 第 107 回触媒討論会, 首都大学東京, 東京, 3/29-30, 2011.
16. ○望月大司，難波征太郎，今井裕之，横井俊之，野村淳子，辰巳 敬，“ゼオライトを用いたヘキサン接触分解におけるルイス酸点の影響”，P17，石油学会第 60 回研究発表会　第 16 回 JPIJS 若手研究者のためのポスターセッション，タワーホール船堀, 東京, 5/18, 2011.（国内，ポスター）
17. ○望月 大司，今井 裕之， 横井 俊之， 難波 征太郎，野村 淳子，辰巳 敬，“ZSM-5 の酸性質制御とヘキサン接触分解性能評価”，A-29，第 11 回 GSC シンポジウム，早稲田大学・国際会議場，東京，6/2-3, 2011.
18. ○望月大司，横井俊之，今井裕之，難波征太郎，野村淳子，辰巳敬，“種々の SDA を用いて合成した H-ZSM-5 のパラフィンクラッキング特性”，P33，石油学会第 61 回研究発表会　第 17 回 JPIJS 若手研究者のためのポスターセッション，タワーホール船堀, 東京, 5/25, 2012.
19. ○望月 大司，横井 俊之，難波 征太郎，野村 淳子，辰巳 敬，“H-ZSM-5 の酸点位置の制御”，A-21，第 12 回 GSC シンポジウム，ベルサール神田，東京，6/12-13, 2012.
20. ○望月 大司， 横井 俊之， 難波 征太郎, 野村 淳子, 辰巳 敬, “酸点分布の異なる H-ZSM-5 の調製と触媒特性”， 1P07， 第 111 回触媒討論会, 関西大学, 大阪, 3/25-26, 2013. （優秀ポスター発表賞）
21. ○望月 大司， 横井 俊之， 難波 征太郎，野村 淳子，辰巳 敬，“H-ZSM-5 の酸点位置分布がメタノール転換反応に及ぼす影響”， 第 2 回 JACI/GSC シンポジウム，メルパルク大阪，大阪，6/6-7, 2013.

4. Oral presentation at domestic conference

22. ○望月大司，渡邉亮太，今井裕之，横井俊之，難波征太郎，辰巳敬，“ナノサイズ ZSM-5 の合成と酸触媒特性評価”，A27, 第 25 回ゼオライト研究発表会，西日本総合展示場新館展示場, 福岡, 11/25-26, 2009.
23. ○望月大司，今井裕之，横井俊之，難波征太郎，辰巳敬，“ゼオライト固体酸触媒によるヘ

キサンの接触分解”, 2D1-36, 日本化学会第90回春季年会, 近畿大学, 大阪, 3/26-29, 2010.

24. ○望月大司，今井裕之，横井俊之，難波征太郎，野村淳子，辰巳 敬， “ゼオライト触媒によるヘキサンの接触分解”，4E07，第106回触媒討論会，ベルクラシック甲府．山梨大学甲府キャンパス，山梨, 9/15-18, 2010.
25. ○望月大司，今井裕之，横井俊之，難波征太郎，野村淳子，辰巳 敬，“修飾ゼオライトによるヘキサンの接触分解”，1B22，第40回石油・石油化学討論会，神戸国際会議場，兵庫, 11/25-26, 2010.
26. ○望月大司，今井裕之，横井俊之，難波征太郎，野村淳子，辰巳 敬, “Al含有量がH-ZSM-5のパラフィン接触分解活性に及ぼす影響”，2H01，第109回触媒討論会，北見工業大学, 北海道, 9/20-22, 2011.
27. ○望月大司，横井俊之，今井裕之，難波征太郎，野村淳子，辰巳敬，“ZSM-5のSi/Al比が酸性質およびヘキサン接触分解特性に及ぼす影響”, C26, 第27回ゼオライト研究発表会, 関西大学千里山キャンパス，大阪, 12/1-2, 2011.
28. ○望月大司，横井俊之，今井裕之，難波征太郎，野村淳子，辰巳敬，“外表面積の異なるH-ZSM-5触媒を用いたヘキサンの接触分解”，2A08，第109回触媒討論会，東京工業大学大岡山キャンパス，東京, 3/28-29, 2012.
29. ○望月大司，今井裕之，横井俊之，難波征太郎，野村淳子，辰巳 敬, “Al含有量がH-ZSM-5のパラフィン接触分解活性に及ぼす影響”，2H01，第109回触媒討論会，北見工業大学, 北海道, 9/20-22, 2011.
30. ○望月 大司， 横井 俊之， 難波 征太郎，野村 淳子，辰巳 敬，“H-ZSM-5を用いた炭化水素分解反応に及ぼす酸点位置の影響”，B12，第28回ゼオライト研究発表会，タワーホール船堀，東京，11/29-30, 2012.
31. ○望月 大司， 横井 俊之， 難波 征太郎, 野村 淳子, 辰巳 敬, “酸点分布の異なるH-ZSM-5を用いた芳香族炭化水素転換反応”， 3C093， 第112回触媒討論会，秋田大学，秋田，9/18-20, 2013.
32. ○望月 大司， 横井 俊之， 難波 征太郎，野村 淳子，辰巳 敬，“ZSM-5ゼオライト細孔内の酸点分布制御と触媒機能評価”，C20総，第29回ゼオライト研究発表会，東北大学, 宮城，11/27-28, 2013.

Acknowledgements

The present thesis is collection of the studies which have been carried out at Chemical Resources Laboratory, Tokyo Institute of Technology during 2009-2014. I would like to express my gratitude to all people that supported me to complete this thesis.

First of all, I would like to express my deepest gratitude to Prof. Dr. Takashi Tatsumi for accepting me as a student in his laboratory and giving me the opportunity to do this research. I am really grateful for his constructive guidance, valuable suggestion, insightful comments and considerable encouragement.

I would like to express my special gratitude to Dr. Seitaro Nambe for his patient guidance, invaluable discussion and considerable encouragement. I would like to express my sincere gratitude to Assoc. prof. Dr. Junko N. Kondo and Assist. Prof. Dr. Toshiyuki Yokoi for their insightful and valuable advice, detailed comments, concrete suggestions and hearty encouragement. I would also like to express my gratitude to Assoc. Prof. Dr. Hiroyuki Imai (The University of Kitakyushu) for his constructive suggestions and advice.

I would like to express my deep gratitude to Prof. Dr. Takao Masuda, Assoc. prof. Dr. Teruoki Tago, Assist. Prof. Dr. Yuta Nakasaka (Hokkaido University), Prof. Dr. Yoshihiro Kubota, Assoc. prof. Dr. Satoshi Inagaki (Yokohama National University), Prof. Dr. Takayuki Komatsu, Assist. Prof. Dr. Shinya Furukawa (Tokyo Institute of Technology) and members of REACT, in particular Dr. Atsuyuki Miyaji, Mr. Masayoshi Murakami and Mr. Satoshi Akiyama, for their kind advice and the fruitful discussion in the Development of Fundamental Technology for Innovative Naphtha Cracking Process Using Catalyst (Green sustainable chemistry project of New Energy and Industrial Technology Development Organization (NEDO)).

I am grateful to Assoc. prof. Dr. Yusuke Yoshinaga at Tokyo Gakugei University. I took a keen interest in the chemistry of catalyst thanks to his guidance at his laboratory when I was an undergraduate student.

I would like to express my thanks to all members of Tatsumi Nomura laboratory. In particular, Mr. Ryoichi Otomo, Mr. Hiroshi Yamazaki and Mr. Ming Liu who are my contemporaries at laboratory for their cooperation and help.

This work was supported by the green sustainable chemistry project of NEDO. This work was also partly supported by Grant-in-Aid for Scientific Research (S) (No. 19106015) of Education, Culture, Sports, Science and Technology of Japan (MEXT) and Research and Development in a New Interdisciplinary Field Based on Nanotechnology and Materials Science Program of the Ministry of MEXT.

Finally, I would like to express my best thanks to my family for their support, understanding and encouragement.

March, 2014
Hiroshi Mochizuki